

AD-A122 404

A STUDY OF MICROSTRIP ANTENNAS FOR MULTIPLE BAND  
OPERATION(U) ILLINOIS UNIV AT URBANA DEPT OF ELECTRICAL  
ENGINEERING Y T LO ET AL. SEP 82 UIU-EM-82-3

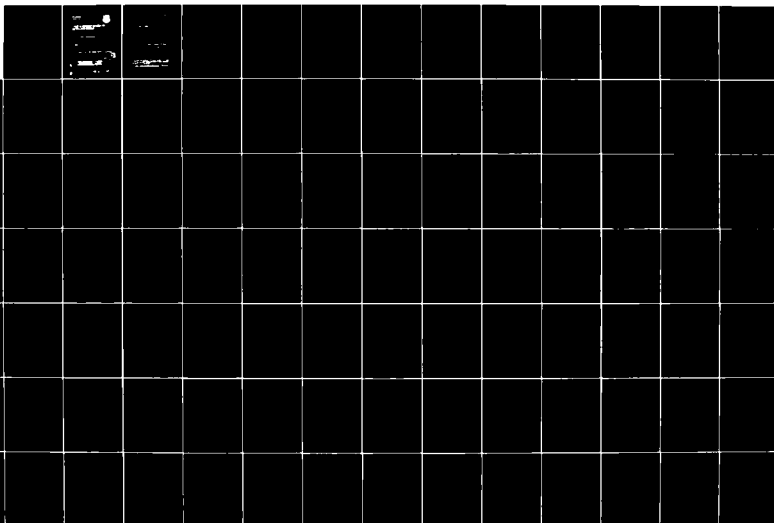
1/2

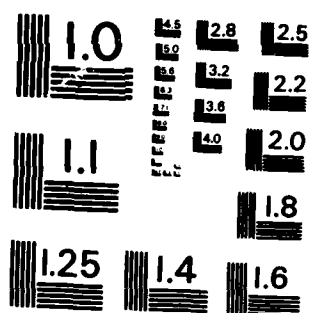
UNCLASSIFIED

RADC-TR-82-236 APOSR-81-0234

F/O 9/5

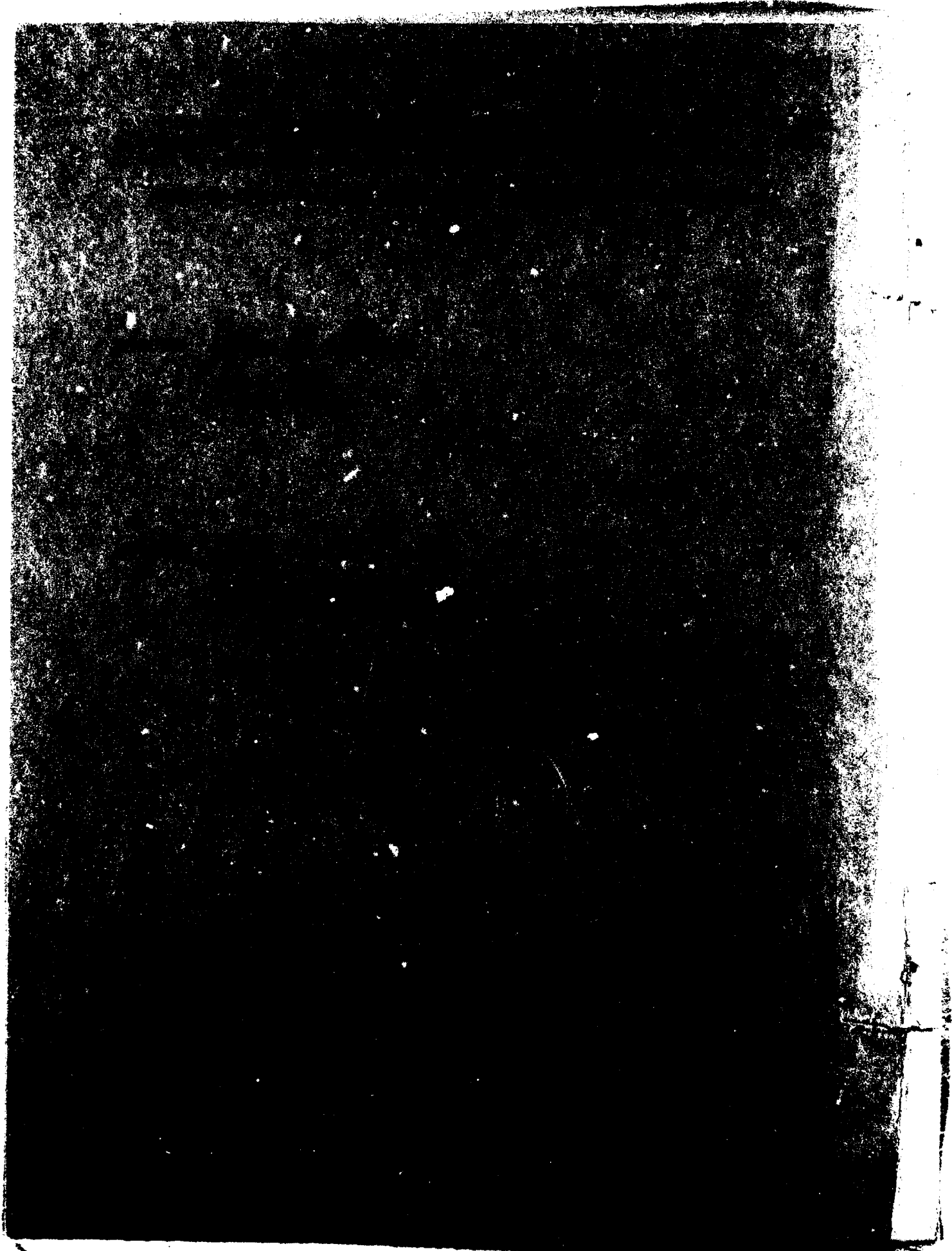
NL





MICROCOPY RESOLUTION TEST CHART  
NATIONAL BUREAU OF STANDARDS-1963-A

AD A 122 404



UNCLASSIFIED

SECURITY CLASSIFICATION OF THIS PAGE (When Data Entered)

REPORT DOCUMENTATION PAGE		READ INSTRUCTIONS BEFORE COMPLETING FORM
1. REPORT NUMBER RADC-TR-82-236	2. GOVT ACCESSION NO. AD-A122 404	3. RECIPIENT'S CATALOG NUMBER
4. TITLE (and Subtitle) A STUDY OF MICROSTRIP ANTENNAS FOR MULTIPLE BAND OPERATION		5. TYPE OF REPORT & PERIOD COVERED Final Technical Report 1 June 81 - 31 May 82
7. AUTHOR(s) Y.I. Lo C.E. Skupien S.S. Zhong		6. PERFORMING ORG. REPORT NUMBER EM 82-3, UILU-82-2541
9. PERFORMING ORGANIZATION NAME AND ADDRESS University of Illinois at Urbana-Champaign Dept of Electrical Engineering/Electromagnetics Urbana IL 61801		8. CONTRACT OR GRANT NUMBER(s) AFOSR 81-0234
11. CONTROLLING OFFICE NAME AND ADDRESS Rome Air Development Center (EEAA) Hanscom AFB MA 01731		10. PROGRAM ELEMENT, PROJECT, TASK AREA & WORK UNIT NUMBERS 61102F 2305J331
14. MONITORING AGENCY NAME & ADDRESS (if different from Controlling Office) Same		12. REPORT DATE September 1982
		13. NUMBER OF PAGES 134
		15. SECURITY CLASS. (of this report) UNCLASSIFIED
		16a. DECLASSIFICATION/DOWNGRADING SCHEDULE N/A
18. DISTRIBUTION STATEMENT (of this Report)  Approved for public release; distribution unlimited		
17. DISTRIBUTION STATEMENT (of the abstract entered in Block 20, if different from Report)  Same		
19. SUPPLEMENTARY NOTES RADC Project Engineer: John A. Strom (EEAA)		
19. KEY WORDS (Continue on reverse side if necessary and identify by block number) Microstrip Antennas Dual-Frequency Microstrip Antennas Annular Microstrip Antennas Modified Rectangular Microstrip Antennas Frequency Tuning Theory and Experiment of Shorting Pins		
20. ABSTRACT (Continue on reverse side if necessary and identify by block number) Thin microstrip antennas have remarkably compact structure; but they are inherently narrow-banded. To extend their usefulness, the possibility of multiple-frequency operation is often speculated. Some workers have considered a design for dual frequency operation by using actually two patch antennas of different dimensions and interconnected with transmission lines, while others made use of an elaborate microstrip line circuit in an ad hoc fashion for achieving a certain dual-frequency operation. (Over)		

FORM 1473

EDITION OF 1 NOV 65 IS OBSOLETE

UNCLASSIFIED

SECURITY CLASSIFICATION OF THIS PAGE (When Data Entered)

UNCLASSIFIED

SECURITY CLASSIFICATION OF THIS PAGE (When Data Entered)

In both cases the unique and attractive feature of compactness of microstrip antennas is compromised.

In this investigation two approaches have been studied, both theoretically and experimentally, in an attempt to achieve that goal. The first investigation is made on annular microstrip antennas. As seen from the cavity model theory, an antenna of this type, if excited for (1,1), (1,2) and (1,3) modes, will all have predominantly broadside radiation of the same polarization. However, unlike disc or rectangular patches, the resonant frequencies for these modes are not fixed ratios, being dependent on the dimensions of the inner and outer radii. Sets of curves and tables which show this dependence are presented. In addition, the feeding methods and techniques for suppressing undesirable modes are discussed. For most microstrip antennas, such as disc and rectangle, the computer resonant frequency from the cavity model theory is always higher than the measured, due to the fringing field effect. However, for annulus, this may not be true since it has two unconnected boundaries. This is also investigated in some detail.

In the second approach, a rectangular patch, excited particularly in the (0,1) and (0,3) modes, is investigated since they both produce broadside radiations of the same polarization. However, the operating frequencies for these modes are at a fixed ratio, approximately 3:1. To remove this restriction, electrically shorting pins are inserted along the modal lines in the (0,3) modal over a wide range while that of the (0,1) mode is kept unchanged. The frequency variation with the number of pins is tabulated. For the pins investigated so far, the ratio of the two frequencies can be changed from 1.8 to 3. The effect of shorting pins can be predicted with good accuracy by the multiport theory.

In some cases, the patch dimensions which are proper for the low-frequency band may become too large for the high band so that large grating lobes appear in the pattern. This problem can be solved by either using materials of moderately high dielectric constant, or using a modified version of the rectangular patch in which one edge is electrically shorted to the ground. The former is straightforward and needs no new theory. Some effort is therefore expended to evaluate the field, pattern, impedance, and frequency tuning range with the pins of the new antenna. It is shown that dual frequency operation is indeed feasible with this type of element.

Obviously, it is highly desirable to have a new design such that a single patch with only one simple feed can be made to operate for two or more discrete bands. This kind of element would find many important applications. For example, for large arrays, they would not only make possible a significant saving in material but also in space and weight, which of course are a major problem in space-borne systems.

UNCLASSIFIED

SECURITY CLASSIFICATION OF THIS PAGE (When Data Entered)

## TABLE OF CONTENTS

	Page
PREFACE .....	v
PART I. ANNULAR MICROSTRIP ANTENNAS AND THEIR APPLICATIONS TO DUAL-FREQUENCY OPERATION .....	1
CHAPTER 1. INTRODUCTION .....	1
CHAPTER 2. ANALYSIS OF THE ANNULAR RING MICROSTRIP ANTENNA..	4
2-1 THE CAVITY MODEL .....	4
2-2 THE INTERNAL FIELD STRUCTURE .....	6
2-2-1 THE RESONANT MODE EXPANSION METHOD...	8
2-2-2 EXPANSION USING MODAL-MATCHING TECHNIQUE .....	19
2-3 RADIATED POWER .....	23
2-4 STORED ENERGY .....	27
2-5 DIELECTRIC LOSS .....	28
2-6 COPPER LOSS .....	29
2-7 THE DISTRIBUTED SYSTEM .....	30
2-8 THE INPUT IMPEDANCE .....	32
CHAPTER 3. ANALYTIC AND EXPERIMENTAL RESULTS .....	33
3-1 THE LOSS TANGENT AND SKIN DEPTH .....	33
3-2 THE QUALITY FACTOR .....	33
3-3 THE RESONANCE FREQUENCY .....	34
3-4 THE INPUT IMPEDANCE AND RADIATION PATTERN...	37
3-5 THE DUAL FREQUENCY ANTENNA .....	43
CHAPTER 4. FRINGING FIELDS AND THE EDGE CORRECTION .....	64
CHAPTER 5. CONCLUSION .....	74



at  
A

Library Codes  
Avail and/or  
Special

	Page
APPENDIX A: CALCULATION OF THE ELECTRIC STORED ENERGY.....	76
APPENDIX B: RESONANT FREQUENCY AND THE EDGE EFFECT .....	78
LIST OF REFERENCES .....	80
 PART II. DUAL-FREQUENCY RECTANGULAR MICROSTRIP ANTENNAS .....	 82
CHAPTER 1. INTRODUCTION .....	82
CHAPTER 2. THEORY OF A MODIFIED RECTANGULAR MICROSTRIP ANTENNA .....	85
2-1 GENERAL ANALYSIS FOR THE FIELD IN THE PATCH .....	85
2-2 INPUT IMPEDANCE .....	88
2-3 FAR FIELD .....	88
2-4 Q-FACTOR .....	90
2-5 MULTI-PORT THEORY AND APPLICATIONS TO ANTENNAS WITH SHORTING PINS .....	91
CHAPTER 3. THEORETICAL AND EXPERIMENTAL RESULTS .....	93
3-1 INTRODUCTION .....	93
3-2 MICROSTRIP ANTENNA WITH ONE SHORTING PIN..	95
3-3 EFFECT OF MULTIPLE PINS ON RESONANT FREQUENCIES .....	102
3-4 REGULAR RECTANGULAR MICROSTRIP ANTENNA FOR DUAL-FREQUENCY OPERATION .....	110
CHAPTER 4. CONCLUSION .....	120
LIST OF REFERENCES .....	122



## PREFACE

This report consists of two independent parts, both of which are devoted to the theory and design of dual frequency microstrip antennas.

In recent years thin microstrip antennas have attracted much attention mainly because of their compactness in structure and simplicity in fabrication. However, their applications are restricted to systems of rather narrow bandwidth unless thick substrate can be tolerated. To extend their usefulness one may ask the next question, whether or not they can be designed to operate for two or more separate frequency bands. This work is intended to provide some answers.

One obvious solution to the dual-frequency microstrip antenna is simply to construct two patch antennas on the same substrate, separated at some distance, and interconnected with some microstrip lines. In this approach the major work needed is to design a proper feeding circuit with microstrip lines such that for each of the two bands only one patch antenna is strongly excited (i.e., one patch is activated) at a time. To that end one needs to know the impedance characteristics of both patch antennas in both frequency bands. As reported earlier, they can be predicted very accurately with the simple cavity model theory. In short, this is simply a circuit design problem for which a solution can usually be found. But, as one can easily see, this approach does not lead to a dual-frequency antenna in the true sense, since it consists of really two antennas,

taking twice as much space and weight. A variation to this approach is to stack a small patch on the top of a larger one. This design again consists of two antennas, having a thickness twice as much. In addition, it requires some complicated feed structure. In array applications, it is believed that two separate conventional arrays, one for each frequency, can probably provide a better and simpler solution than a single array made of either one of these two types of elements.

One may wonder whether or not it is possible to design a dual-frequency microstrip antenna with only a single element. From our cavity model theory it is easy to see that any single element can resonate at many frequencies. But this is not sufficient. For a useful antenna, its pattern, polarization, and impedance should remain about the same, if not identical, for all frequency bands of interest. This immediately rules out many modes. For example, a rectangular patch can be designed to operate at two resonant frequencies corresponding to the (0,1) and (1,0) modes, even with nearly the same patterns and impedances, but unfortunately their radiated fields have completely different polarizations. As another example, a similar patch can be designed to operate for the (0,1) and (0,3) modal frequencies, both with broadside radiation patterns, same polarizations, and even similar impedances, but the two frequencies are always at a fixed ratio, about three in this case. This again severely restricts its usefulness.

In this report, two attempts are made to search for a solution to the problem just stated. In Part I, annular microstrip antennas are investigated in some detail. From the cavity model theory, such antennas if excited with (1,1), (1,2), (1,3), or even higher order mode, should all have broadside radiation with the same polarization. Unlike the rectangular or disk patches, the ratio of resonant frequencies for these modes could be adjusted over a wide range by choosing proper dimensions of inner and outer radii. A detailed study, in both theory and experiment, has shown that this approach is indeed feasible. Sets of design curves as well as some feeding methods are discussed in Part I.

The work reported in Part II is concentrated in the rectangular microstrip antennas, in particular for their operation in the (0,1) and (0,3) modes. Theoretical consideration predicts that electrically shorting pins, if placed on the nodal lines of the (0,3) modal field, could have a strong effect on the (0,1) modal resonant frequency but leave the (0,3) modal resonant frequency unaffected. Thus, in so doing, one obtains a great flexibility in the design of dual-frequency rectangular patch antennas. In fact, as will be seen later, the insertion of pins at proper locations can also be used advantageously to tune the impedance for a desired value for the (0,1) mode frequency while the feed location may be chosen first for the proper impedance in the (0,3) mode frequency band.

In both approaches, one may find that in some cases the antenna dimensions needed for the low frequency operation may become too

large for the high frequency band. As a result, grating lobes and/or large cross-polarized field may occur in the high band. In many cases they can be effectively reduced by using modal suppressing pins. Of course they can also be eliminated by using substrate of high permittivity, or using a modified version of the microstrip antenna. Finally, it should be remarked that although electrically shorting pins are considered in this report, other types of tuning elements can also be used for more flexibility. In fact, the multiport theory is applicable to any type of the elements.

PART I - Annular Microstrip Antennas and Their Applications to Dual-Frequency Operation

CHAPTER 1

INTRODUCTION

This thesis analyzes the properties of an annular ring microstrip antenna. Microstrip antennas are constructed of a generally thin layer of dielectric sandwiched between two layers of conducting material. One side of the cladding, the ground plane, is left intact, while the other can be selectively removed in order to form antennas of various geometries. The antennas studied in this paper were all constructed of 1/16" Rexolite 2200 surrounded by copper cladding.

The antenna can be fed using either a stripline or a coaxial feed. The coaxial feed, used here, has the advantage that the feed point can be easily changed to any point within the antenna.

Thin microstrip antennas are unique in their compactness in structure, low cost in production, and integrability with feeding networks. They are inherently limited in bandwidth, however, which, as shown previously, [1], depends mainly on the thickness of the substrate, not the patch geometry.

In order to extend their usefulness, it seems natural to ask whether thin microstrip antennas can be designed to operate for two or more discrete bands, if not for a single wide band. A dual frequency microstrip antenna has been reported [2] in which actually two patch antennas are used and interconnected with transmission lines. This is essentially a circuit problem since one is required to design a circuit so that interactions between the two patches in impedance and radiation patterns would be minimized.

A similar approach is to use a single patch connected to an impedance matching network [3]. Using a disc-shaped patch, a single resonance was split into two narrowly spaced operating bands. Both resonances, however, exhibit a narrow band of operation, and it is unclear whether these frequencies can be more widely spaced while retaining similar and useful radiation patterns for both bands.

A more interesting approach would be to design a single patch, without matching networks, which could operate at multiple frequency bands. A simple but highly accurate model has been developed for studying the properties of thin microstrip antennas [1,4,5,6]. The antenna is approximated as a closed lossy cavity, with the radiation properties dependent on the field at the edge of the cavity. From this cavity model one would expect that such a multiple frequency antenna is indeed possible, with frequencies resonant at various modes. Unfortunately, the multi-mode operation is generally restricted to frequencies of fixed ratio and may also result in vastly different radiation patterns and polarizations.

The annular patch, however, seems uniquely suited to the design of dual or multiple frequency antennas. As will be shown, the resonant frequencies of such antennas are not harmonically related. Further, the ratios between the various modes can be changed over a considerable range by adjusting the ratio of the inner to the outer radius.

In this paper, the closed cavity theory, previously developed, is applied to the annular microstrip antenna and examined in detail. The theoretical impedance and radiation characteristics are calculated and compared to experimental values.

With the basic theory outlined, the design of dual frequency antennas is studied, and a method for their construction developed. As will be shown, tunable annular patch antennas can be designed, without the need in matching networks, to operate at two or more frequencies with similar and useful radiation patterns and the same polarization.

Finally, the effects of fringing fields at the edges of the antenna on the resonant frequencies and impedance characteristics are examined, and a simple method to correct for these effects is put forward.

## CHAPTER 2

## ANALYSIS OF THE ANNULAR RING MICROSTRIP ANTENNA

In this chapter, the internal fields of the annular microstrip antenna are determined. Expressions for the stored energy, radiated power, and power lost in the copper cladding and the dielectric are then obtained. Finally, using these parameters, the driving point impedance and the antenna pattern are computed.

2-1 THE CAVITY MODEL

A rigorous calculation of the fields inside the antenna is prohibitively complex. To facilitate the calculation of the fields, a number of simplifying assumptions are made. The good agreement between analytic calculations and experimental data reported for microstrip antennas of other geometries supports the validity of such an approach.

The antenna is modelled as a closed cavity, bounded on top and bottom by perfect electric conducting (PEC) plates, and on the inner and outer edges by a perfect magnetic conducting (PMC) ribbon, as in Figure 2.1.

If the antenna is thin relative to a wavelength, the variation of the fields in the cavity with  $z$ , along the normal to the ground plane, will be negligible. Thus the fields are assumed independent of  $z$ . Since the tangential component of  $\vec{E}$  is zero at the top and bottom boundaries, this implies that the electric field has a component along the  $z$ -direction only, and that  $\vec{H}$  has transverse components with respect to  $\hat{z}$  only.



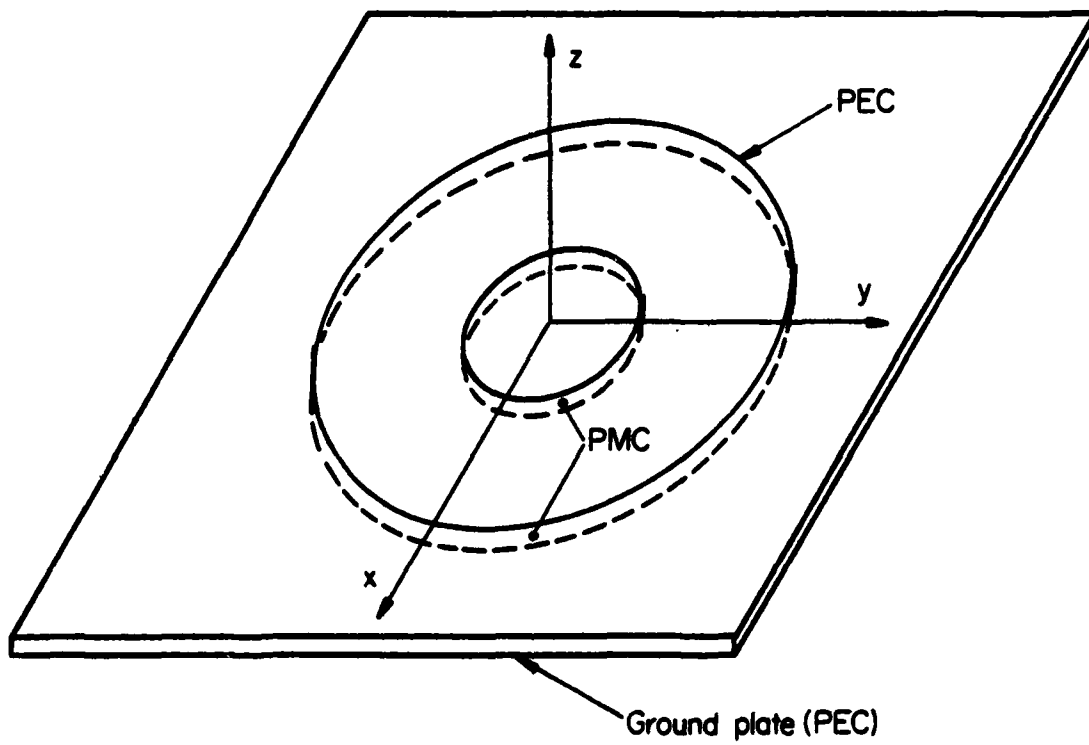


Figure 2-1: The antenna modelled as a closed cavity.

The presence of the bounding PMC ribbon is suggested, since, at the inner and outer edges, the radially directed electric surface current is very small. Therefore, the component of the magnetic field tangential to the edge is also expected to be small, and the introduction of the PMC ribbon, requiring the tangential H field to be equal to zero at the boundaries, should not greatly affect the internal fields.

The antenna modelled as a closed cavity does not, of course, radiate. The radiated power can be approximated once the internal fields of the closed cavity are known. Implicit in this method is the assumption that the shape of the internal field structure is essentially the same whether or not there is radiation through the edges, since the quality factor of thin microstrip antennas is high. The validity of this assumption is verified by experiment.

Although the cavity model accurately predicts the shape of the internal fields, it will be shown later that the amplitude of the field, that is, the coefficient that multiplies this distribution, differs greatly for the cavity and the radiating antenna. However, the amplitude of the field can be estimated if the quality factor of the antenna is known. Finally, with the field distribution completely determined, the impedance and radiation patterns can be calculated.

## 2-2 THE INTERNAL FIELD STRUCTURE

Two different, but equivalent, methods can be used to solve for the fields inside the antenna. With an expansion in resonant modes, the field is expressed as a double infinite series of orthogonal mode

functions, each of which satisfies the source-free wave equation and appropriate boundary conditions, while their sum, the total field, satisfies the source condition.

For the modal matching technique, the homogeneous wave equation is solved in each source-free region, and each source-free solution satisfies all boundary conditions, except at the interface between the two regions where the source is located. A complete solution is then determined by matching these solutions to the source. This generally results in the field being expressed as a single infinite series.

Starting from Maxwell's equations, and assuming a sinusoidal time dependence,  $\exp(j\omega t)$ , we have

$$\text{curl } \vec{H} = j\omega\epsilon\vec{E} + \vec{J} \quad (2.1)$$

$$\text{curl } \vec{E} = -j\omega\mu\vec{H} \quad (2.2)$$

which can be solved in terms of  $\vec{E}$ ;

$$\begin{aligned} -\nabla^2\vec{E} + \nabla \cdot (\nabla \cdot \vec{E}) &= \text{curl}(\text{curl } \vec{E}) = -j\omega\mu \text{curl } \vec{H} \\ &= -j\omega\mu(j\omega\epsilon\vec{E} + \vec{J}) \end{aligned} \quad (2.3)$$

In the above equations,  $\epsilon$  and  $\mu$  are the complex permittivity and permeability of the substrate, and  $\vec{J}$  is the feed current.

The assumptions that  $\vec{E}$  is along the  $\hat{z}$  direction only and dependent of  $z$ , as noted in section 2.1, imply

$$\nabla \cdot \vec{E} = 0 \quad (2.4)$$

so that (2.3) becomes

$$\nabla^2 \vec{E} + \omega^2 \mu \epsilon \vec{E} = j\omega \mu \vec{J} \quad (2.5)$$

Equation (2.5) can now be solved by the two methods outlined above.

### 2-2-1 THE RESONANT MODE EXPANSION METHOD

Each term in the expansion for  $\vec{E}$  must satisfy the homogeneous form of (2.5)

$$\nabla^2 \psi_{nm} + K_{nm}^2 \psi_{nm} = 0 \quad (2.6)$$

where  $K_{nm}$  is the eigenvalue.

In cylindrical coordinates this becomes

$$\frac{1}{\rho} \frac{\partial}{\partial \rho} \left( \rho \frac{\partial \psi_{nm}}{\partial \rho} \right) + \frac{1}{\rho^2} \frac{\partial^2 \psi_{nm}}{\partial \phi^2} + K_{nm}^2 \psi_{nm} = 0 \quad (2.7)$$

Assuming a separable solution,

$$\psi_{nm} = R(\rho) \phi(\phi) \quad (2.8)$$

$$\frac{1}{\rho} \frac{\partial}{\partial \rho} (\rho R'(\rho) \phi(\phi)) + \frac{1}{\rho^2} R(\rho) \phi''(\phi) + K_{nm}^2 R(\rho) \phi(\phi) = 0 \quad (2.9)$$

where one prime signifies differentiation of that function with respect to the argument once, two primes twice, and so on. Simplifying, we obtain

$$\frac{\rho}{R(\rho)} \frac{\partial}{\partial \rho} (\rho R'(\rho)) + K_{nm}^2 = \frac{-\phi''(\phi)}{\phi(\phi)} = n^2 \quad (2.10)$$

where  $n^2$  is a separation constant. Solving the separated equations, we have

$$\text{I.} \quad \phi''(\phi) + n^2 \phi(\phi) = 0 \quad (2.11)$$

$$\phi_n(\phi) = \cos n\phi \quad (2.12)$$

$$\text{II.} \quad \rho \frac{\partial}{\partial \rho} (\rho R'(\rho) + (K_{nm}^2 \rho^2 - n^2) R(\rho)) = 0 \quad (2.13)$$

$$R''(\rho) + \frac{1}{\rho} R'(\rho) + \left( K_{nm}^2 - \frac{n^2}{\rho^2} \right) R(\rho) = 0 \quad (2.14)$$

The solution of (2.15) is well known to be

$$R(K_{nm}\rho) = A J_n(K_{nm}\rho) + B N_n(K_{nm}\rho) \quad (2.15)$$

a linear combination of Bessel functions of the first kind,  $J_n(K_{nm}\rho)$ , and Neumann functions,  $N_n(K_{nm}\rho)$ .

The constants A and B in (2.15) are determined by satisfying the boundary condition that  $\vec{H} \cdot \hat{\phi} = 0$  for each mode at the boundaries  $\rho = a$  and  $\rho = b$ .

$$\text{Letting } \vec{E}_{nm} = A_{nm} \psi_{nm} \hat{z}, \quad (2.16)$$

from Maxwell's equations

$$\vec{H} = \frac{-1}{j\omega\mu} \text{curl } \vec{E} \quad (2.17)$$

$$\vec{H}_{nm} = \frac{-1}{j\omega\mu} \text{curl } (A_{nm} \psi_{nm} \hat{z}) \quad (2.18)$$

$$\vec{H}_{nm} = j \frac{A_{nm}}{\omega\mu} \left( \frac{\partial \psi_{nm}}{\rho \partial \phi} \hat{\rho} - \frac{\partial \psi_{nm}}{\partial \rho} \hat{\phi} \right) \quad (2.19)$$

Requiring  $\vec{H}_{\phi} = 0$  at the boundaries  $\rho = a, b$  implies

$$A J'_n(K_{nm}a) + B N'_n(K_{nm}a) = 0 \quad (2.20)$$

$$A J'_n(K_{nm} b) + B N'_n(K_{nm} b) = 0 \quad (2.21)$$

Therefore we have the characteristic equation for  $K_{nm}$

$$J'_n(K_{nm} a) N'_n(K_{nm} b) = J'_n(K_{nm} b) N'_n(K_{nm} a) \quad (2.22)$$

Let  $x = K_{nm} a$ ,  $\Lambda = b/a$ . This equation can be more conveniently written as

$$J'_n(x) N'_n(\Lambda x) = J'_n(\Lambda x) N'_n(x) \quad (2.23)$$

Given values for  $a$  and  $b$ , or  $\Lambda$ , the roots  $x$  of the above equation can be determined for various values of  $n$ . Some of these roots are given in Tables 2.1 and 2.2 for  $n = 1$  and  $n = 2$ . The roots are also shown graphically in Figures 2.2 and 2.3, as a function of  $\Lambda = b/a$ , the ratio of the outer radius to the inner radius.

One of the motivations for studying the annular ring antenna was to obtain a tunable antenna which operates at two frequencies with similar radiation patterns. From Figure 2.2, a graph for the resonances for  $n = 1$ , it is apparent that by changing  $\Lambda$ , the ratio of the outer to the inner radius, it is possible to vary widely the ratio between the first ( $m = 1$ ) and the 2nd ( $m = 2$ ) resonance. Indeed, as  $\Lambda$  varies from 1.5 to 12, the ratio of these two resonances changes from 7.92 to 2.85. As will be shown in Chapter 3, the radiation patterns for these resonances are very similar, so that the unique geometry of the annular ring antenna allows a great freedom in designing dual frequency antennas.

Table 2-1: Resonances for  $n=1$ ; values of  $x$ ,  $x = K_{nm} a$ , such that  
 $J_1'(x) N_1'(\Lambda x) = N_1'(x) J_1'(\Lambda x)$ .

$\Lambda \backslash m$	1.5	2.0	2.5	3.0
1	0.80509	0.67734	0.58471	0.51362
2	6.37652	3.28247	2.26364	1.75777
3	12.61287	6.35324	4.27330	3.23611
4	18.88053	9.47133	6.33924	4.77494
5	25.15599	12.60124	8.41951	6.32991

$\Lambda \backslash m$	4.0	5.0	6.0	7.0
1	0.41112	0.34102	0.29042	0.25240
2	1.25112	0.99217	0.83062	0.71780
3	2.20208	1.68661	1.37743	1.17060
4	3.21274	3.19865	1.96588	1.65479
5	4.24176	3.19865	2.57334	2.15782

$\Lambda \backslash m$	8.0	10.0	12.0	15.0
1	0.22291	0.18035	0.15123	0.12101
2	0.63335	0.51371	0.43223	0.34893
3	1.02177	0.81992	0.68749	0.55478
4	1.43264	1.13588	1.10714	0.96701
5	1.35955	1.32858	---	---

Table 2-2: Resonances for  $n=2$ ; values of  $x$ ,  $x = K_{nm} a$ , such that  
 $J_2'(x) N_2'(\Lambda x) = N_2'(x) J_2'(\Lambda x)$ .

$\Lambda \backslash m$	1.5	2.0	2.5	3.0
1	1.60806	1.34060	1.13696	0.97743
2	6.53808	3.53129	2.56640	2.09010
3	12.69280	6.47471	4.42238	3.40667
4	18.93369	9.55159	6.43666	4.88507
5	--	--	--	6.41125

$\Lambda \backslash m$	4.0	5.0	6.0	7.0
1	0.75232	0.60694	0.50743	0.43556
2	1.58931	1.29898	1.09728	0.94764
3	2.40580	1.90989	1.60448	1.38900
4	3.34281	2.57995	2.12651	1.82391
5	4.33619	3.30385	--	2.28122

$\Lambda \backslash m$	8.0	10.0	12.0	15.0
1	0.38139	0.30529	0.25447	0.20241
2	0.83265	0.66847	0.55804	0.44680
3	1.22489	0.98875	0.82725	0.67192
4	1.60398	1.29696	1.08806	0.88960
5	--	--	1.34385	--



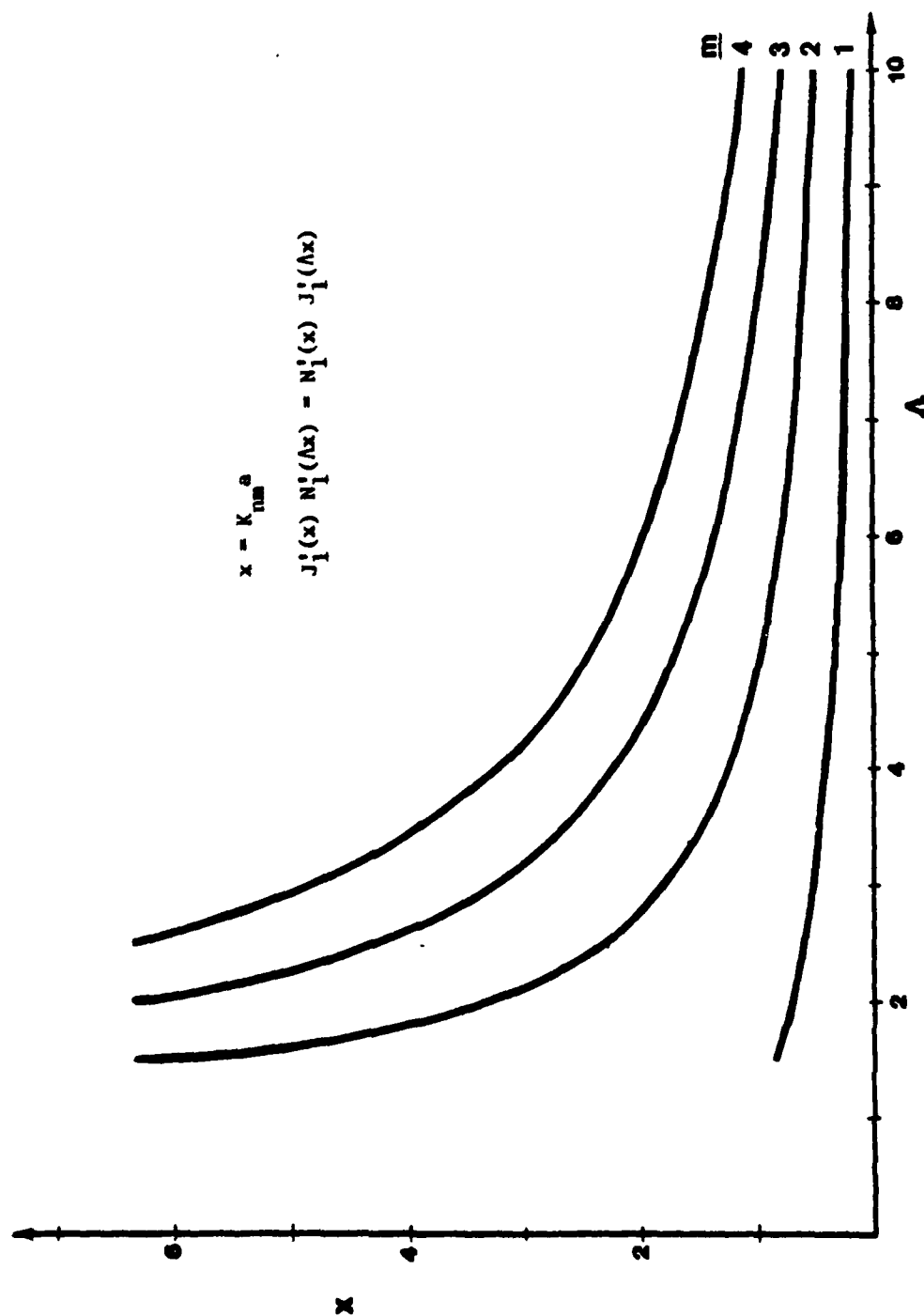


Figure 2-2: The roots,  $x$ , of equation (2.23), for  $n = 1$ , as a function of  $\Lambda$ .

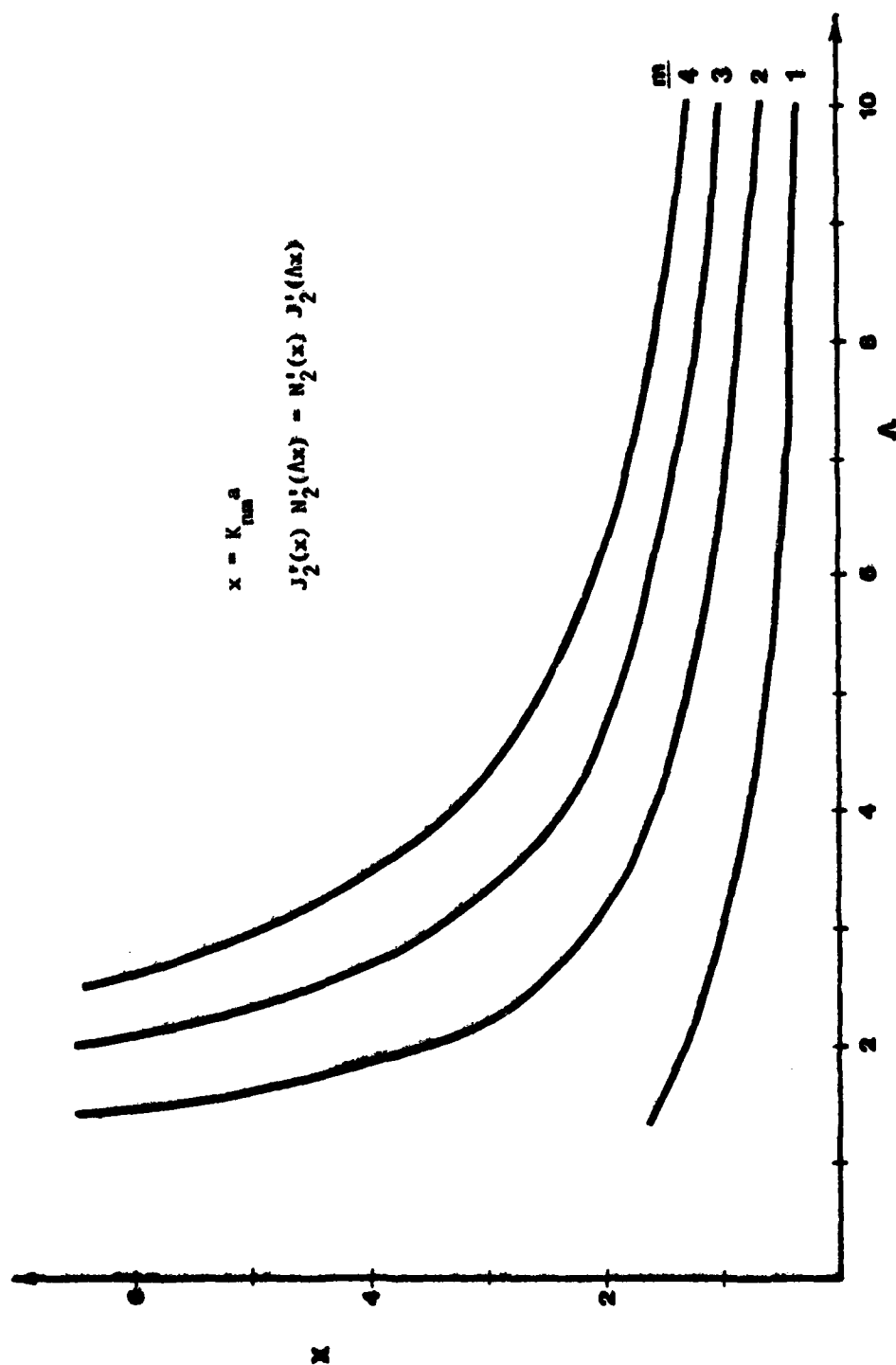


Figure 2-3: The roots,  $x$ , of equation (2.23), for  $n = 2$ , as a function of  $\lambda$ .

The solution to (2.14) is unique to only a multiplicative constant, so we take as a solution

$$\psi_{nm} = (N'_n(K_{nm}a) J_n(K_{nm}\rho) - J'_n(K_{nm}a) N_n(K_{nm}\rho)) \cos n\phi \quad (2.24)$$

The complete solution of  $E_z$  in terms of the resonant modes

$$E_z = \sum_{n=0}^{\infty} \sum_{m=0}^{\infty} A_{nm} \psi_{nm} \quad (2.25)$$

must satisfy the inhomogeneous wave equation

$$\nabla^2 E_z + K_1^2 E_z = j\omega\mu \vec{J} \quad (2.26)$$

where

$$K_1^2 = K_0^2 \epsilon(1 - j\delta)$$

$\epsilon$  = relative permittivity of the substrate

$\delta$  = loss tangent of the substrate

The values of the  $A_{nm}$ 's in (2.25) are dependent on the particular form of  $\vec{J}$ . Considering a point source at  $(\rho', \phi')$  with unit total current,

$$\vec{J} = \delta(\phi - \phi') \delta(\rho - \rho') / \rho \hat{z} \quad (2.27)$$

we can solve for the  $A_{nm}$ 's. (2.26) becomes, using (2.25)

$$(K_1^2 - K_{nm}^2) \sum_{n,m=0}^{\infty} A_{nm} \psi_{nm} = j\omega\mu \delta(\phi - \phi') \delta(\rho - \rho') / \rho \quad (2.28)$$

Multiplying by  $\psi_{pq}^*$  and integrating over the antenna,

$$\begin{aligned}
& \sum_{n,m=0}^{\infty} (K_1^2 - K_{nm}^2) A_{nm} \int_a^b \int_0^{2\pi} \psi_{nm} \psi_{pq}^* \rho d\rho d\phi \\
& = j\omega\mu \int_a^b \int_0^{2\pi} \psi_{pq}^* \delta(\phi - \phi') \delta(\rho - \rho') d\rho d\phi \quad (2.29)
\end{aligned}$$

By the orthogonality of the cosine functions, only when  $p, q = n, n$  will the left hand side of (2.29) not equal zero. Further, because of symmetry, we can take  $\phi' = 0$ . (2.29) becomes

$$(1 + \delta_{on}) \pi (K_1^2 - K_{nn}^2) A_{nn} \int_a^b \psi_{nn} \psi_{nn}^* \rho d\rho = j\omega\mu \psi_{nn}(\rho', \phi' = 0) \quad (2.30)$$

where  $\delta_{on}$  is the Kronecker delta.

Solving for the  $A_{nn}$ 's gives

$$A_{nn} = \frac{j\omega\mu \psi_{nn}(\rho', 0)}{(1 + \delta_{on}) \pi (K_1^2 - K_{nn}^2)} \left( \int_a^b \psi_{nn} \psi_{nn}^* \rho d\rho \right)^{-1} \quad (2.31)$$

This along with (2.25) determines the complete solution for  $\vec{E}(\rho, \phi; \rho', 0)$ .

$$\vec{E}(\rho, \phi; \rho', 0) = E_z \hat{z} = \hat{z} \sum_{n,m=0}^{\infty} A_{nm} \psi_{nm}(\rho, \phi) \quad (2.25)$$

which is the field at  $(\rho, \phi)$  due to a unit current point source at  $(\rho', 0)$ . For a point source at  $(\rho', \phi')$ ,

$$\vec{E}(\rho, \phi; \rho', \phi') = \vec{E}(\rho, \phi - \phi'; \rho', 0) \quad (2.32)$$

The actual feed is not, of course, a point source. It can be idealized, however, by assuming a rectangular distribution in  $\phi$ , with a total feed current of one ampere, concentrated at a radius  $\rho'$ . as in Figure 2.4:

$$\vec{J} = \begin{cases} \frac{1}{2\phi_w} \delta(\rho - \rho') & , \quad -\phi_w < \phi < \phi_w ; \\ 0 & , \quad \text{otherwise} \end{cases} \quad (2.33)$$

This choice for the current distribution, while somewhat arbitrary, has yielded good agreement between experimental measurements and theoretical calculations of the impedance loci of various antennas. It is probable that other models for the antenna feed could be used, also with good results.

The field due to this extended source is easily found by convolution of the Green's function (2.32) and the source function (2.33).

$$\vec{E}(\rho, \phi) = \int_{\rho} \int_{\phi} \vec{E}(\rho, \phi; \rho', \phi') \vec{J}(\rho', \phi') \rho d\rho' d\phi' \quad (2.34)$$

Because of the presence of the delta function, the integration over  $\rho'$  is trivial. Carrying out the integration over  $\phi'$  we obtain

$$\begin{aligned} \vec{E}(\rho, \phi) = & \sum_{n,m=0}^{\infty} A_{nm} [N'_n(K_{nm}a) J_n(K_{nm}\rho) - J'_n(K_{nm}a) N_n(K_{nm}\rho)] \\ & \cdot \left[ \frac{\sin n\phi_w}{n\phi_w} \right] \end{aligned} \quad (2.35)$$

with  $A_{nm}$  as given in (2.31).

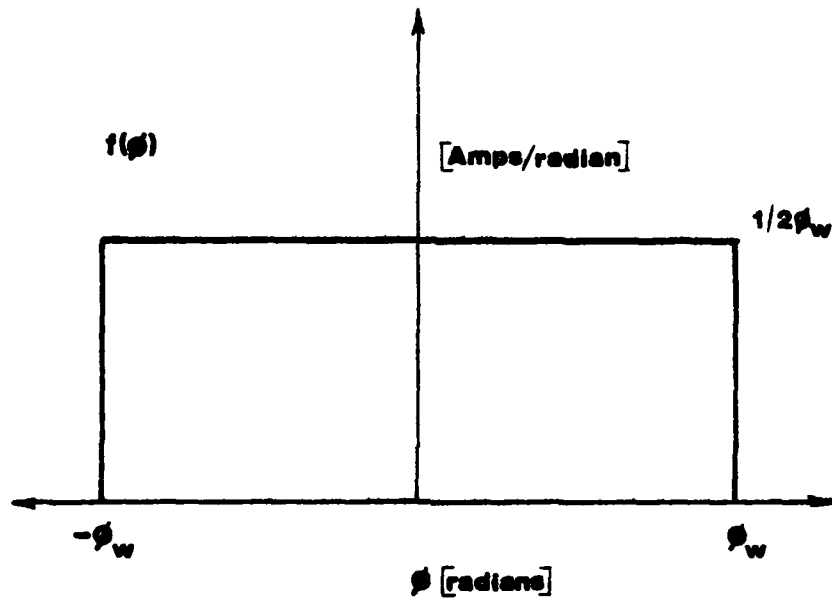


Figure 2-4: The source current distribution.

### 2-2-2 EXPANSION USING MODAL-MATCHING TECHNIQUE

In the modal-matching analysis, the homogeneous equation

$$\nabla^2 \psi_n + K_1^2 \psi_n = 0 \quad (2.36)$$

is solved in each source-free region, satisfying the appropriate boundary conditions. The total solution is then found by matching these separate partial solutions to the source constraints. The source current

$$\vec{J} = f(\phi) \delta(\rho - \rho') / \rho' \hat{z} \quad (2.37)$$

is considered to be located at a radius  $\rho'$ , dividing the disc into two source-free regions; Region I for  $\rho > \rho'$ , Region II for  $\rho < \rho'$ . (See Figure 2.5.) The current distribution  $f(\phi)$  is the same as that used in the resonant mode expansion (Figure 2.4), a rectangular distribution in  $\phi$ , with a total feed current of one ampere.

With  $f(\phi)$  chosen,  $\vec{J}$  can be represented in terms of its Fourier components

$$\vec{J} = \frac{\delta(\rho - \rho')}{\rho'} \sum_{n=0}^{\infty} a_n \cos n\phi \quad (2.38)$$

where

$$a_0 = \frac{1}{2\pi} \int_{-\phi_w}^{\phi_w} \frac{1}{2\phi_w} d\phi = \frac{1}{2\pi} \quad (2.39)$$

and

$$a_n = \frac{1}{\pi} \int_{-\phi_w}^{\phi_w} \left( \frac{1}{2\phi_w} \right) \cos n\phi d\phi = \frac{1}{\pi} \frac{\sin(n\phi_w)}{n\phi_w} \quad (2.40)$$

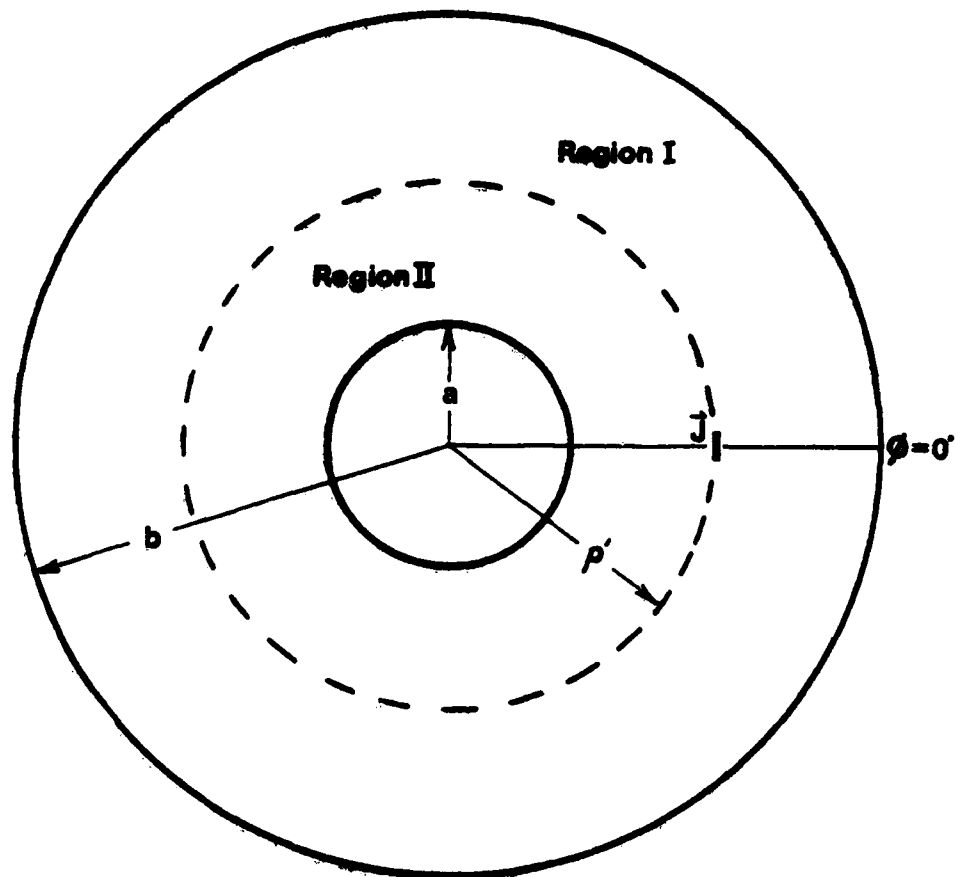


Figure 2-5: The annular antenna modelled in the mode-matching technique.



so that  $\vec{J}$  can be written

$$\vec{J} = \hat{z} \sum_{n=0}^{\infty} \frac{\delta(\rho - \rho')}{\pi \rho' (1 + \delta_{0n})} \frac{\sin(n\phi_w)}{n\phi_w} \cos n\phi \quad (2.41)$$

where it is understood that for  $n = 0$ ,  $\sin(n\phi_w)/n\phi_w$  is taken equal to one.

Returning to the solution of (2.36), in Region I,  $\rho' < \rho < b$ ,

$$E_1 = \sum_{n=0}^{\infty} [A_n J_n(K_1 \rho) + B_n N_n(K_1 \rho)] \cos n\phi \quad (2.42)$$

Requiring that  $H_\phi = 0$  at the edge of the disc ( $\rho = b$ ), and using (2.20) gives

$$A_n J'_n(K_1 b) + B_n N'_n(K_1 b) = 0 \quad (2.43)$$

where the prime indicates differentiation with respect to the entire argument.

Similarly, in Region II,  $a < \rho < \rho'$ ,

$$E_2 = \sum_{n=0}^{\infty} (C_n J_n(K_1 \rho) + D_n N_n(K_1 \rho)) \cos n\phi \quad (2.44)$$

and at  $\rho = a$ , the inner radius,  $\partial E / \partial \rho = 0$  again, so that

$$C_n J'_n(K_1 a) + D_n N'_n(K_1 a) = 0 \quad (2.45)$$

Two additional boundary conditions must be applied to (2.42) and (2.44) at the source. At  $\rho'$ , the electric field must be continuous, since no magnetic current source is present.

$$A_n J_n(K_1 \rho') + B_n N_n(K_1 \rho') = C_n J_n(K_1 \rho') + D_n N_n(K_1 \rho') \quad (2.46)$$

Finally, the field must satisfy the source condition at  $\rho'$

$$\hat{\rho} \times (H_1 - H_2) \hat{\phi} = \vec{J} \quad (2.47)$$

Since  $H_{\phi} = \frac{-1}{\omega \mu} \frac{\partial E}{\partial \rho}$ , this implies

$$\begin{aligned} A_n J'_n(K_1 \rho') + B_n N'_n(K_1 \rho') - C_n J'_n(K_1 \rho') - D_n N'_n(K_1 \rho') \\ = \frac{j\omega \mu}{K_1 \pi \rho' (1 + \delta_{on})} \frac{\sin(n\phi_w)}{(n\phi_w)} \end{aligned} \quad (2.48)$$

Solving for  $A_n$  to  $D_n$  in the four equations (2.43), (2.45), (2.46), and (2.48) gives

$$A_n = \frac{CN'_n(K_1 b) [J'_n(K_1 a) N_n(K_1 \rho') - N'_n(K_1 a) J_n(K_1 \rho')]}{\Delta_n} \quad (2.49)$$

$$B_n = \frac{-CJ'_n(K_1 b) [J'_n(K_1 a) N_n(K_1 \rho') - N'_n(K_1 a) J_n(K_1 \rho')]}{\Delta_n} \quad (2.50)$$

$$C_n = \frac{CN'_n(K_1 a) [J'_n(K_1 b) N_n(K_1 \rho') - N'_n(K_1 b) J_n(K_1 \rho')]}{\Delta_n} \quad (2.51)$$

$$D_n = \frac{-CJ'_n(K_1 a) [J'_n(K_1 b) N_n(K_1 \rho') - N'_n(K_1 b) J_n(K_1 \rho')]}{\Delta_n} \quad (2.52)$$

where

$$C = \frac{i\omega\mu}{2} \frac{\sin(n\phi_w)}{n\phi_w} \quad (2.53)$$

and

$$\Delta_n = (1 + \delta_{on})(N'_n(K_1 a) J'_n(K_1 b) - J'_n(K_1 a) N'_n(K_1 b)) \quad (2.54)$$

The above equations, together with (2.42) and (2.44) can be used to calculate the electric field within the antenna.

### 2-3 RADIATED POWER

With the calculation of the electric fields within the antenna, a magnetic current source  $\vec{K}(\rho, \phi) = \hat{z} E(\rho, \phi) \times \hat{n}$  can be defined at the edge of the ring. This Huygen source is used to calculate approximately the ring's radiation pattern.

At the boundaries  $\rho = a$  and  $b$

$$E(b, \phi) = \sum_{n=0}^{\infty} (A_n J_n(K_1 b) + B_n N_n(K_1 b)) \cos n\phi = \sum_{n=0}^{\infty} K_b(n) \cos n\phi \quad (2.55)$$

$$E(a, \phi) = \sum_{n=0}^{\infty} (C_n J_n(K_1 a) + D_n N_n(K_1 a)) \cos n\phi = \sum_{n=0}^{\infty} K_a(n) \cos n\phi \quad (2.56)$$

so that

$$\vec{K}_s = \hat{z} E \times \hat{n} = \sum_{n=0}^{\infty} [K_b(n) \delta(\rho - b) - K_a(n) \delta(\rho - a)] \cos n\phi \quad (2.57)$$

The electric vector potential  $\vec{F}(\vec{r})$  due to a source at  $\vec{r}'$  is

$$\vec{F}(\vec{r}) = \frac{1}{4\pi} \int \frac{\vec{K}(\vec{r}')}{|\vec{r} - \vec{r}'|} \exp(-jK_0 |\vec{r} - \vec{r}'|) dv' \quad (2.58)$$

where

$$dv' = \rho' d\rho' d\phi' dz' \quad (2.59)$$

the integration being carried out over the magnetic source.

In the far field approximation

$$\begin{aligned} -jK_0 |\vec{r} - \vec{r}'| &= r - x' \cos\phi \sin\theta - y' \sin\theta \sin\phi \\ 1/|\vec{r} - \vec{r}'| &= 1/r \end{aligned} \quad (2.60)$$

so that

$$\vec{F}(\vec{r}) = \frac{\exp(-jK_0 r)}{2\pi r} \int \vec{K}(\vec{r}') \exp(jK_0 (x' \sin\theta \cos\phi + y' \sin\theta \sin\phi)) dv' \quad (2.61)$$

Considering the source current at  $\rho = b$  only, we have, since

$$\hat{\phi} = -\hat{x} \sin\phi' + \hat{y} \cos\phi' \quad (2.61a)$$

$$\begin{aligned} \begin{pmatrix} F_{xb} \\ F_{yb} \end{pmatrix} &= \frac{t \exp(-jK_0 r)}{2\pi r} \sum_{n=0}^{\infty} K_b(n) b \int_0^{2\pi} \cos n\phi' \begin{pmatrix} -\sin\phi' \\ \cos\phi' \end{pmatrix} \\ &\quad \cdot \exp(jK_0 b \sin\theta \cos(\phi' - \phi)) d\phi' \end{aligned} \quad (2.62)$$

where  $K_b(n)$  is defined as in (2.55), the factor of  $t$  is due to integrating over  $z$ , and a factor of 2 has been added for the presence of the ground plane.

Let

$$C(r) = \frac{t \exp(-jK_0 r)}{2\pi r} \quad (2.63)$$

and

$$\alpha_b = K_0 b \sin \theta \quad (2.64)$$

(2.62) becomes

$$\begin{pmatrix} F_{xb} \\ F_{yb} \end{pmatrix} = C(r) \sum_{n=0}^{\infty} K_b(n) \cdot b \int_0^{2\pi} \cos n\phi' \begin{pmatrix} -\sin\phi' \\ \cos\phi' \end{pmatrix} \exp[j\alpha_b \cos(\phi' - \phi)] d\phi' \quad (2.65)$$

Using the relation

$$\exp(j\alpha \cos\phi) = \sum_{m=-\infty}^{\infty} (j)^m J_m(\alpha) \exp(im\phi) = 2 \sum_{m=0}^{\infty} \frac{(j)^m}{1 + \delta_{m0}} J_m(\alpha) \cos m\phi \quad (2.66)$$

$$\begin{pmatrix} F_{xb} \\ F_{yb} \end{pmatrix} = C(r) \sum_{n=0}^{\infty} K_b(n) \cdot 2 \cdot b \sum_{m=0}^{\infty} \frac{(j)^m J_m(\alpha_b)}{1 + \delta_{m0}} \int_0^{2\pi} \begin{pmatrix} -\sin\phi' \\ \cos\phi' \end{pmatrix} \cdot \cos n\phi' \cos m(\phi' - \phi) d\phi' \quad (2.67)$$

The orthogonality of the cosine terms under the integral allows the double summation to be expressed simply as single summation over  $m$ .

$$\begin{pmatrix} F_{xb} \\ F_{yb} \end{pmatrix} = C(r) \cdot \pi \cdot b \left\{ \begin{pmatrix} 0 \\ K_b(1) J_0(\alpha_b) \end{pmatrix} + \sum_{m=1}^{\infty} (j)^m J_m(\alpha_b) \begin{pmatrix} K_b(m+1) + (1 + \delta_{m1}) K_b(m-1) \end{pmatrix} \begin{pmatrix} \sin m\phi \\ \cos m\phi \end{pmatrix} \right\} \quad (2.68)$$

The calculation of the electric vector potential due to the source at the inner radius  $a$  is essentially the same as above, substituting  $a$  for  $b$ , and noting that  $\hat{z} \times \hat{n} = -\hat{\phi}$ , where  $\hat{n}$  is now the inward normal at  $\rho = a$ . Let

$$\alpha_a = K_0 a \sin\theta \quad (2.69)$$

The total electric vector potential is

$$\begin{aligned} \begin{pmatrix} F_x \\ F_y \end{pmatrix} &= C(r) \cdot \pi \left\{ \begin{pmatrix} 0 \\ K_b(1) \cdot b \cdot J_0(\alpha_b) - K_a(1) \cdot a \cdot J_0(\alpha_a) \end{pmatrix} \right. \\ &+ \left[ \sum_{m=1}^{\infty} (j)^m J_m(\alpha_b) \cdot b [K_b(m+1) + (\delta_{m1} + 1) K_b(m-1)] \right. \\ &\left. \left. - \sum_{m=1}^{\infty} (j)^m J_m(\alpha_a) \cdot a [K_a(m+1) + (\delta_{m1} + 1) K_a(m-1)] \right] \begin{pmatrix} \sin m\phi \\ \cos m\phi \end{pmatrix} \right\} \\ &\quad (2.70) \end{aligned}$$

which can be represented in spherical coordinates as

$$F_\theta = F_x \cos\theta \cos\phi + F_y \cos\theta \sin\phi \quad (2.71)$$

$$F_\phi = F_x \sin\phi + F_y \cos\phi$$

In the far field

$$\vec{E}(\vec{r}) = \nabla \times \vec{F}(\vec{r}) = -jK_0 \hat{r} \times \vec{F}(\vec{r}) + O(1/r^2) \quad (2.72)$$

so that the electric field can be written

$$E_{\theta} = \eta_0 H_{\phi} = jK_0 F_{\phi} = jK_0 (F_y \cos\phi - F_x \sin\phi) \quad (2.73)$$

$$E_{\phi} = -\eta_0 H_{\theta} = -jK_0 F_{\theta} = -jK_0 (F_x \cos\theta \cos\phi - F_y \cos\theta \sin\phi)$$

where  $\eta_0$  is the free space impedance, 377 ohms.

The total radiated power,  $P_{\text{rad}}$ , can be determined by integrating the Poynting vector over the entire hemisphere.

$$P_{\text{rad}} = \int_0^{\pi/2} \int_0^{2\pi} (E_{\theta} H_{\phi}^* - E_{\phi} H_{\theta}^*) r^2 \sin\theta \, d\phi d\theta \quad (2.74)$$

In practice, although the integration over phi can be written in closed form, (2.74) is evaluated by a double numerical integration routine.

#### 2-4 STORED ENERGY

The time-averaged electric stored energy,  $W_E$ , of the antenna

$$W_E = \frac{\epsilon}{2} \int_V |E|^2 \, dv \quad (2.75)$$

is easily calculated, since the fields are separable in  $\rho$ ,  $\phi$ , and  $z$ . The electric fields calculated in (2.42) and (2.44) can be expressed

$$E_1 = \sum_{n=0}^{\infty} P_n(K_1 \rho) \cos n\phi \quad (2.76)$$

$$E_2 = \sum_{n=0}^{\infty} Q_n(K_1 \rho) \cos n\phi \quad (2.77)$$

where

$$P_n(K_1 \rho) = A_n J_n(K_1 \rho) + B_n N_n(K_1 \rho) \quad (2.78)$$

$$Q_n(K_1 \rho) = C_n J_n(K_1 \rho) + D_n N_n(K_1 \rho)$$

so that the electric stored energy is

$$W_E = \frac{\epsilon t}{2} \sum_{m=0}^{\infty} \sum_{n=0}^{\infty} \left( \int_{\rho'}^b P_m(K_1 \rho) P_n^*(K_1 \rho) \rho d\rho + \int_a^{\rho'} Q_m(K_1 \rho) Q_n^*(K_1 \rho) \rho d\rho \right) \cdot \int_0^{2\pi} \cos m\phi \cos n\phi d\phi \quad (2.79)$$

with the integration over  $z$  already carried out. Because of the orthogonality of the cosine terms in the integral, (2.79) reduces to

$$W_E = \frac{\epsilon t \pi}{2} \sum_{n=0}^{\infty} (1 + \delta_{0n}) \left( \int_{\rho'}^b |P_n(K_1 \rho)|^2 \rho d\rho + \int_a^{\rho'} |Q_n(K_1 \rho)|^2 \rho d\rho \right) \quad (2.80)$$

where the above integrals can be evaluated in closed form (Appendix A).

Since we are interested in the stored energy only near resonance, it is not necessary to compute the magnetic stored energy, because, at resonance, the energy stored in the magnetic field equals  $W_E$ .

## 2-5 DIELECTRIC LOSS

The power absorbed by the dielectric,  $P_d$ , is

$$P_d = \sigma \int |E|^2 dv \quad (2.81)$$



This can clearly be expressed in terms of  $W_E$  which has already been determined in section 2.4. Therefore, in terms of the dielectric loss tangent,  $\delta = \frac{\sigma}{\omega \epsilon}$ ,

$$P_d = 2 \omega \delta W_E \quad (2.82)$$

## 2-6 COPPER LOSS

Rigorously, the copper loss is due to both the  $\vec{H}$  field and  $\vec{E}$  field at the plates. The effect due to the normal  $\vec{E}$  field is generally negligible for good conductors, however, and only that due to the tangential  $H$  field will be calculated.

For a good conductor, the skin depth,  $\Delta$ , is

$$\Delta = \left( \frac{2}{\omega \mu \sigma} \right)^{1/2} \quad (2.83)$$

and for conductors much thicker than the skin depth, the current density  $\vec{J}_v$  can be approximated by

$$|\vec{J}_v| = |\vec{J}_s| \exp(-z/\Delta)/\Delta \quad (2.84)$$

where  $\vec{J}_s$  is the surface current.

The power dissipated in the copper,  $P_{cu}$ , is

$$P_{cu} = \frac{1}{\sigma} \int_v |\vec{J}_v|^2 dv \quad (2.85)$$

with the integration: over  $v$ , the volume of copper. Substituting for  $|\vec{J}_v|$ , we have

$$P_{cu} = \frac{2}{\sigma \Delta^2} \int_{z=0}^{\infty} \exp(-2z/\Delta) \int_a^b \int_0^{2\pi} |\vec{J}_s|^2 \rho d\rho d\phi \quad (2.86)$$

where the factor of  $z$  takes into account both top and bottom conducting plates. Since  $\vec{H}$  has tangential components to the conducting surface only,  $|\vec{J}_s| = |\vec{H}|$ , and with the independence of  $\vec{H}$  over  $z$ ,

$$\int_a^b \int_0^{2\pi} |\vec{J}_s| \rho d\rho d\phi = \frac{2}{\mu t} \left( \frac{\mu}{2} \right) \int_v |\vec{H}|^2 dv \quad (2.87)$$

$P_{cu}$  thus becomes

$$P_{cu} = \frac{2W_M}{\sigma \Delta \mu t} = \frac{\Delta \omega W_M}{t} \quad (2.88)$$

where  $W_M$  is the time-averaged magnetic stored energy. Near resonance, where the energies stored in the electric and magnetic fields are equal, the copper loss can finally be expressed as

$$P_{cu} = \frac{\Delta \omega W_E}{t} \quad (2.89)$$

## 2-7 THE DISTRIBUTED SYSTEM

It was stated without proof in section 2.1 that the cavity model accurately predicts the shape of the internal fields of the antenna, but not its amplitude.

From section 2.2, the electric field in the cavity at a point  $(\rho, \phi)$  due to a source at  $(\rho', \phi')$  can be expressed

$$E(\rho, \phi; \rho', \phi') = \sum_{n,m=0}^{\infty} \frac{C_{nm} \psi_{nm}(\rho, \phi) \psi_{nm}(\rho', \phi')}{K_1^2 - K_{nm}^2} \quad (2.90)$$

where the  $C_{nm}$ 's are constant multipliers. Near resonance, where  $K_1$  approaches  $K_{nm}$ , only the single resonance term is important, and the expression in the denominator approaches  $-j\omega^2\mu\epsilon\delta$ , so that the magnitude is critically dependent on the imaginary part,  $\delta$ , of the wave number, whereas the shape of the distribution, determined largely by the single modal function, is not.

The loss tangent accounts only for losses in the cavity due to the dielectric, while the actual antenna loses power in radiation and through heating of the copper cladding. Equation (2.82) suggests the introduction of an "effective loss tangent,"  $\delta_{eff}$ , to account for this additional loss

$$\delta_{eff} = \frac{P_T}{2\omega W_E} \quad (2.91)$$

where  $P_T = P_{rad} + P_{cu} + P_d$ , the total power dissipated by the antenna. Under this approximation, the power lost by the antenna is thus redistributed throughout the field. A modified wave number

$$K = \omega[\mu\epsilon(1 - j\delta_{eff})]^{1/2} \quad (2.92)$$

can then be defined, and used to recalculate the fields within the antenna. The stored energy and power lost can then be recalculated and a new  $\delta_{eff}$  defined. In practice, this iterative method converges to a value for  $\delta_{eff}$  that agrees with experiment after a single iteration. This result is expected, since, for thin microstrip antennas, the Q-factor is generally high, 100-200, and the exact allocation of the losses becomes unimportant.

2-8 THE INPUT IMPEDANCE

The input impedance can be found from

$$z_{in} = -V/I \quad (2.93)$$

where  $V$  is the driving point voltage, and  $I$  is the source current.

If we choose  $I =$  one ampere, since the fields are independent of  $z$ ,

$$z_{in} = -tE_z \quad (2.94)$$

where  $t$  is the thickness of the dielectric. To account for the finite size of the feed, the voltage is averaged over the feed width. From section 2.2, the input impedance becomes

$$z_{in} = t \sum_{n=0}^{\infty} \frac{-j\omega\mu}{(1 + \delta_{on})\Delta_n} [N'_n(K_1 a)J_n(K_1 \rho') - J'_n(K_1 a)N_n(K_1 \rho')] \\ [N'_n(K_1 b)J_n(K_1 \rho') - J'_n(K_1 b)N_n(K_1 \rho')] \frac{\sin^2(n\phi_w)}{(n\phi_w)^2} \quad (2.95)$$

The validity of this averaging process is again to be justified by experiment.

### CHAPTER 3

#### ANALYTIC AND EXPERIMENTAL RESULTS

The impedance characteristics and radiation patterns of a variety of antennas with differing  $\Delta$ 's were studied. As will be discussed in Chapter 4, in order to obtain better agreement between theory and experiment it was necessary to modify the antenna dimensions used in calculations by a small amount to account for the fringing effect at the edges of the antenna. Unless specifically noted, all calculated results in this chapter are based on this corrected model. The dimensions given for these antennas are the actual physical measurements, with modified values following them in parentheses.

##### 3-1 THE LOSS TANGENT AND SKIN DEPTH

The calculated value of the effective loss tangent,  $\delta_{eff}$ , clearly depends on the values used for the dielectric loss tangent and copper conductivity. These factors have been previously measured as a function of frequency [7], and the values used here have been noted on the figures of the various microstrip patches.

##### 3-2 THE QUALITY FACTOR

As discussed in chapter 2, the effective loss tangent of the antenna must be determined in order to calculate an effective wave number, and thus the impedance of the antenna, if we define Q, the quality factor, by

$$Q = \frac{\omega \cdot \text{stored energy}}{\text{total power loss}} \quad (3.1)$$

At resonance, where the power stored in the magnetic and electric fields are equal, the quality factor is

$$Q = \frac{2\omega W_E}{P_T} \quad (3.2)$$

where  $P_T$  is the total power lost by the antenna. Comparing (3.2) to (2.91), the definition of  $d_{\text{eff}}$ , it is clear that the effective loss tangent is just the reciprocal of the quality factor of the antenna.

The quality factors measured for these annular antennas, ranging from 100 to 250, agree with those measured for microstrip antennas of other geometries. Such high quality factors demonstrate that the antenna loss is indeed small, as was originally assumed in redistributing the loss throughout the antenna.

### 3-3 THE RESONANCE FREQUENCY

The resonance frequencies predicted by the characteristic equation (2.23) agree quite well with the experimentally measured values. Tables 3-1 and 3-2 compare theory and experiment for two antennas with  $\Lambda = 6.00$  (6.82) and 2.0 (2.16),  $a = 1.50$  (1.342) cm and 3.24 (3.082) cm, for various modes. In most cases, the deviations are less than 1%.

The edge correction was chosen equal to the thickness of the dielectric, .138 cm, primarily in order to explain the large deviations between theory and experiment at high frequencies (see chapter 4). As

Table 3-1: The calculated and measured resonance frequencies (MHz) for the annular microstrip antenna of Figure 3-1,  $a = 1.5$  (1.342) cm,  $\Lambda = 6.0$  (6.82), edge correction = .158 cm.

(n,m)	Calculated Resonant Frequency	Measured Resonant Frequency	Deviation %
(1,1)	570	573.4	.61
(2,1)	978	989.8	1.19
(1,2)	1620	1625	.30
(2,2)	2137	2137.7	.03
(1,3)	2638	2625	.49

Table 3-2: The calculated and measured resonance frequencies (MHz) for the annular microstrip antenna of Figure 3-2,  $a = 3.24(3.082)$  cm,  $\Lambda = 2.0$  (2.16), edge correction = .158 cm.

(n,m)	Calculated Resonant Frequency	Measured Resonant Frequency	Deviation %
(1,1)	622	635.0	2.05
(2,1)	1220	1250.8	2.46
(3,1)	1829	1829.6	.03
(4,1)	2340	2370.5	1.3
(5,1)	2820	2854.0	1.2
(1,2)	2786	2810.3	.87
(2,2)	3006	3075.0	2.3
(3,2)	3418	3417.4	.02
(4,2)	3897	3890.2	.17

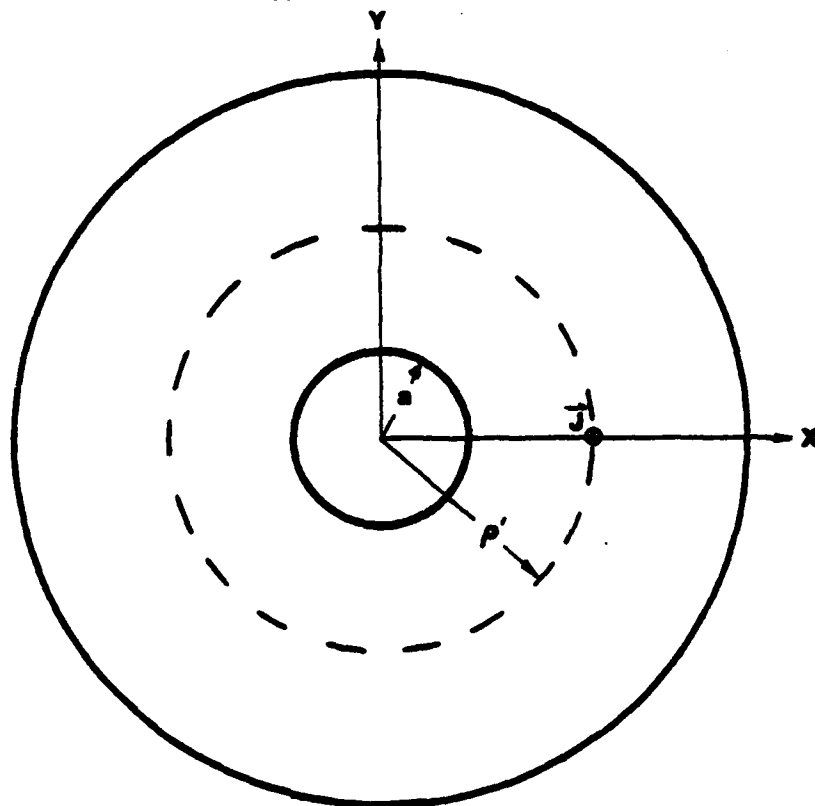


such, the agreement at lower frequencies is relatively worse, but the largest deviation is still only 2.46%. It is also possible that the effect of the fringing fields differs for low and high frequencies, and so a single edge correction, applied at all resonances, will not yield equally good agreement between theory and experiment for all resonant frequencies.

#### 3-4 THE INPUT IMPEDANCE AND RADIATION PATTERN

With the effective wave number determined, the theoretical driving point impedance can be calculated. Figures 3-1-a and 3-1-b show both the calculated and measured impedance patterns, plotted on a Smith chart, for the (1,1) and (1,2) modes of the antenna of Figure 3-1, with  $\Lambda = 6.0$  (6.82). It is clear that the theory outlined is in good agreement with experiment, and that the losses have been correctly accounted for.

The calculated and measured radiation patterns of these same two modes are shown in Figures 3-1-c and 3-1-d. Again, the agreement is quite good. The measured pattern for the (1,1) mode shows a markedly higher cross-polarized component than the theory predicts, although this might be expected since the E field at the edges of the antenna is not exactly z directed, as was assumed with the simple cavity model. The similarity of the radiation patterns of the two modes should be noted, as this characteristic is important in designing dual frequency antennas, a topic which will be more fully treated in the next section.



$\Lambda = 6.0$  (6.82)

$a = 1.5$  (1.342) cm

Thickness = .158 cm

Dielectric constant = 2.62

(1,1) mode

$\rho' = 4.5$  cm

Skin depth = .00038 cm

Loss tangent = .0008

Quality factor = 125

(1,2) mode

$\rho' = 1.5$  (1.342) cm

Skin depth = .00025 cm

Loss tangent = .001

Quality factor = 99

Figure 3-1. The annular microstrip antenna  $\Lambda = 6.0$  (6.82).

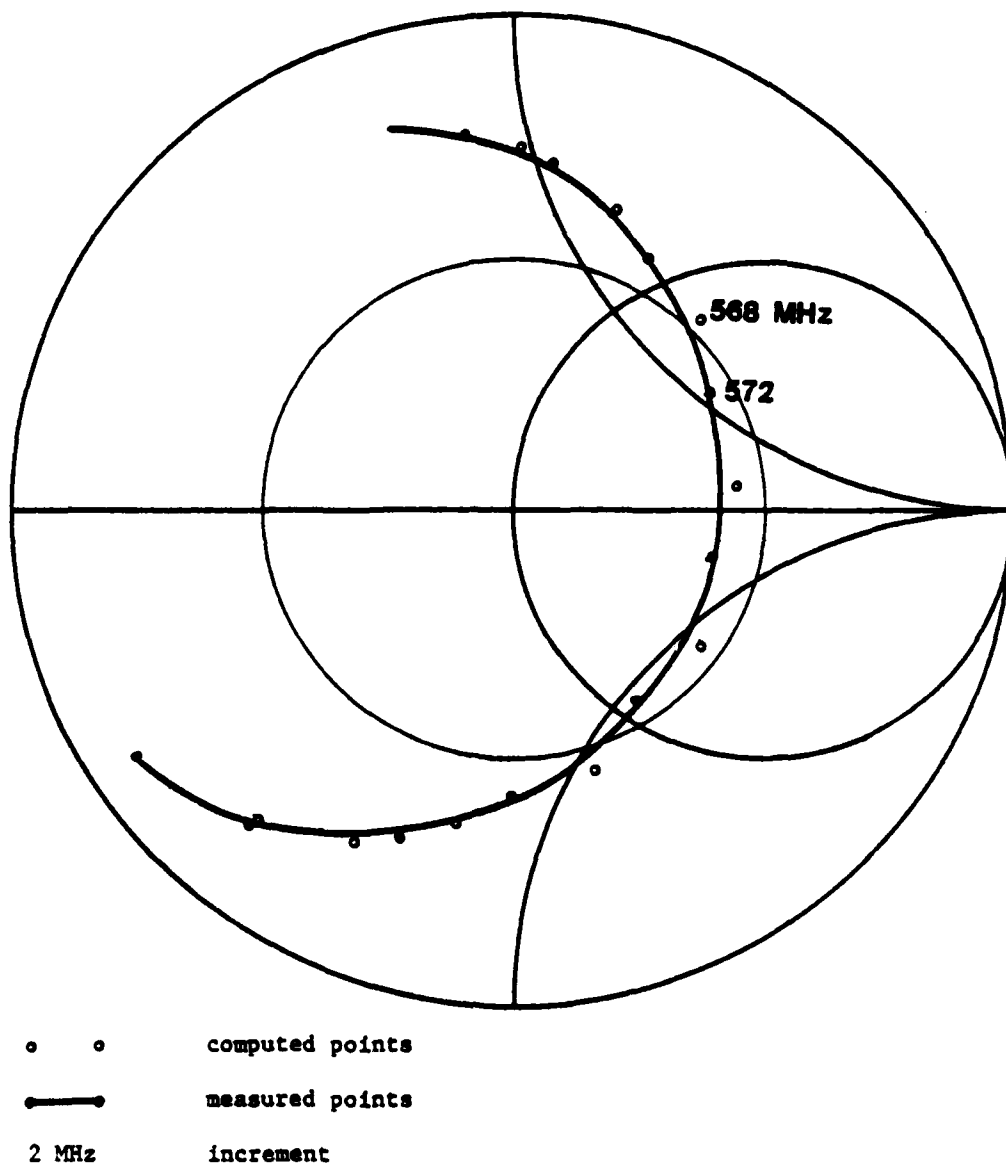


Figure 3-1-a: Calculated and measured input impedance loci, (1,1) mode, for the antenna element of Figure 3-1,  $\Lambda = 6.0$  (6.82).

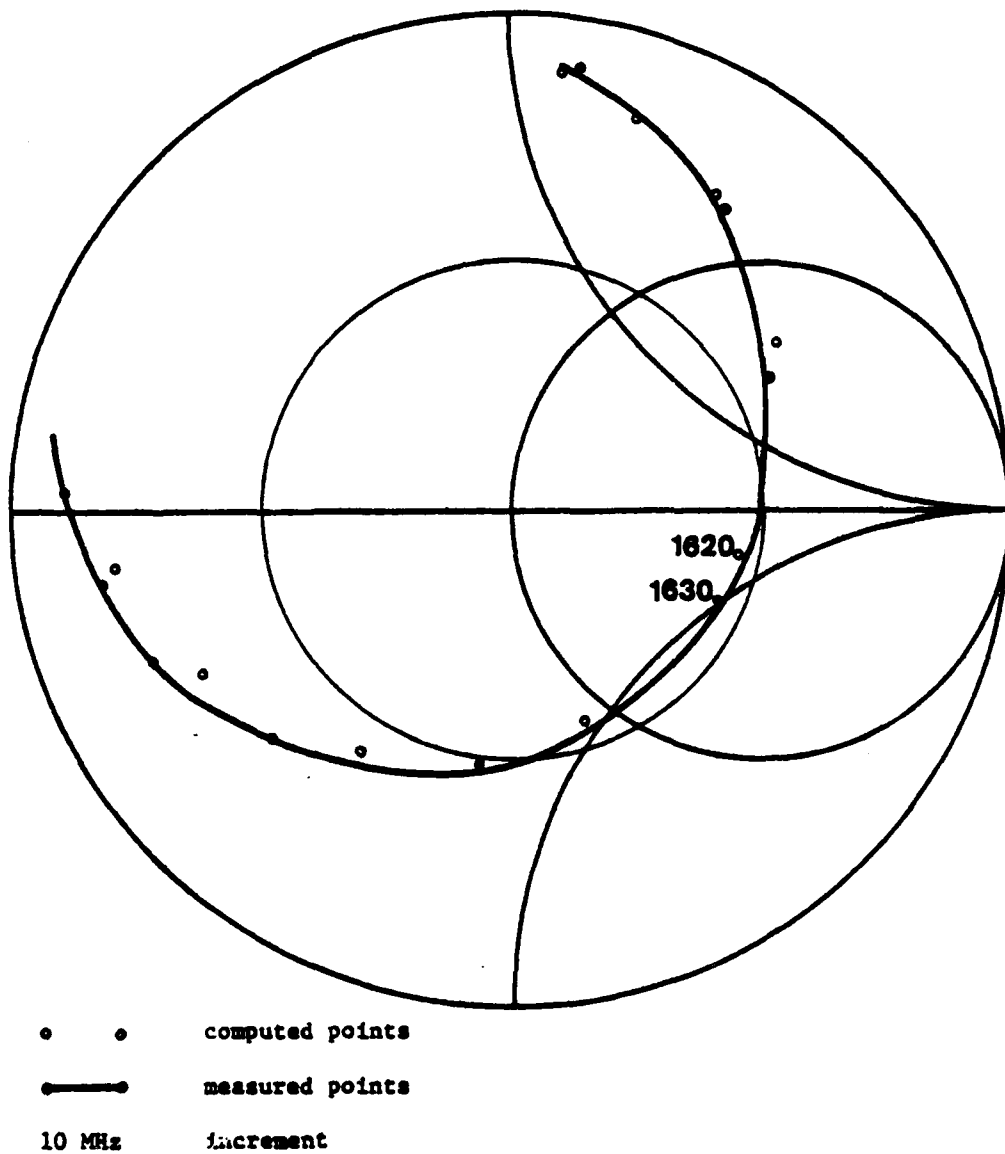


Figure 3-1-b: Calculated and measured input impedance loci, (1,2) mode, for the antenna element of Figure 3-1,  $\Lambda = 6.0$  (6.82).

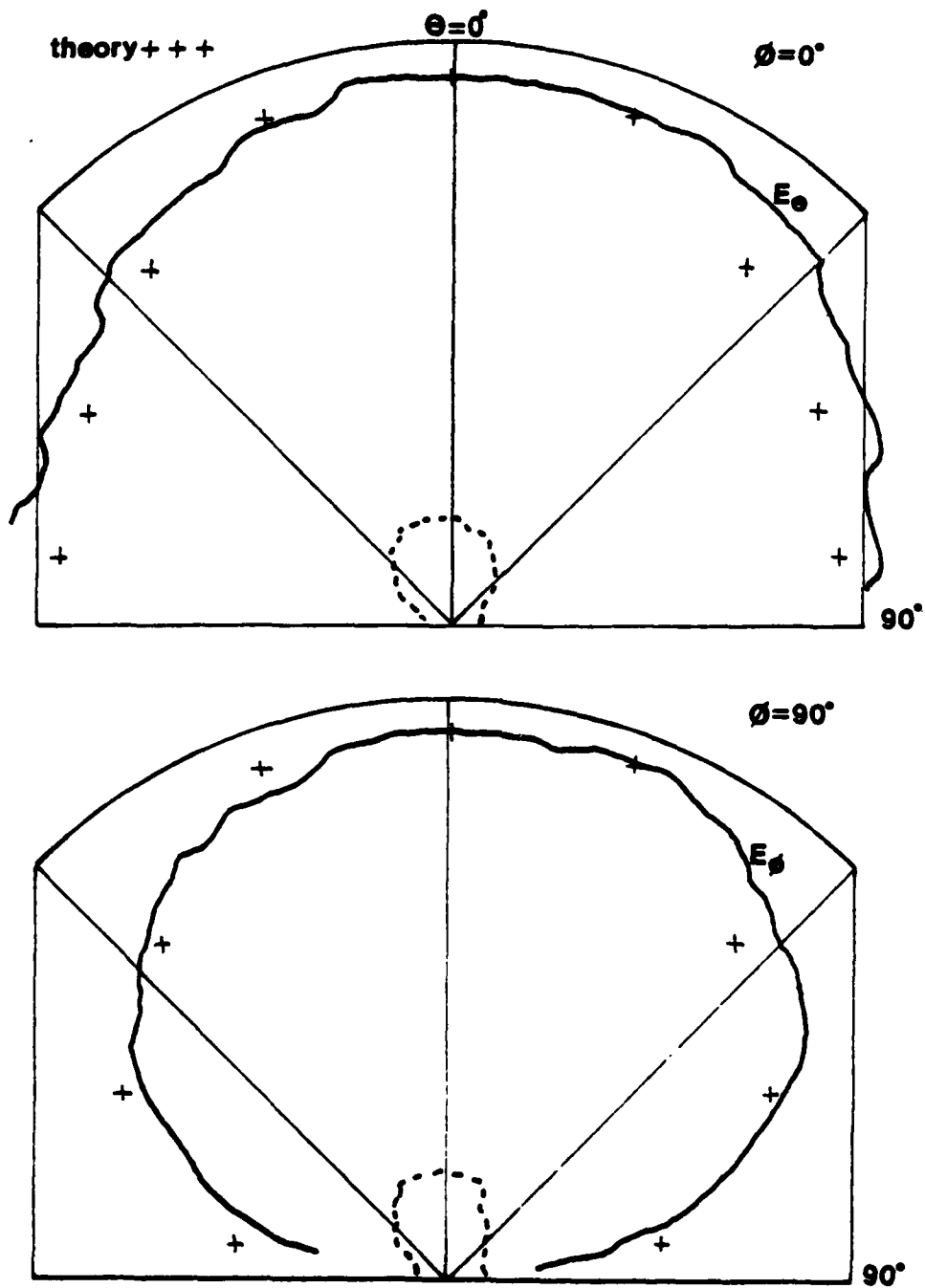


Figure 3-1-c: (1,1) mode radiation pattern in the  $\phi = 0^\circ$  and  $\phi = 90^\circ$  planes, of the microstrip antenna shown in Figure 3-1 at 537.4 MHz. (dotted pattern is for the cross-polarized component).

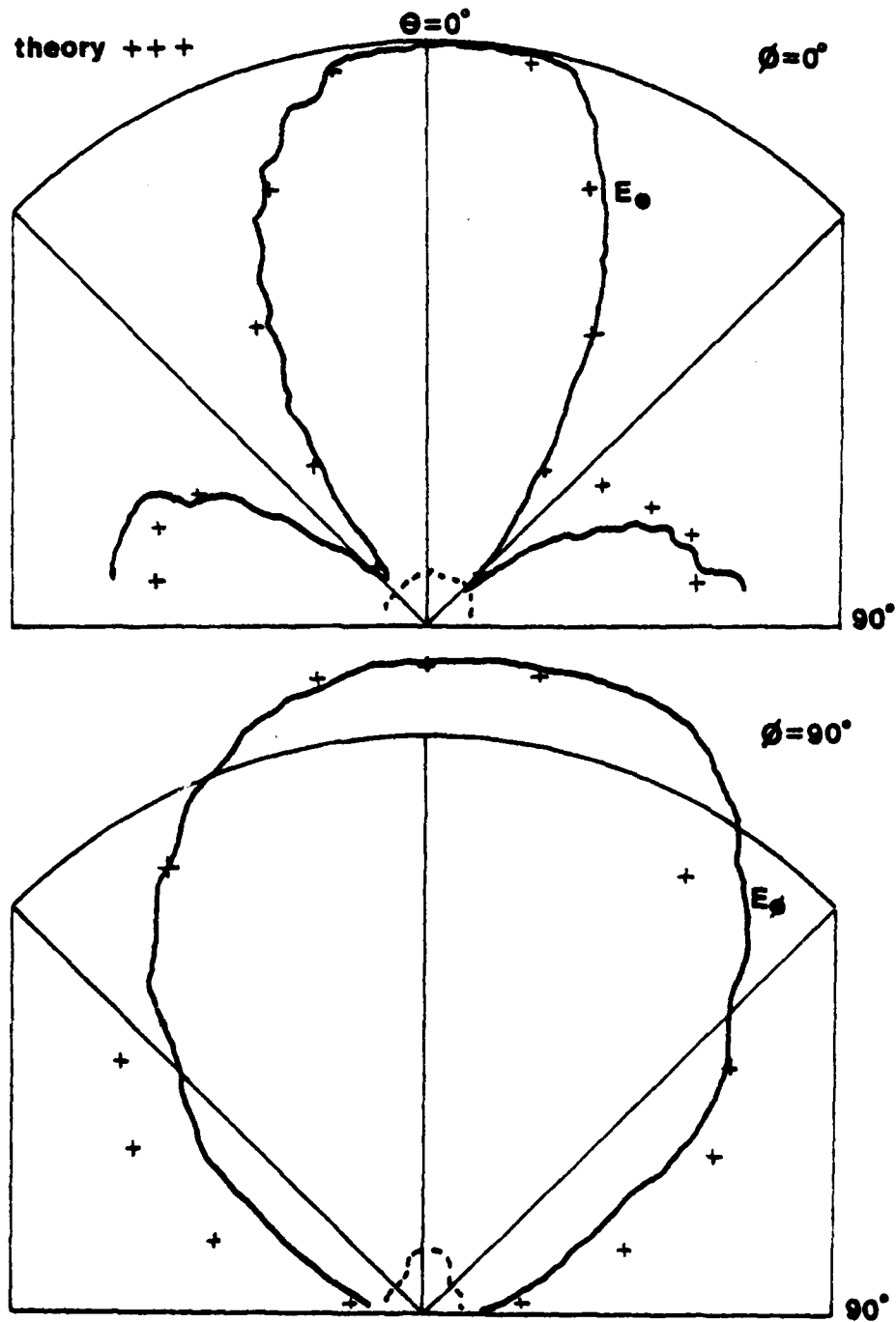


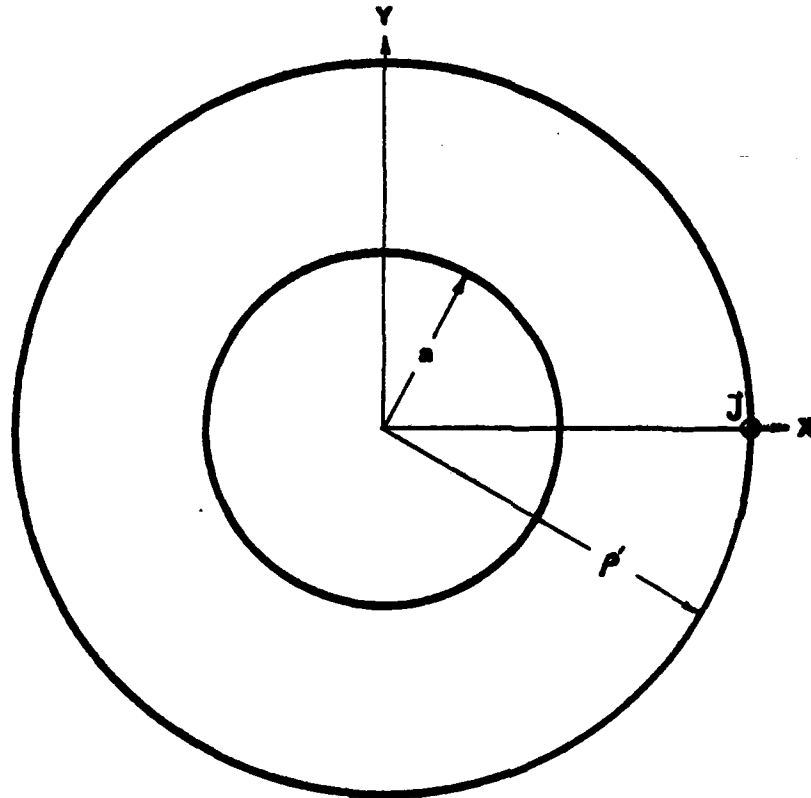
Figure 3-1-d: (1,2) mode radiation pattern in the  $\phi = 0^\circ$  and  $\phi = 90^\circ$  planes, of the microstrip antenna shown in Figure 3-1 at 1625 MHz (dotted pattern is for cross-polarized component).

The measured and calculated impedance loci of the (1,1) mode of the antenna in Figure 3-2,  $\Lambda = 2.0$  (2.16), is shown in Figure 3-2-a. Again, the agreement is very good, with a shift in frequency of only 10 MHz between theory and experiment.

The radiation pattern for this mode is shown in Figure 3-3. It can be seen, comparing these figures with 3-1-c and 3-1-d, which show the measured radiation of the antenna with  $\Lambda = 6.0$  (6.82), that the radiation pattern of the (1,1) mode of annular microstrip antennas does not depend on  $\Lambda$ , that is, the shape of the ring. Further, since the antenna of Figure 3-2 was fed at the outer edge, while the feed of the antenna in Figure 3-1 was located near the center of the ring, the radiation pattern seems to be also relatively independent of the feed position. This is important, since the driving point impedance, calculated from the magnitude of the field at the feed, can vary widely with feed position. We are therefore free to choose the feed position in order to obtain the desired impedance characteristics, without undue concern about any effect on the radiation pattern.

### 3-5 THE DUAL FREQUENCY ANTENNA

Other studies on the microstrip antenna [1], [4] have demonstrated the possibility of using shorting stubs placed about the antenna in order to modify the input impedance locus. The antenna can be modelled as a multi-port device (with the impedance of the shorted ports held equal to zero) and rigorously analyzed.



$\Lambda = 2.0$ (2.16)	
$a = 3.24$ (3.082) cm	Dielectric constant = 2.62
$p' = 6.48$ (6.657) cm	Skin depth = .00035 cm
Thickness = .158 cm	Loss tangent = .0008

Figure 3-2. The annular microstrip antenna  $\Lambda = 2.0$  (2.16)



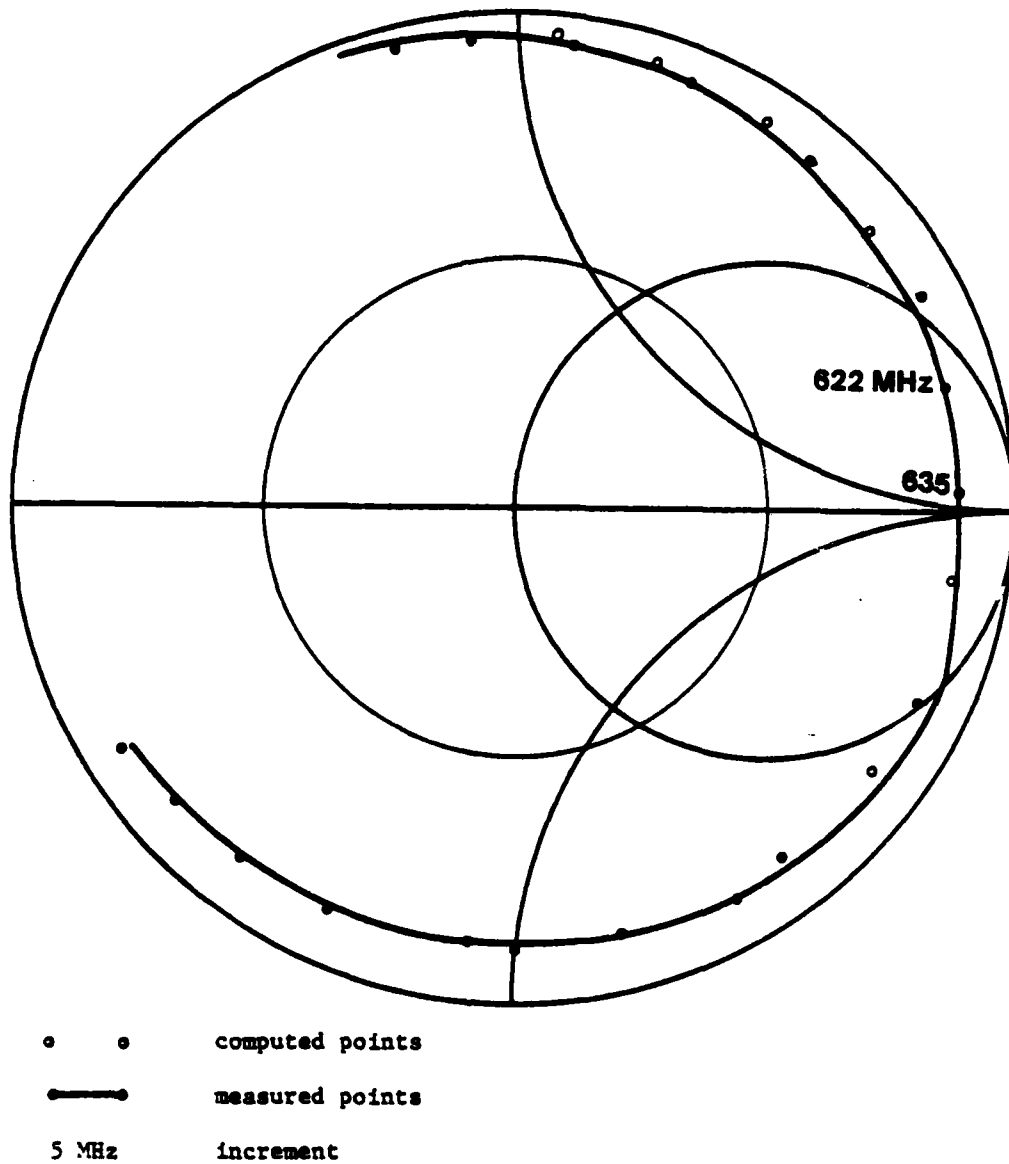


Figure 3-2-a: Calculated and measured impedance loci, (1,1) mode, for the antenna element of Figure 3-2,  $A = 2.0$  (2.16).

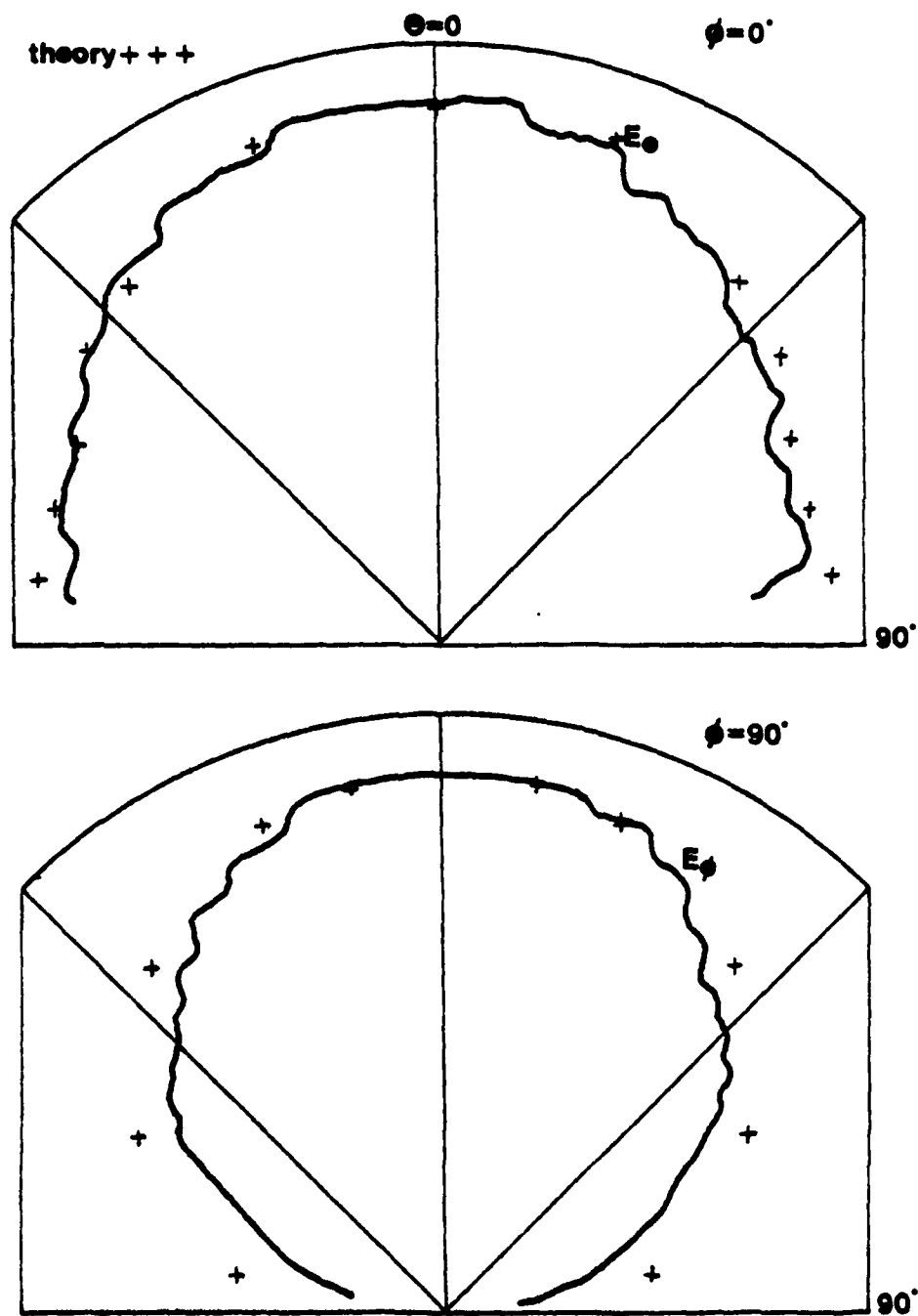


Figure 3-3: (1,1) mode radiation pattern in the  $\phi = 0^\circ$  and  $\phi = 90^\circ$  planes, of the microstrip antenna shown in Figure 3-2 at 635.7 MHz.

Figure 3-4 shows the magnitude variations of the (1,1), (1,2), and (1,3) modal functions of  $E_z$  as a function of  $\rho$  for an antenna with  $\Lambda = 6.82$ . At resonance, where one mode dominates, the electric field in the antenna is approximately a multiple of the appropriate modal function. The single or multiple zeroes of the higher order functions suggest that shorting pins can be placed at the null points of these resonant modes without effect, while they can substantially modify the impedance for any lower order mode.

Thus, in designing a dual frequency antenna, the radial location of the feed is first chosen to obtain the desired impedance of the higher order mode. A shorting pin is then placed somewhere in the circle of the higher order null. By choosing  $\phi_p$ , the angle between the feed and the shorting pin, the impedance for the lower order resonance can thus be tuned as desired. In practice, only the (1,1) and (1,2) resonances exhibit useful and similar patterns, so attention was focused on these modes.

Figure 3-6 shows the measured impedance of the (1,2) resonance of the antenna of Figure 3-5,  $\Lambda = 6.0$  (6.82), with  $\rho' = 4.9$  cm. The variation of the (1,1) mode impedance with  $\phi_p$  is shown in Figure 3-7. It is clear that by moving the position of the shorting pin, the input impedance can be varied over a wide range.

Unfortunately, the shorting pin changes not only the impedance locus of the lower resonance, but also the radiation pattern, by introducing a large cross-polarization component. Figure 3-8, the radiation pattern of the (1,1) mode with the shorting pin in place,

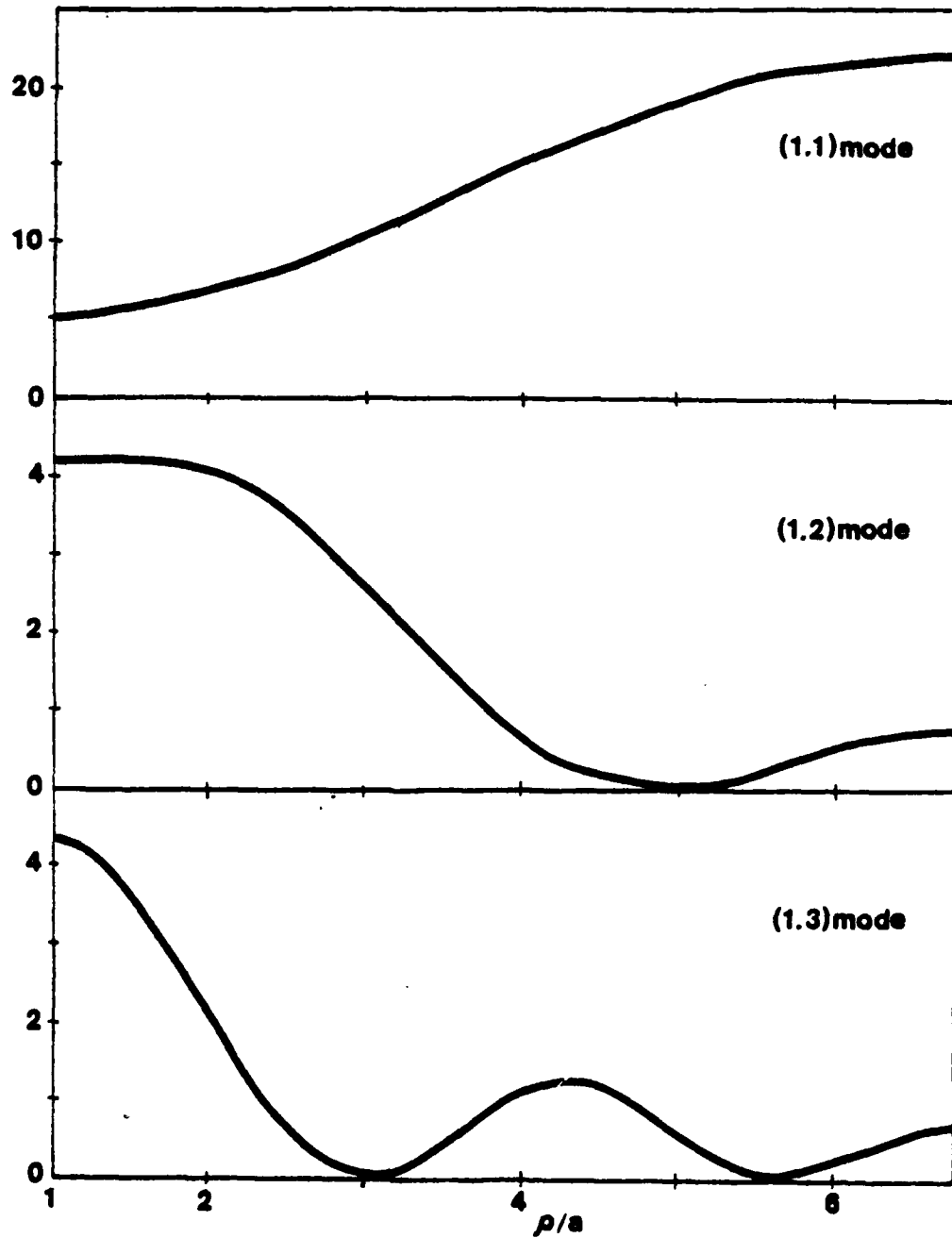
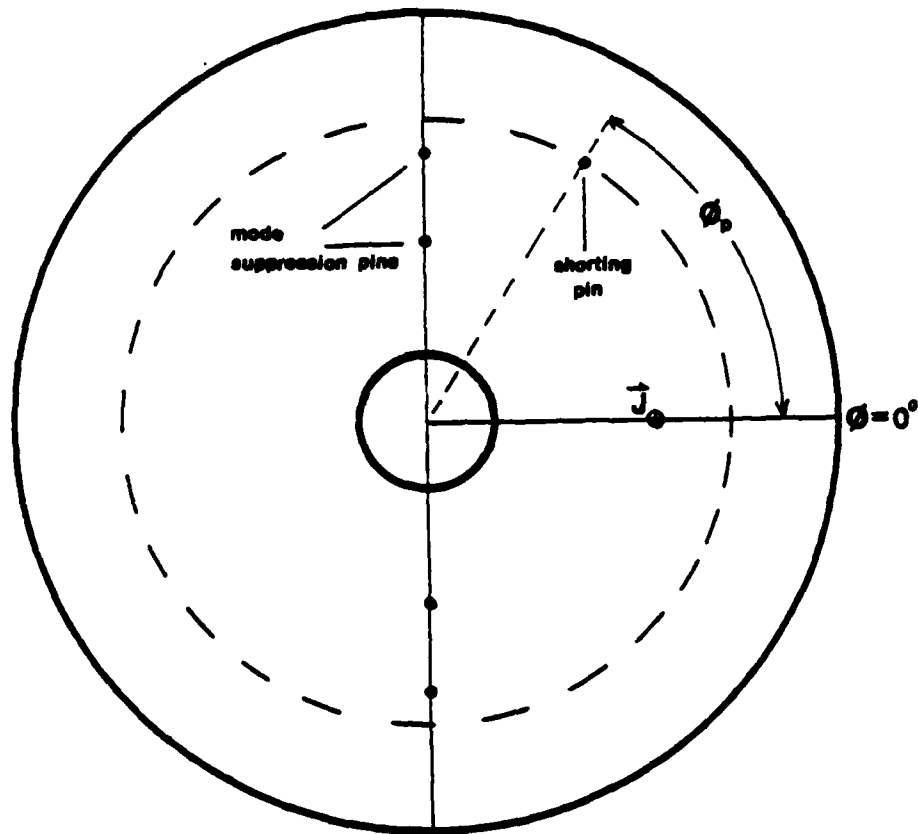


Figure 3-4: The (1,1), (1,2) and (1,3) modal functions  $[J_1'(Ka) N_1(K\rho) - N_1'(Ka) J_1(K\rho)]$  as a function of  $\rho$ ,  $\Lambda = 6.82$ ,  $a = 1.342$  cm.



$$a = 1.5 \text{ (1.342) cm}$$

$$\Lambda = 6.0 \text{ (6.82)}$$

$$\rho' = 4.9 \text{ cm}$$

shorting pin at  $\rho = 6.5 \text{ cm}$

mode suppression pins at  $\rho = 4.0, 6.0 \text{ cm}, \phi = 90^\circ, 180^\circ$

Figure 3-5: The dual frequency antenna,  $\Lambda = 6.0 \text{ (6.82)}$

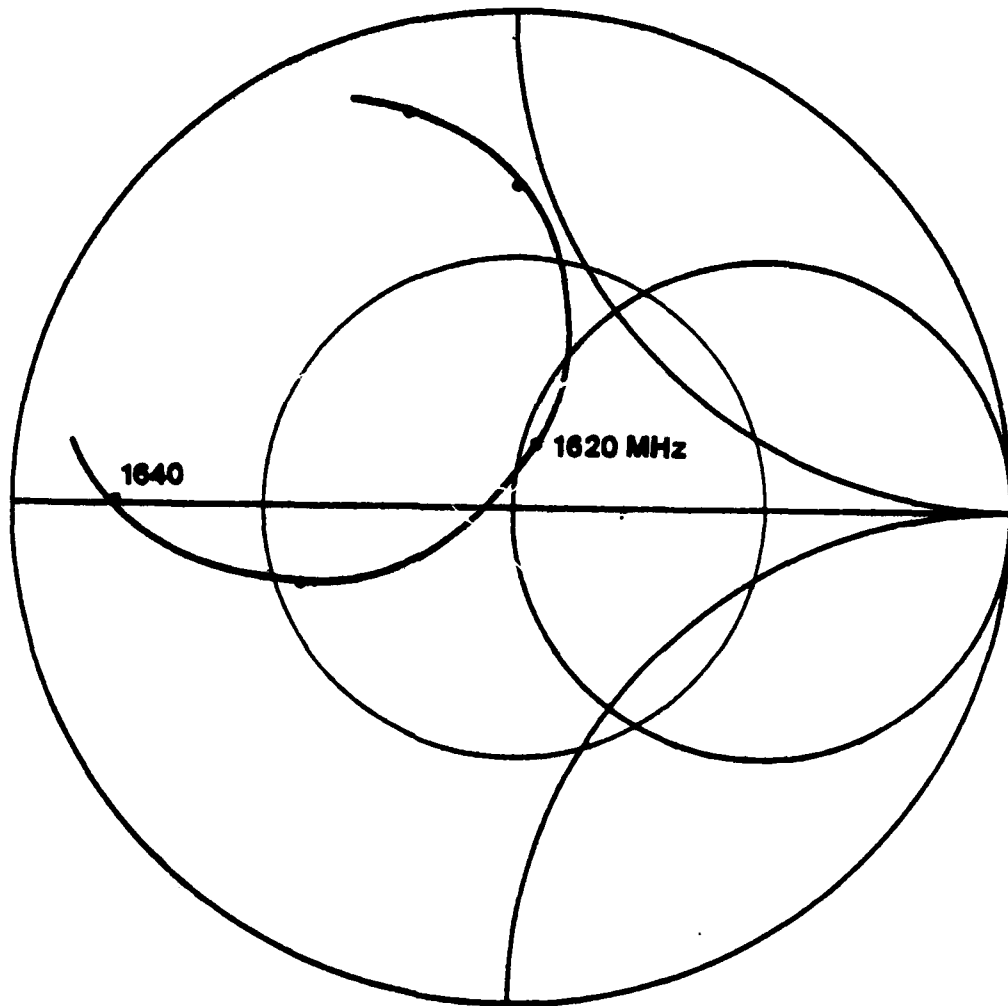


Figure 3-6: Measured impedance locus, (1,2) mode, for the antenna element of Figure 3-5,  $\Lambda = 6.0$  (6.82); frequency increment = 10 MHz.

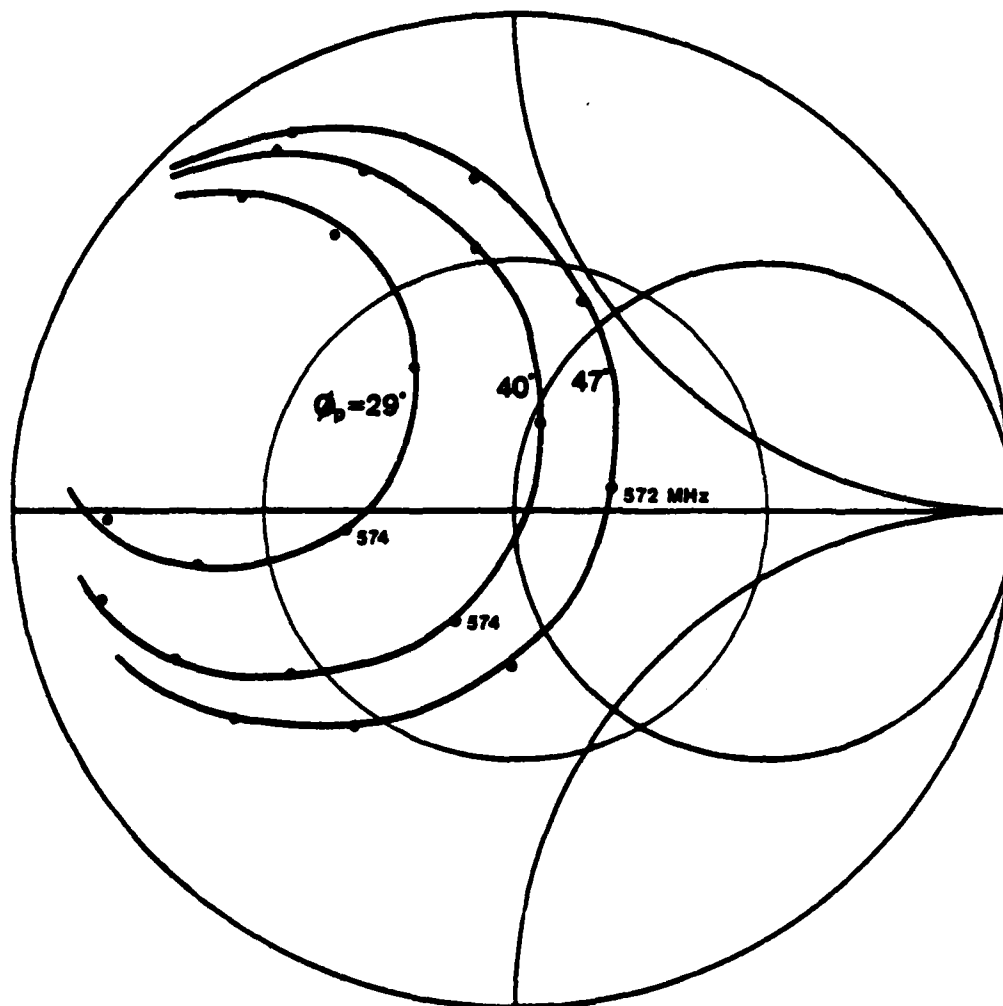


Figure 3-7: Measured impedance loci, (1,1) mode, for the antenna element of Figure 3-5,  $\Lambda = 6.0$  (6.82), for  $\phi_p = 29^\circ$ ,  $40^\circ$ , and  $47^\circ$ ; frequency increment = 2 MHz.

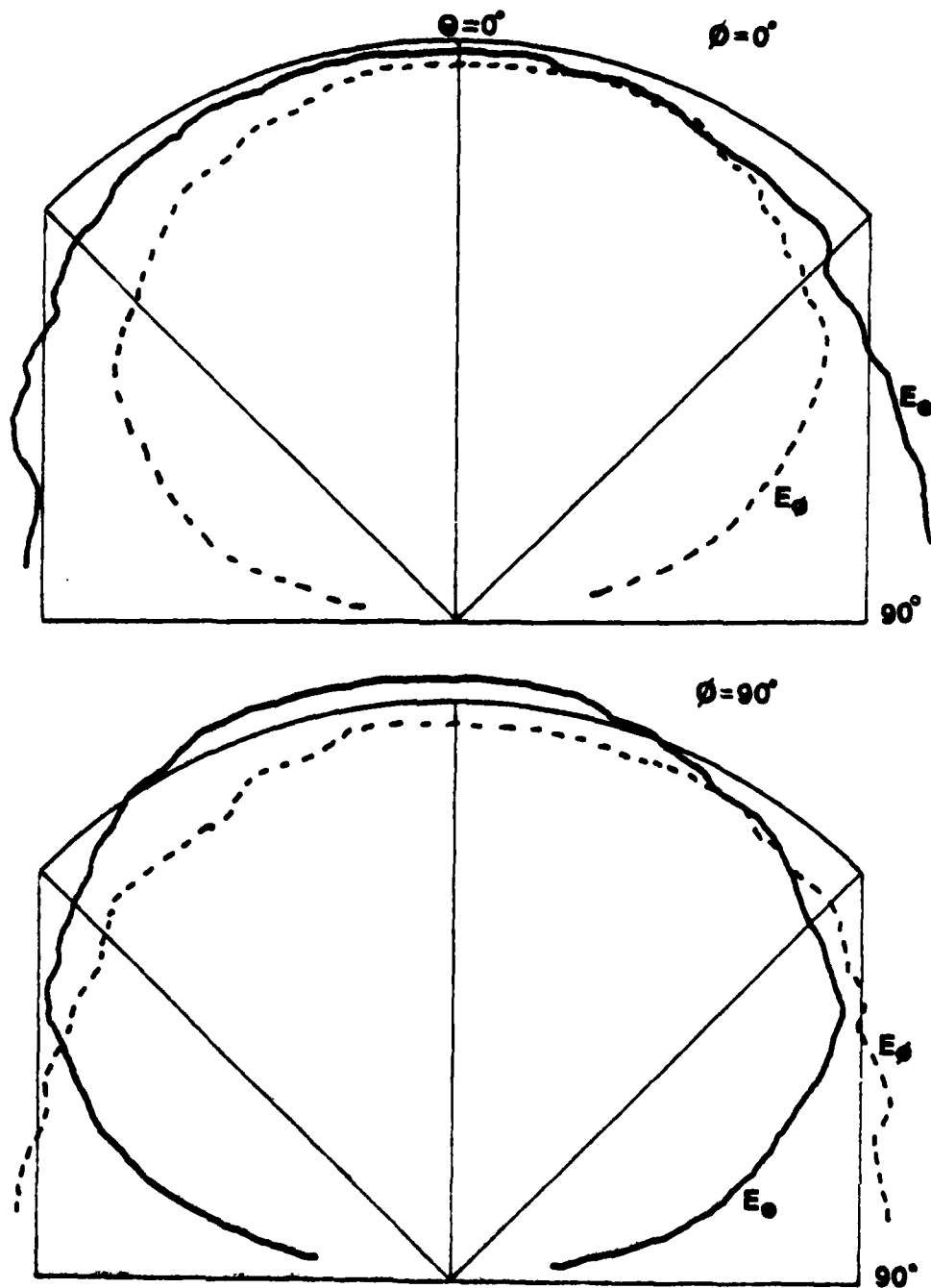


Figure 3-8: (1,1) mode radiation pattern in the  $\phi = 0^\circ$  and  $\phi = 90^\circ$  planes, of the microstrip antenna of Figure 3-5, at 573.4 MHz.  $\phi_p = 40^\circ$ , without mode suppression pins.



can be compared with Figure 3-1-c, where no shorting pin is present. However, this cross-polarization can be removed by placing shorting mode suppression pins at  $90^\circ$  and  $180^\circ$  relative to the feed point. The fields which give rise to the cross-polarization vary as  $\sin\phi$  and are thus effectively damped. Figure 3-9 shows the same (1,1) resonance with four such pins in place, and the cross-polarization substantially reduced. Since the original short was located so as to not affect the (1,2) resonance, the radiation pattern at this resonance (Figure 3-10) shows essentially no change from Figure 3-1-d.

It is obvious that by varying  $\Lambda$ , the ratio between the (1,1) and (1,2) resonances can be changed. The tuning process outlined above was repeated for an antenna with  $\Lambda = 2.72$  (2.95), shown in Figure 3-11.

In Figure 3-12 the impedance of the (1,2) resonance is displayed, and Figure 3-13 shows the effect of  $\phi_p$  on the lower order (1,1) resonance. Figure 3-13 also demonstrates the possibility of shifting the resonant frequency through the use of shorting pins. As the pin placement is changed,  $\phi_p = 140^\circ$  to  $170^\circ$ , the resonant frequency also changes, from 680 to 748 MHz. Thus the ratio between the (1,1) and (1,2) resonances can be varied from 3.18 to 2.90. Continuing studies on the use of multiple shorting pins to change resonant frequencies indicate that such a technique can be used to shift resonances over a wide range, and that construction of antennas operating at two frequencies of relatively arbitrary ratio can be accomplished. It must be noted, however, that the presence of multiple shorting pins

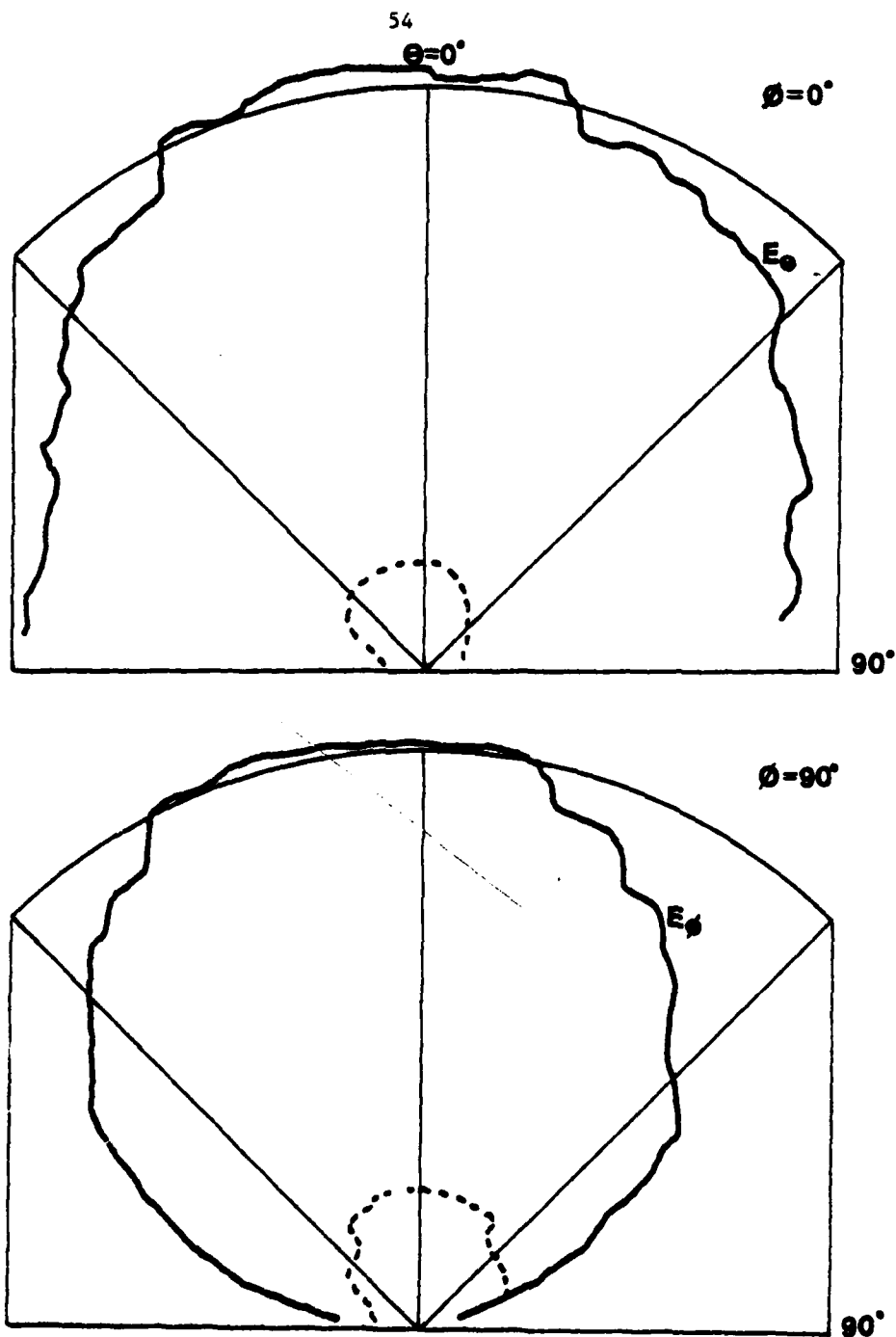


Figure 3-9: Same as Fig. 3-8, but with mode suppression pins at  $\rho = 4.0, 7.0$  cm,  $\phi = 90^\circ, 180^\circ$  (dotted pattern is for cross-polarization component)

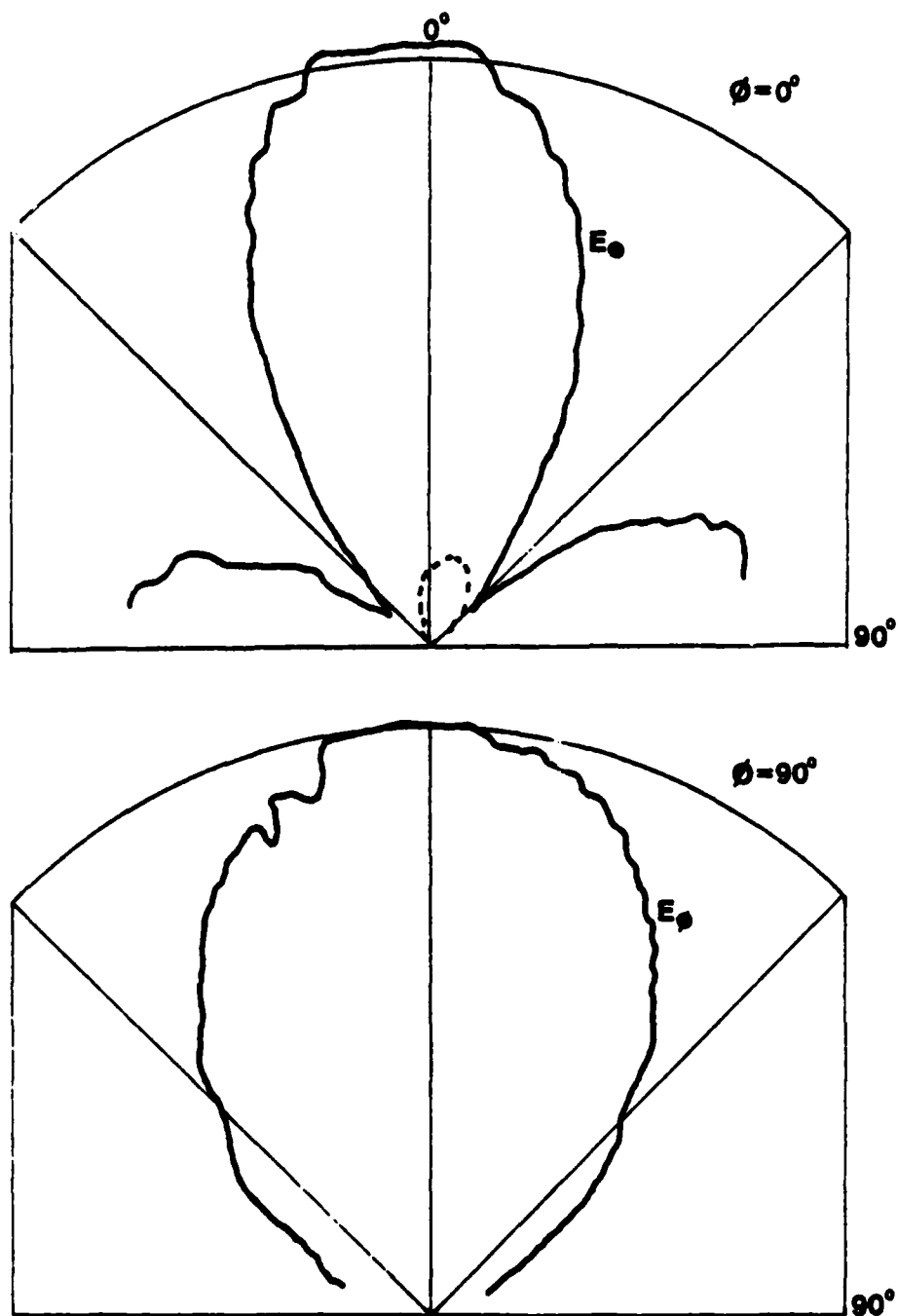
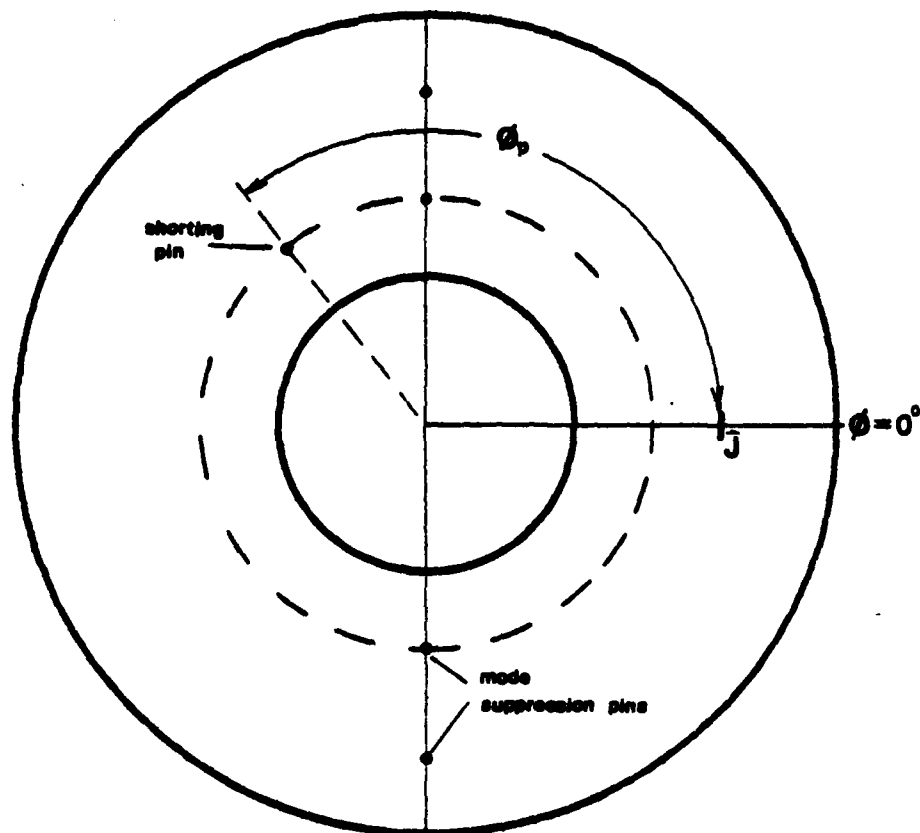


Figure 3-10: (1,2) mode radiation pattern in the  $\phi = 0^\circ$  and  $\phi = 90^\circ$  planes, of the microstrip antenna shown in Figure 3-4,  $\phi_p = 40^\circ$ .



$$a = 2.7 \text{ (2.542) cm}$$

$$\Lambda = 2.72 \text{ (2.95)}$$

$$\rho' = 5.0 \text{ cm}$$

shorting pin at  $\rho = 4.1 \text{ cm}$

mode suppression pins at  $\rho = 4.0, 6.0 \text{ cm}, \phi = 90^\circ, 180^\circ$

Figure 3-11: The dual frequency antenna  $\Lambda = 2.72 \text{ (2.95)}$ .

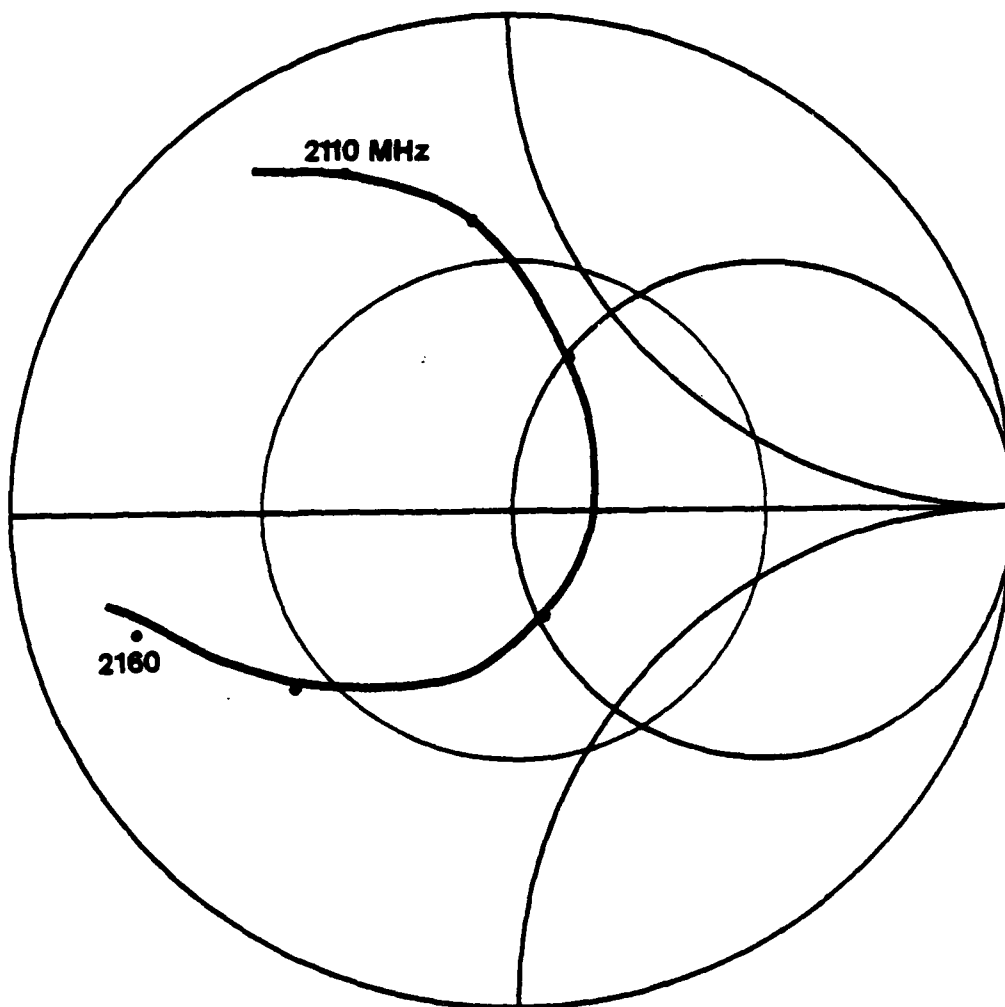


Figure 3-12: Measured impedance locus, (1,2) mode, for the antenna element of Figure 3-11,  $\Lambda = 2.72$  (2.95); frequency increment = 10 MHz.

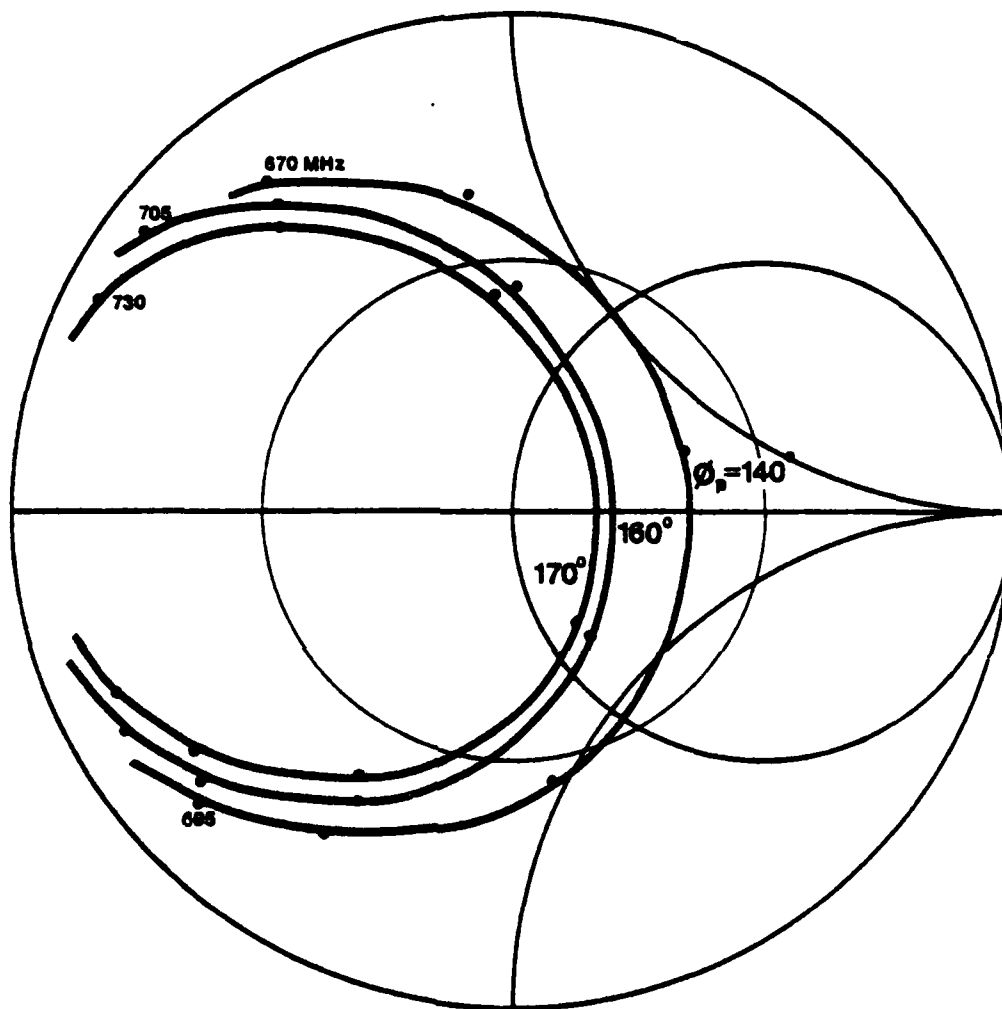


Figure 3-13: Measured impedance loci, (1,1) mode, for the antenna element of Figure 3-11,  $\Lambda = 2.72$  (2.95), for  $\phi_p = 140^\circ$ ,  $160^\circ$ ,  $170^\circ$ ; frequency increment = 5 MHz.

also changes the radiation pattern. The possible shift in frequency, then, may be ultimately determined by how much distortion in the radiation pattern can be tolerated.

Figures 3-14 and 3-15 give the radiation pattern of the (1,1) resonance, with and without mode suppressing pins. Here the cross-polarization is only slightly reduced. Figures 3-16 and 3-17 similarly show the patterns of the (1,2) resonance. In this case, the shorting pin was not placed exactly at the null of the (1,2) mode, so that the effect of the mode suppression pins is seen for both resonances.

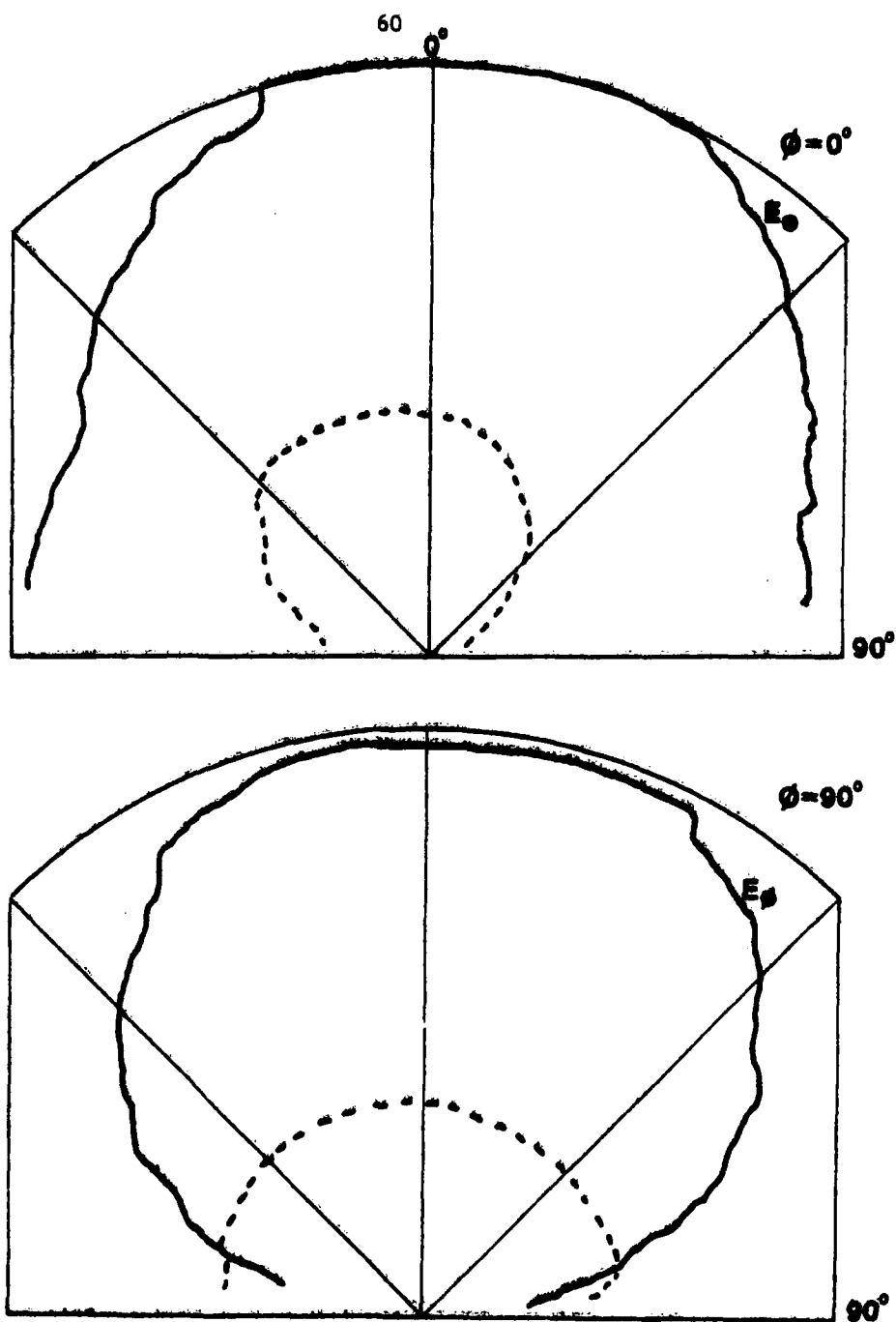


Figure 3-14: (1,1) mode radiation pattern in the  $\phi = 0^\circ$  and  $\phi = 90^\circ$  planes, of the antenna shown in Figure 3-11, at 728.8 MHz,  $\phi_p = 160^\circ$ , without mode suppression pins.



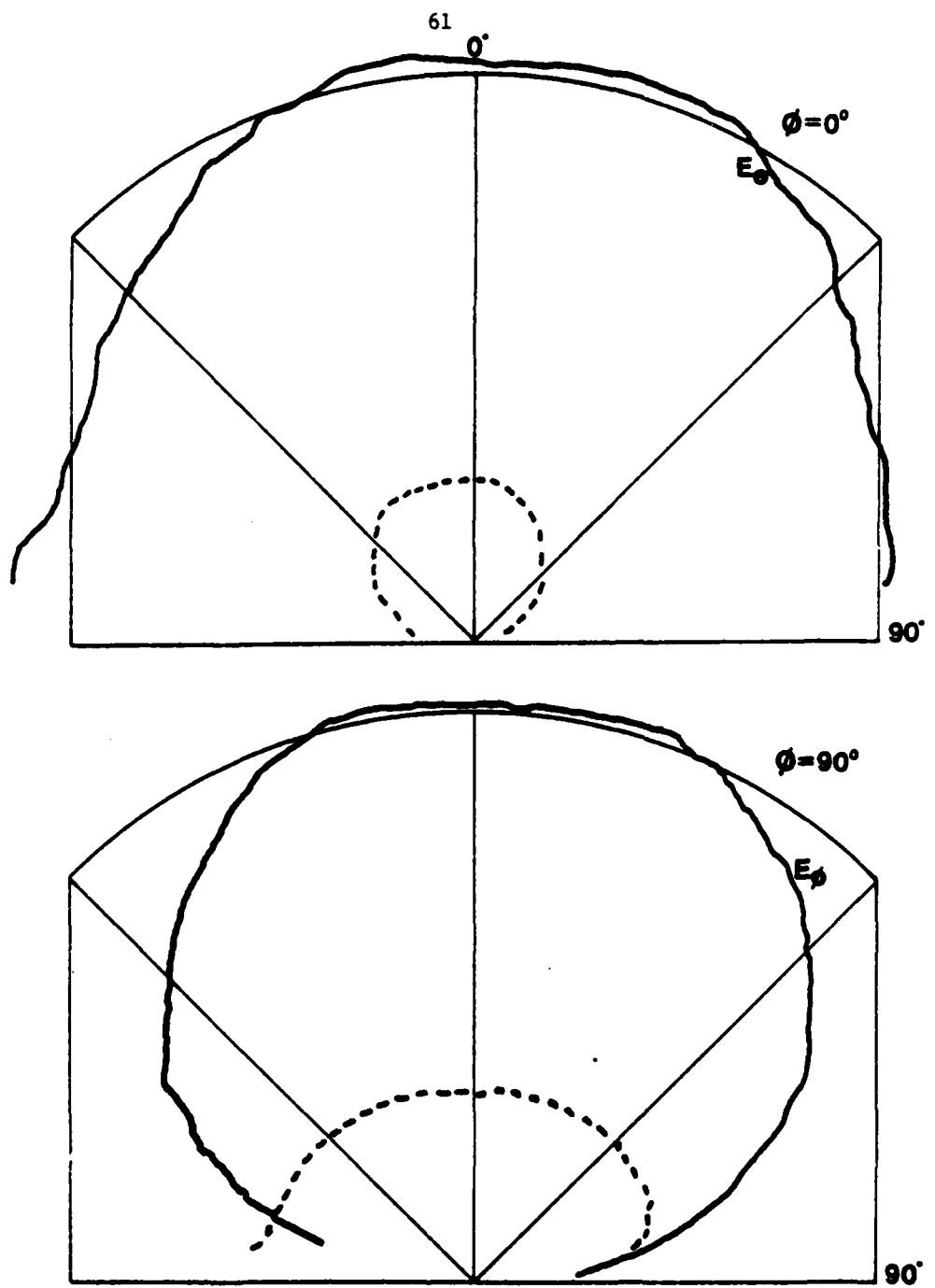


Figure 3-15: Same as Figure 3-14, but with mode suppression pins at  $\rho = 4.0, 6.0$  cm;  $\phi = 90^\circ, 180^\circ$  (dotted pattern is for cross-polarized component).

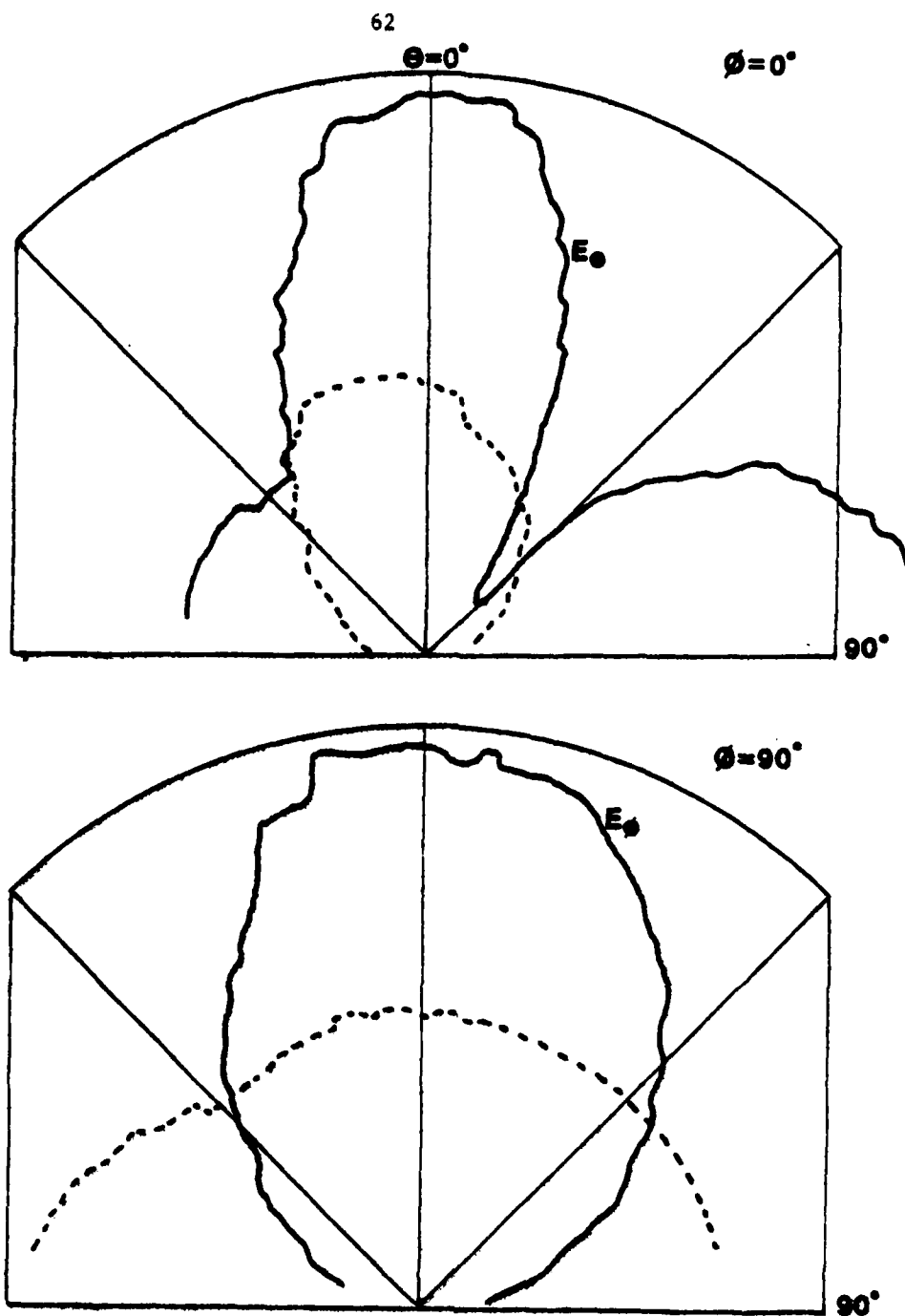


Figure 3-16: (1,2) mode radiation pattern in the  $\phi = 0^\circ$  and  $\phi = 90^\circ$  planes, of the antenna shown in Figure 3-11, at 2170 MHz,  $\phi_p = 160^\circ$ , without mode suppression pins.

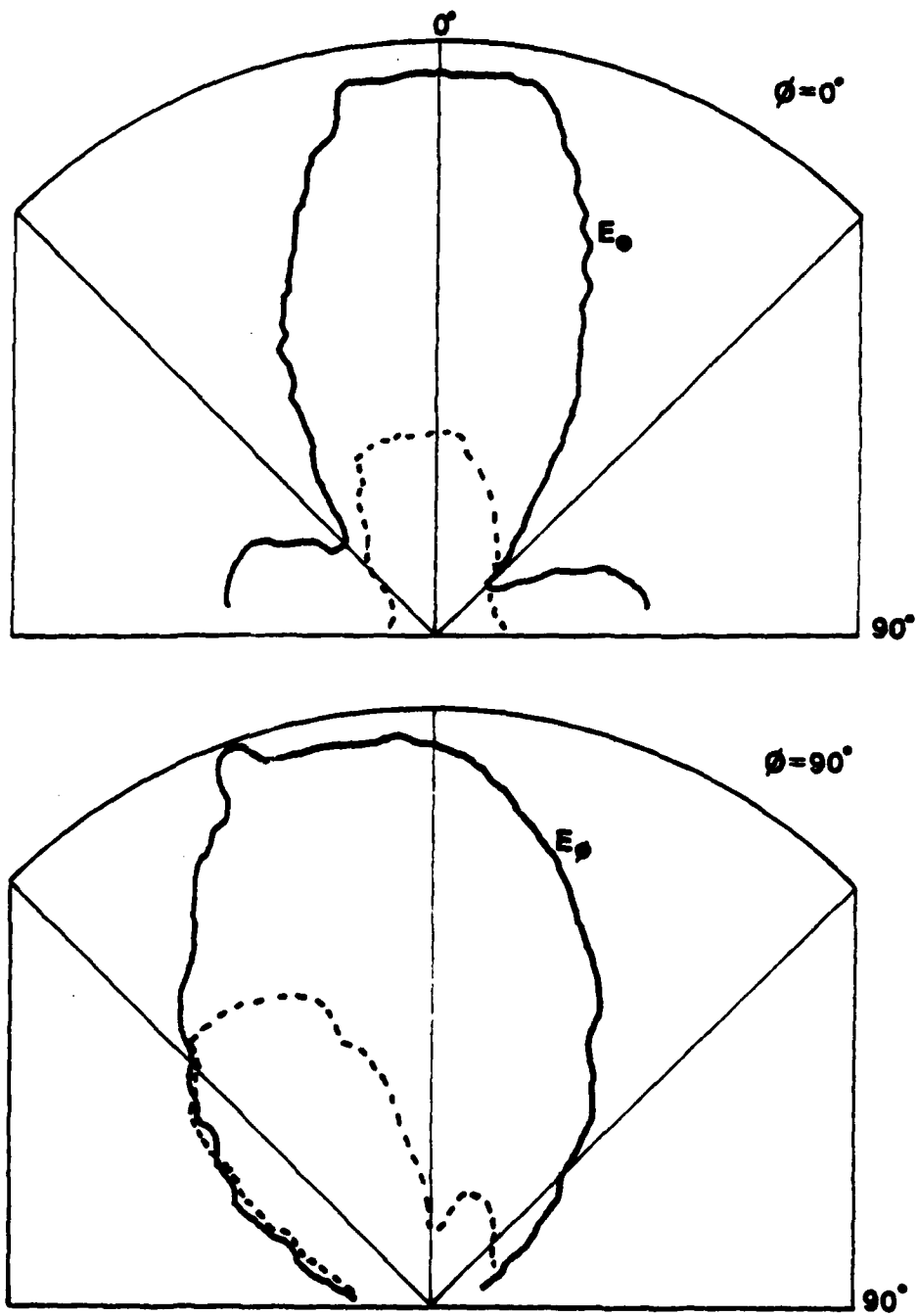


Figure 3-17: Same as Figure 3-16, but with mode suppression pins at  $\rho = 4.0, 6.0$  cm;  $\phi = 90^\circ, 180^\circ$  (dotted pattern is for cross-polarized component).

## CHAPTER 4

## FRINGING FIELDS AND THE EDGE CORRECTION

The analysis of the microstrip antenna developed in Chapter 2 is based on the model of a closed cavity. As such, the E field is along the z direction only and exists only in the cavity. These approximations, which allow the difficult problem of the antenna fields to be solved in separable form, do not take into account the complicated fringing fields at the edges of the antenna.

The effect of the fringing fields is most clearly seen by comparing calculated resonance frequencies of microstrip antennas with experiment. Other writers [4],[8] have noted that the resonance frequencies of a circular disc microstrip antenna, calculated on the basis of a closed cavity model, are consistently too high. This is also true for antennas of other geometries, rectangular, for example, which have no interior boundaries.

Several methods can be used to better approximate the fields inside the antenna. Other boundary conditions, rather than the assumption of a PMC wall used in this paper, can be defined at the edges of the antenna. Perhaps more simply, the dimensions of the cavity can be slightly changed; since the fields extend outward beyond the edges, the antenna is assumed, for purposes of calculation, to be slightly larger than its actual physical dimensions.

In applying this second method, then, the question arises of how to determine the necessary change in dimension. Analytic calculations of

this quantity have been made, based, for example, on the dc capacitance of the antenna [8]. In this paper, a simpler, empirical correction has been used. By comparing experimental and analytical results, it was found that a change in dimension approximately that of the thickness of the antenna gives the best overall agreement between theory and experiment. Since the fringing field is assumed to extend outward from the antenna patch, in order to obtain the modified dimensions of the antenna this length is added to the outer radius and subtracted from the inner radius.

It should be noted that this value for the correction has been determined only by considering thin microstrip antennas. The analysis of fringing effects for thick antennas can be expected to be more complicated, and it is likely that this correction may also depend on the permittivity of the antenna dielectric, the curvature of the antenna boundaries, as well as other factors.

Tables 4-1 and 4-2 compare some resonant frequencies of two antennas,  $\Lambda = 6.0$  (6.82) and  $\Lambda = 2.0$  (2.16), calculated both with and without the edge correction, to the experimentally measured frequencies. The modified resonant frequencies show a generally closer agreement with experiment, (deviation of approximately 1%.) particularly at higher order resonances, where the uncorrected theory predicts values that are consistently too high.

It is interesting to note that while the calculated resonance frequencies of disc and rectangular microstrip antennas are consistently higher than the measured values, the resonances of the annular antenna

Table 4-1: Theoretical resonance frequencies, calculated with and without edge correction, and measured values, for the annular antenna of Figure 3-1,  $A = 6.0$  (6.82). Edge correction = .158 cm.

Mode	Uncorrected		Edge Corrected		Experimental Res. Frequency (MHz)
	(K <sub>na</sub> )	Frequency (MHz)	(K <sub>na</sub> )	Frequency (MHz)	
(1,1)	0.29042	571.34	0.259	570	573.4
(2,1)	0.50743	998.0	0.4450	978	989.8
(1,2)	0.83062	1634.0	0.737	1620	1625.0
(2,2)	1.09728	2158.7	0.972	2137	2137.7
(1,3)	1.37743	2709	1.200	2638	2625.0

Table 4-2: Theoretical resonance frequencies, calculated with and without edge correction, and measured values, for the annular antenna of Figure 3-2,  $\lambda = 2.0$  (2.16). Edge correction = 1.58 cm.

Mode	Uncorrected		Edge Corrected		Experimental Res Frequency (MHz)
	(K <sub>na</sub> )	Frequency (MHz)	(K <sub>na</sub> )	Frequency (MHz)	
(1,1)	0.67734	616.6	0.648	622	635.0
(2,1)	1.34060	1220.5	1.273	1220	1250.8
(3,1)	1.97888	1801.6	1.910	1829	1829.6
(4,1)	2.58761	2355.8	2.44	2340	2370.5
(5,1)	3.1613	2878.1	2.946	2820	2854.0
(1,2)	3.28247	2988.4	2.91	2786	2810.3
(2,2)	3.53129	3214.9	3.14	3006	3075.0
(3,2)	3.92005	3568.9	3.57	3418	3417.4
(4,2)	4.4318	4034.8	4.07	3897	3890.0

follow a more complicated pattern. At low order resonances, the uncorrected theory predicts values that are too low. As the excitation frequency increases, the difference between theory and experiment gradually narrows, and finally, at high frequencies the theoretical resonance frequencies are higher than those measured. This can be more clearly seen in the data for the antenna with  $\Lambda = 2.0$  (2.16). This phenomenon is qualitatively examined in Appendix B.

The edge correction also affects the calculated impedance, in general, by simply rotating the impedance locus. In Figure 4-1, the calculated impedance locus is shown for the (1,1) mode of the antenna of Figure 3-1,  $\Lambda = 6.0$  (6.82). As the outer radius,  $b$ , is increased, the impedance locus shifts, lowering the calculated resonant frequency, the frequency at which the impedance is purely real. This is expected, since increasing  $b$  also increases  $\Lambda$ . Figure 2.2 shows that the resonant frequency decreases monotonically with  $\Lambda$ .

When the inner radius  $a$  is varied, the situation is more complicated, since the roots of the characteristic equation (2.23) depend on  $a$  and  $\Lambda$ , which are both changing. From the analysis of Appendix B, it is clear that at low frequencies a decrease in  $a$  shifts the resonance higher, while for high order modes the shift is to lower resonant frequencies.

Figure 4-2 shows the shift in impedance as  $a$  is varied for the same (1,1) mode as in Figure 4-1. At this low order mode the calculated resonant frequency increases as  $a$  is decreased. In Figure 4-3 the impedance of a higher order (4,2) is displayed, with the shift now towards a lower resonant frequency as  $a$  is decreased.



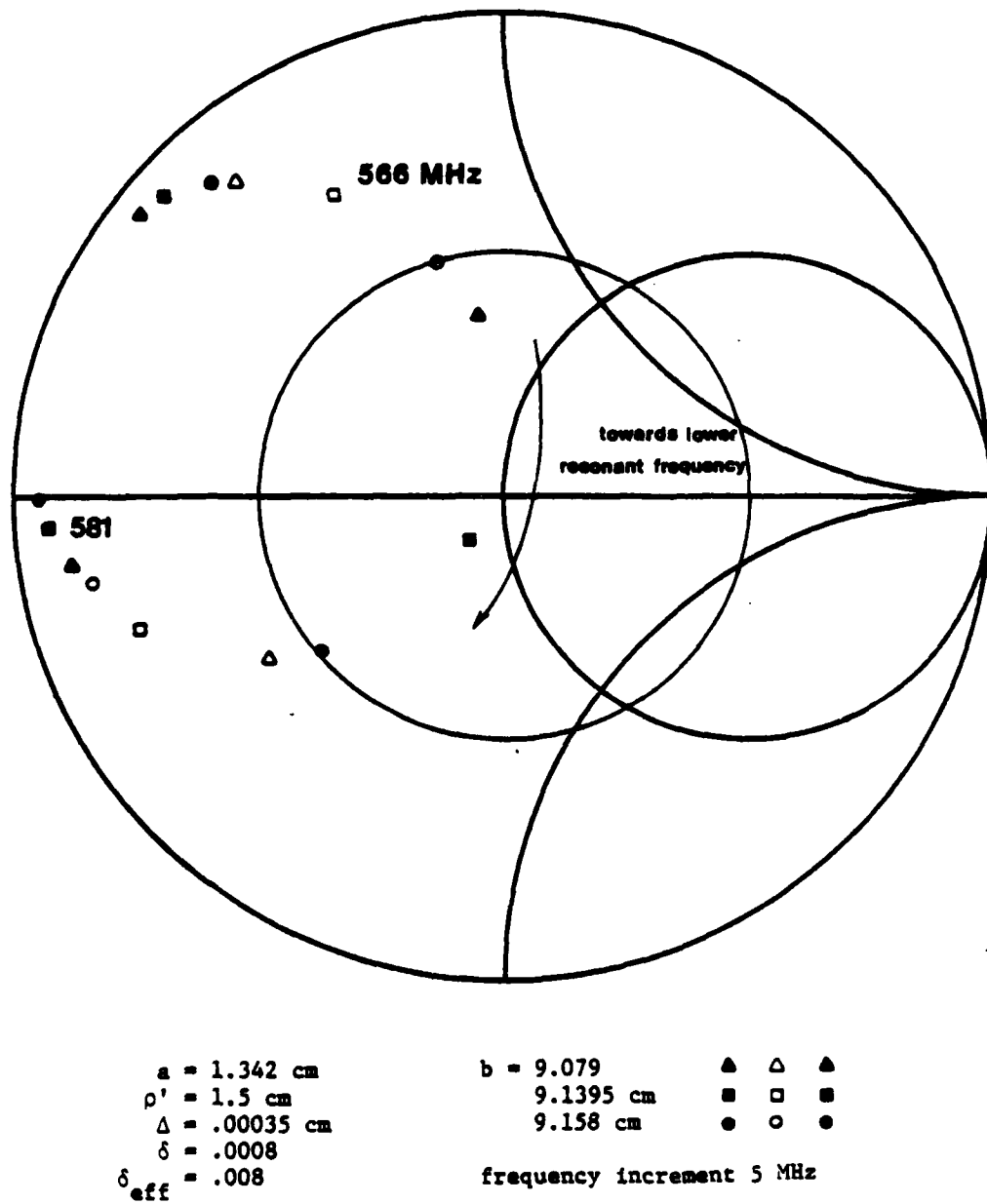
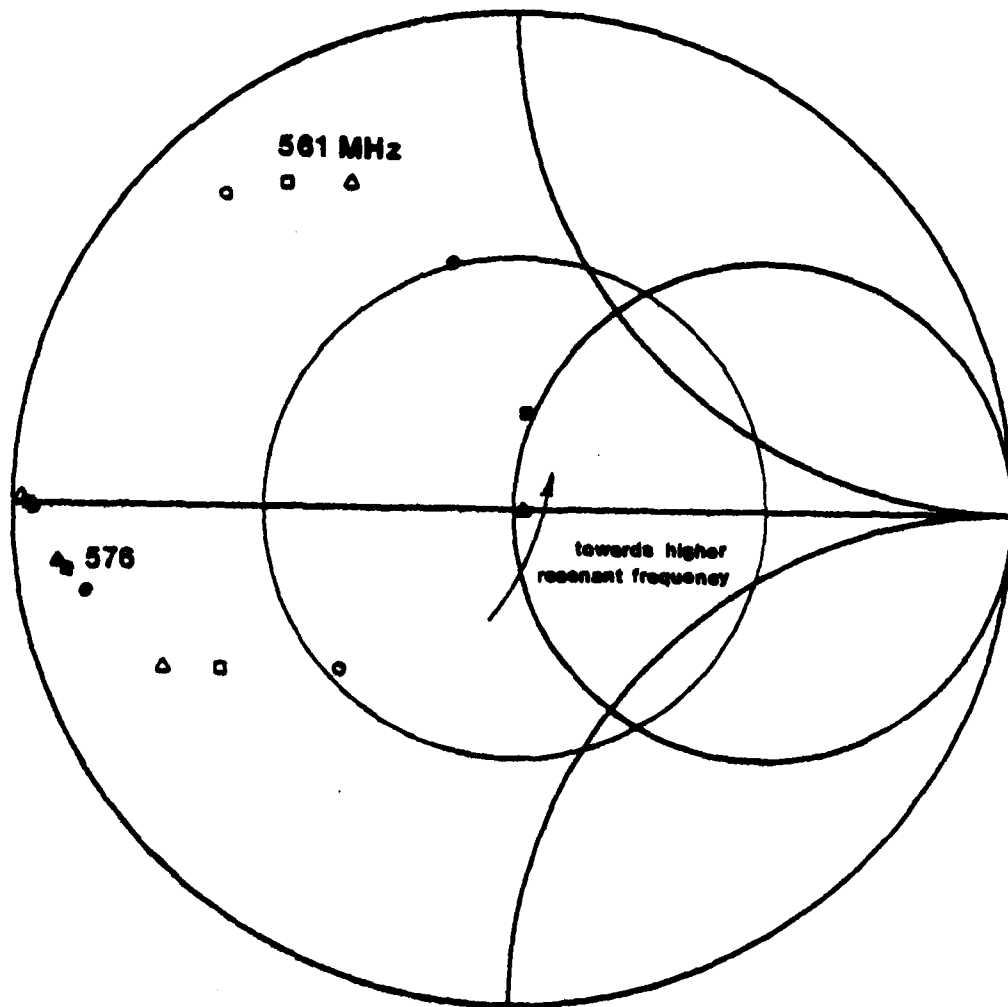


Figure 4-1: The shift of the calculated impedance locus, (1,1) mode, as the outer radius  $b$  is increased,  $\Lambda = 6.0$ .

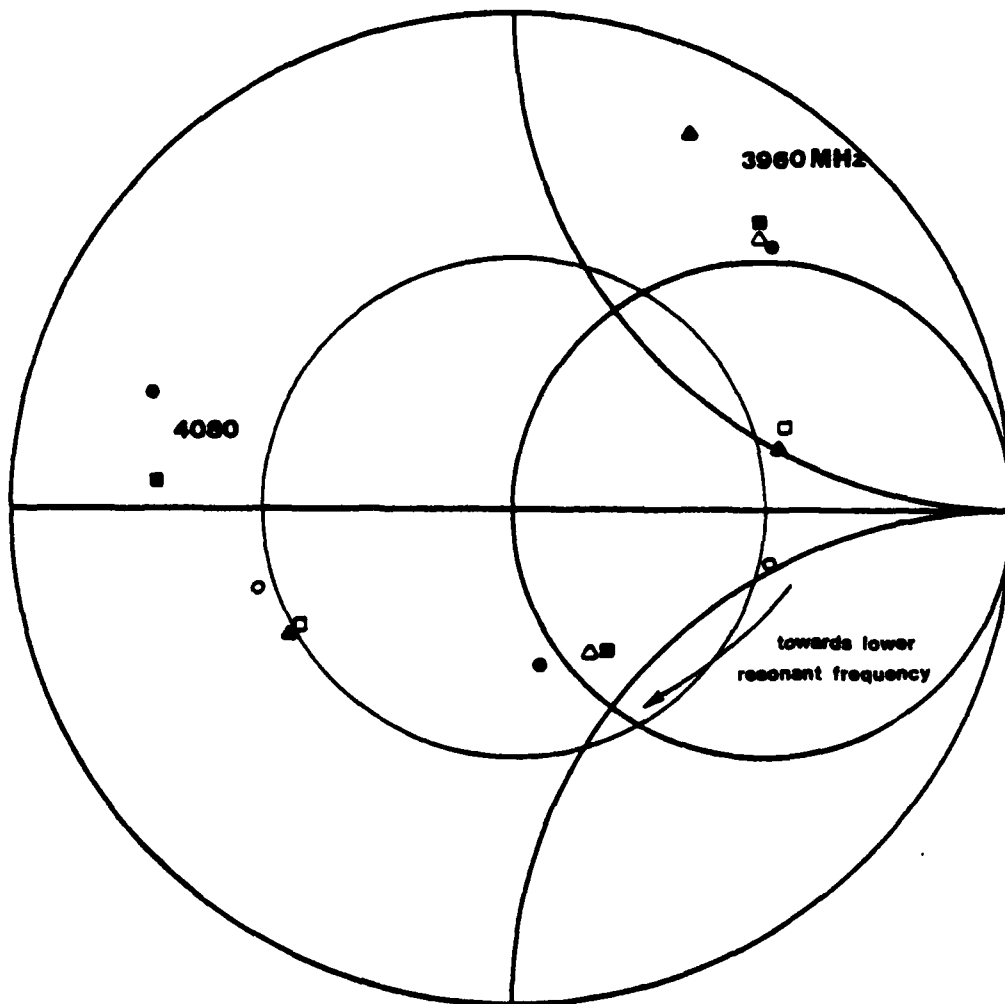


$b = 9.158 \text{ cm}$   
 $\rho' = 1.5 \text{ cm}$   
 $\Delta = .00035 \text{ cm}$   
 $\delta = .0008$   
 $\delta_{\text{eff}} = .008$

$a = 1.421 \text{ cm}$   
 $1.3605 \text{ cm}$   
 $1.342 \text{ cm}$   
 frequency increment  $5 \text{ MHz}$

$\triangle \triangle \triangle$   
 $\square \square \square$   
 $\circ \circ \circ$

Figure 4-2: The shift of the calculated impedance locus, (1,1) mode, as the inner radius  $a$  is decreased,  $\Lambda = 6.0$ .



$b = 9.158 \text{ cm}$   
 $\rho' = 1.5 \text{ cm}$   
 $\Delta = .00012 \text{ cm}$   
 $\delta = .0012$   
 $\delta_{\text{eff}} = .008$

$a = 1.50 \text{ cm}$   
 $1.3605 \text{ cm}$   
 $1.342 \text{ cm}$   
 frequency increment  $30 \text{ MHz}$

$\triangle$   $\triangle$   $\triangle$   
 $\square$   $\square$   $\square$   
 $\bullet$   $\circ$   $\bullet$

Figure 4-3: The shift of the calculated impedance locus, (4,2) mode, as the inner radius  $a$  is decreased,  $\Lambda = 6.0$ .

More interesting is the fact that the edge correction does not simply rotate the impedance locus, but that in certain cases it can shift the magnitude substantially. Figure 4-5 shows experimental and calculated impedance plots of a single antenna with  $\Lambda = 6.0$  (6.82) for varying feed points. As the feed approaches the inner radius, the uncorrected theory increasingly deviates from the experiment. Although the impedance calculated using the modified dimensions also deviates slightly, which may be corrected by a better choice for the edge correction, it is clear that slightly changing the antenna measurements is a necessary correction if an accurate predictive model for the properties of the microstrip antenna is required.

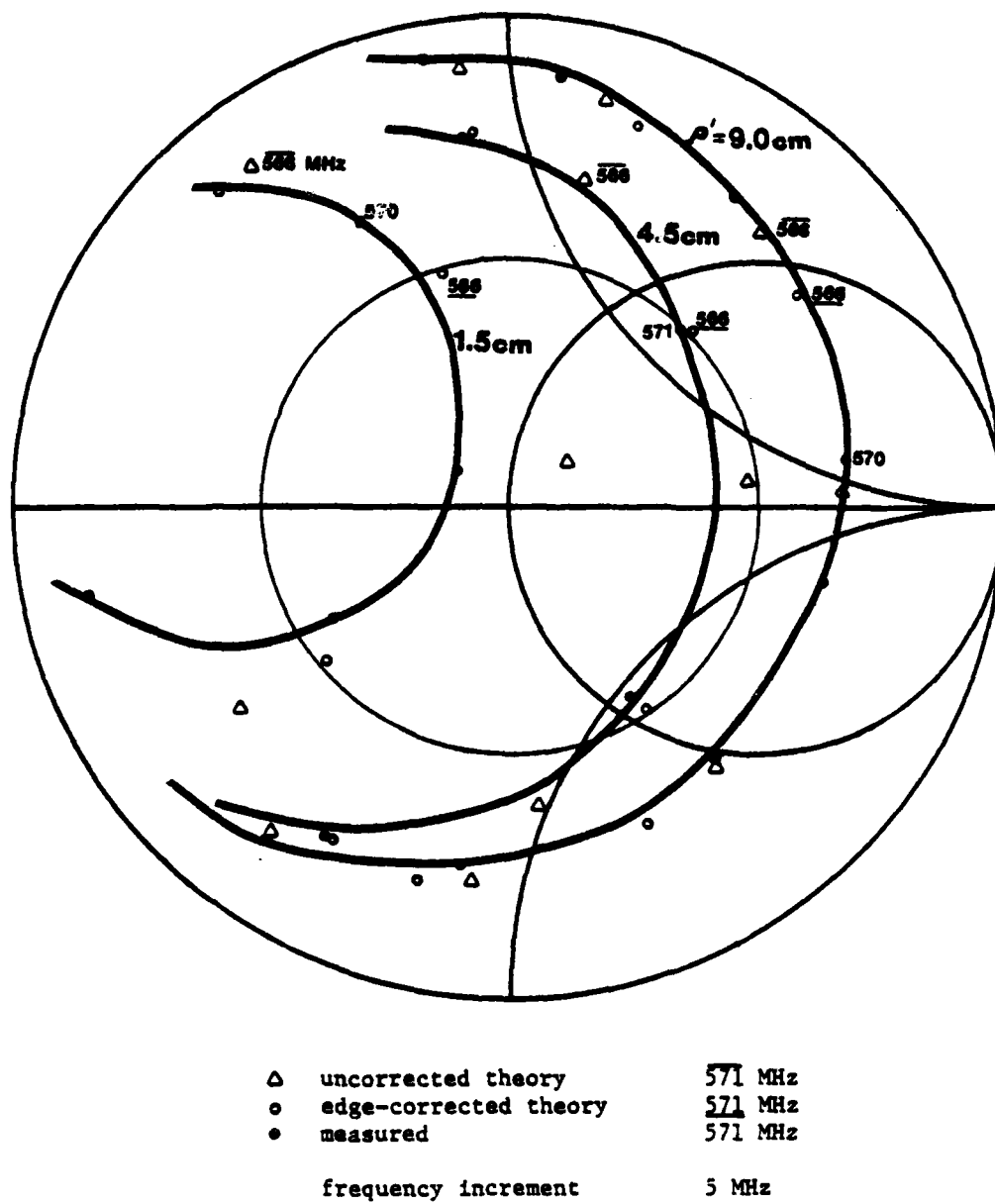


Figure 4-4: Measured and calculated impedance loci, (1,1) mode,  $\Lambda = 6.0$ , with impedance calculated both with and without edge correction,  $\rho' = 9.0, 4.5, 1.5$  cm.

## CONCLUSION

In this thesis, a method for analyzing thin microstrip antennas, by approximating the antenna as a closed cavity, was applied to an annularly shaped patch. The theory was examined in detail and expressions for the internal fields, losses, radiation pattern, and input impedance were obtained. Analytic calculations and experimental results of the input impedance, resonant frequencies, and radiation pattern were compared. The excellent agreement between theory and experiment demonstrates the validity of the approximation technique.

The suitability of annular patches in designing tunable antennas that operate at two bands with similar impedance and radiation characteristics was examined. It was shown that such operation is indeed possible, and a method was outlined for their construction. The lower order modes of the annular antenna exhibit very similar radiation patterns, and the ratio between the two operating frequencies can be varied by choosing appropriate values for the inner and outer radii. Theoretically, the ratio between the first and second resonant frequencies for  $n = 1$  varies from 7.92 to 2.88 as  $\Lambda$  changes from 1.5 to 10.0. For the antenna studied here with intermediate values of  $\Lambda$ , ratios between resonant frequencies from 2.8 to 3.4 were obtained.

As with all thin microstrip antennas, the operation is very narrow banded. However, for theoretical calculations, a multipoint theory over a wide frequency range has been developed and already applied to the study of the rectangular microstrip antenna. Such an analysis could be extended to the annular patch.

The effects of the fringing fields at the edges of the antenna were also examined in detail. As expected, there is a slight discrepancy between measured resonant frequencies and those predicted by the cavity model, a discrepancy that can be corrected for by adding a small edge correction to account for the fringing fields. More significantly, in certain cases these fringing fields can also substantially shift the impedance characteristics, and this shift can also be predicted by adding approximately the same edge correction.

For these thin antennas, a single edge correction, a change in dimension approximately the thickness of the antenna, has been used throughout and shown to yield satisfactory results. Since the efficiency of microstrip antennas increases with their thickness, a logical extension of this work is towards study of the properties of thicker antennas. However, as already noted, the effects of the fringing fields for thicker antennas are expected to be more pronounced, and the edge correction needed to accurately predict their characteristics would be more complicated. The change in dimensions of the inner and outer radii need not be equal, and might be dependent on the frequency of excitation, the magnitude of the E field, or the antenna curvature at the edge.

Although the nature of the necessary correction is an open question, it is clear that the fringing fields must be accounted for in order to develop an accurate predictive model for designing thick microstrip antennas. This correction might become increasingly important if the analysis is extended to the wide band multi-port theory already mentioned.

## APPENDIX A

## CALCULATION OF THE ELECTRIC STORED ENERGY

If  $U_n(K\rho)$  is a solution of Bessel's equation

$$\int_a^b |U_n(K\rho)|^2 \rho d\rho = \frac{\rho^2}{2} \left\{ \left[ U_n(K\rho) \right]^2 + \left[ 1 - \frac{n^2}{(K\rho)^2} \right] \left[ U_n'(K\rho) \right]^2 \right\} \Big|_a^b \quad (A.1)$$

Using this relation, after some simplification, (2.80) can be written in closed form

$$\begin{aligned} W_E &= \frac{\epsilon \epsilon_0 \omega^2 \mu^2}{2} \sum_{n=0}^{\infty} \frac{1}{(1 + \delta_{0n}) \Delta_n^2} \left\{ \frac{2}{\pi^2 K_1^2} \left[ 1 - \frac{n^2}{(K_1 b)^2} \right] \cdot \right. \\ &\quad [J_n(K_1 \rho') N_n'(K_1 a) - N_n(K_1 \rho') J_n'(K_1 a)]^2 \\ &\quad - \frac{2}{\pi^2 K_1^2} \left[ 1 - \frac{n^2}{(K_1 a)^2} \right] \cdot [J_n(K_1 \rho') N_n'(K_1 b) - N_n(K_1 \rho') J_n'(K_1 b)] \\ &\quad + \frac{\rho'}{2} \{ [J_n(K_1 \rho') N_n'(K_1 b) - N_n(K_1 \rho') J_n'(K_1 b)]^2 \cdot \\ &\quad [J_n'(K_1 \rho) N_n'(K_1 a) - N_n'(K_1 \rho') J_n'(K_1 a)]^2 \\ &\quad - [J_n(K_1 \rho') N_n'(K_1 a) - N_n(K_1 \rho') J_n'(K_1 a)]^2 \cdot \end{aligned}$$



$$\left. [J'_n(K_1 \rho') N'_n(K_1 b) - N'_n(K_1 \rho') J'_n(K_1 b)]^2 \right\}$$

where  $\Delta_n$  is defined in equation (2.54).

## APPENDIX B

## RESONANT FREQUENCY AND THE EDGE EFFECT

As noted in chapter 3, the calculated resonant frequencies differ in a very regular way from the experimental values. For low order resonances, the predicted frequencies are too low, but as the frequency of excitation increases, this difference between theory and experiment decreases, and finally the theory predicts values that are too high.

In chapter 4 this discrepancy is examined in depth, and explained as due to the presence of fringing fields at the edges of the antenna. But it is interesting to note that this general phenomenon can be qualitatively explained with a very simple model.

The shift in the resonant frequency  $\Delta f$ , due to a small change in the inner radius  $a$  can be expressed as

$$\Delta f = \frac{\partial f}{\partial a} \Delta a + \frac{\partial f}{\partial \Lambda} \Delta \Lambda \quad (\text{B.1})$$

since

$$f_r = \frac{c R_{nm}}{2\pi a(\epsilon)^{1/2}} \quad (\text{B.2})$$

where

$c$  = speed of light

$R_{nm}$  = root of (2.24) which defines the resonance condition

$\epsilon$  = relative permittivity of the substrate

Therefore

$$\frac{\partial f}{\partial a} = \frac{-c R_{nm}}{2\pi(\epsilon)^{1/2} a^2} \quad (\text{B.3})$$

and

$$\frac{\partial f}{\partial \Lambda} = \frac{\partial f}{\partial R_{nm}} \frac{\partial R_{nm}}{\partial \Lambda} = \frac{c}{2\pi a(\epsilon)^{1/2}} \frac{\partial R_{nm}}{\partial \Lambda} \quad (\text{B.4})$$

Substituting into (A.1) we obtain

$$\Delta f = \frac{c}{2\pi(\epsilon)^{1/2} a} \left( \frac{\partial R_{nm}}{\partial \Lambda} \Delta \Lambda - \frac{R_{nm}}{a} \Delta a \right) \quad (\text{B.5})$$

In compensating for the edge effect, the change in  $a$  is always negative, so that (A.5) may more clearly be written

$$\Delta f = \frac{c}{2\pi(\epsilon)^{1/2} a} \left( \frac{\partial R_{nm}}{\partial \Lambda} \Delta \Lambda + \frac{R_{nm}}{a} |\Delta a| \right) \quad (\text{B.6})$$

The second term within the parentheses is thus always positive, tending to shift the calculated resonance higher, and, from Figures 2.2 and 2.3 it is clear that  $\partial R_{nm}/\partial \Lambda$  (excluding very large values of  $\Lambda$ ) is always negative. More importantly, for a given value of  $\Lambda$ , as  $m$  increases, that is, as the frequency increases,  $\partial R_{nm}/\partial \Lambda$  is also increasing negative. Thus for low order resonances, the second term may dominate, shifting the resonant frequency higher, but at higher frequencies, the first term becomes increasingly important, and resonance occurs at a lower frequency than predicted by the cavity model.

## LIST OF REFERENCES

- [1] Lo, Y.T. et al., "Study of Microstrip Antenna Elements, Arrays, Feeds, Losses and Applications," Report No. RADC-TR-81-98, June, 1981. AD# A104 493.
- [2] Sanford, G.G. and R.E. Munson, "Conformal VHF Antenna for the Apollo-Soyuz Test Project," IEEE AP-S Int. Symp. Digest, Oct. 1976, pp. 113-116.
- [3] Derneryd, A.G. "Microstrip Disc Antenna Covers Multiple Frequencies," Microwave Journal, pp. 77-79, May 1978.
- [4] Lo, Y.T., D.D. Harrison, and W.F. Richards, "An Analysis of the Disk Microstrip Antenna, Part II," Report No. RADC-TR-79-132, May 1979. AD# A070 794.
- [5] Richards, W.F., Y.T. Lo, and D.D. Harrison, "An Improved Theory for Microstrip Antennas and Applications," IEEE Transactions on Antennas and Propagation, vol. AP-29, No. 1, pp. 38-46, January 1981.
- [6] Lo, Y.T., D. Solomon, and W.F. Richards, "Theory and Experiment on Microstrip Antennas," IEEE Transactions on Antennas and Propagation, vol. AP-27, No. 2, pp. 137-145, March 1979.
- [7] Lo, Y.T., W.F. Richards, and J.E. Brewer, "Evaluation of Losses in Microstrip Antenna Materials," Report No. RADC-TR-80-85, April 1980. AD# A087 476.
- [8] Shen, L.C., "Resonant Frequency of a Circular Disk, Printed Circuit Antenna," IEEE Transactions on Antennas and Propagation, vol. AP-25, pp. 595-596, July 1977.

- [9] Abramovitz, M. and I.A. Stegun, Handbook of Mathematical Functions. New York: Dover Publications, Inc., 1965.
- [10] Watson, G.N., A Treatise on the Theory of Bessel Functions. New York: The MacMillan Co., 1944.

## PART II - Dual-Frequency Rectangular Microstrip Antennas

## CHAPTER 1

## INTRODUCTION

A rectangular microstrip antenna can resonate at many frequencies corresponding to various modes. However, in order for such a multiple frequency antenna to be useful many requirements must be met. First the antenna must have similar, if not identical, radiation patterns for the frequency bands of interest (for example, the dominant radiation be broadside, i.e., normal to the patch for all frequencies). Second, the dominant radiation fields for all bands must have the same polarization. Third, the antenna input impedance can be matched closely to the line, say 50 ohms, for all bands. Fourth, it is desirable to have a single feed for all bands. Fifth, the antenna can operate in two or more frequency bands over a range as large as possible.

In view of these conditions, one can immediately conclude that operations of many modes are not acceptable. For example, the modes (0,1) and (1,0) are not useful since they produce radiations of completely two different polarizations. Furthermore, it is generally not possible to have one element to operate over two or more bands with very large differences in frequencies still having good patterns. This is because the element dimension which is proper for the low band would be too large for the high band, resulting in grating lobes and/or large cross-polarized field. Therefore, even though operation over many bands is possible in principle, we shall confine our investigation to the two lowest useful modes, namely the (0,1) and

(0,3) modes of the rectangular patch. (Note that the (0,2) mode is not useful since its radiation pattern has a null in the broadside direction.)

For a dual frequency rectangular microstrip antenna to operate at the (0,1) and (0,3) modes, the two operating frequencies always have a fixed ratio, namely three in this case (the exact number depends on the fringing field structure). To remove this restriction, shorting pins are placed along the nodal lines of the (0,3) modal field. In so doing, these pins will have practically no effect on the (0,3) modal field structure but can alter the (0,1) modal field, therefore its stored energy, drastically. As a result, the (0,1) modal frequency can be tuned independently over a wide range, thus providing some flexibility in design. Because of the large change in the field the usual perturbation theory becomes useless in evaluating the effect of shorting pins. Fortunately, the multi-port theory developed previously can predict their effect on frequency and impedance very well. This is discussed in Chapter 2.

As explained above, a patch designed to operate for the (0,3) mode may be too large in the sense that undesirable grating lobes may appear since the two radiating magnetic line sources are separated  $3/2 \lambda$  apart,  $\lambda$  being the wavelength in substrate. There are two ways to alleviate this problem. The first is to use substrate with higher permittivity (around four or higher in relative permittivity). The second is to cut the rectangle in y by one-half and to electrically short this edge to the ground plate with either copper tape or sufficiently large number of conducting pins. In so doing, only one

magnetic line current remains and thus interferring grating lobes and nulls are avoided. However, as expected the Q-factor of this antenna would be somewhat higher than that of a regular rectangular patch. Nevertheless, because of the availability of materials, the second method is considered in this investigation while the first method is straightforward and does not need further study.



CHAPTER 2  
THEORY OF A MODIFIED RECTANGULAR  
MICROSTRIP ANTENNA

2-1 GENERAL ANALYSIS FOR THE FIELD IN THE PATCH

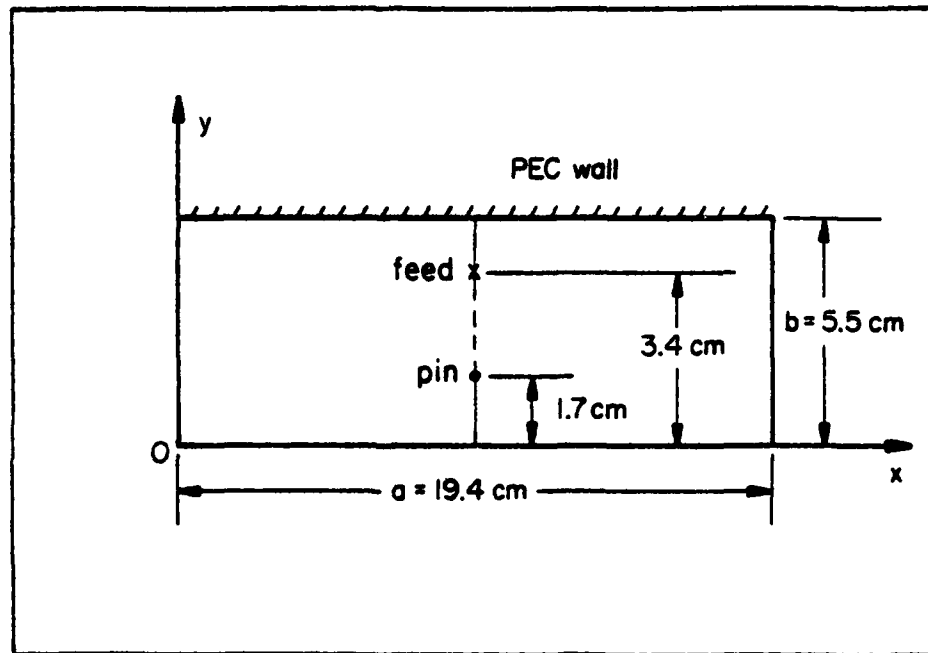
Consider a rectangular microstrip patch defined by  $0 \leq x \leq a$  and  $0 \leq y \leq b$  as shown in Figure 1. In contrast to the conventional design, an electrically shorting wall is placed at  $y = b$ . This can be achieved in practice by cutting a slot at  $y = b$  and  $0 \leq x \leq a$  and soldering a copper tape along the slot to both the patch and the ground plate, or by inserting a sufficiently large number of shorting pins along the edge  $y = b$ . Let the feed be located at  $(x_1, y_1)$ ; then from the cavity model theory one has for the field the following expressions:

in region 1 ( $0 \leq x \leq x_1$ ),

$$\begin{aligned} E_z &= \sum_m A'_m \cos \beta_m x \cos \frac{m\pi}{2b} y, \\ H_x &= -\frac{j}{\omega\mu_0} \sum_m A'_m \frac{m\pi}{2b} \cos \beta_m x \sin \frac{m\pi}{2b} y, \\ H_y &= \frac{j}{\omega\mu_0} \sum_m A'_m \beta_m \sin \beta_m x \cos \frac{m\pi}{2b} y; \end{aligned} \quad (1)$$

in region 2 ( $x_1 \leq x \leq b$ ),

$$\begin{aligned} E_z &= \sum_m A_m \cos \beta_m (a - x) \cos \frac{m\pi}{2b} y \\ H_x &= -\frac{j}{\omega\mu_0} \sum_m A_m \frac{m\pi}{2b} \cos \beta_m (a - x) \sin \frac{m\pi}{2b} y \\ H_y &= \frac{j}{\omega\mu_0} \sum_m A_m \beta_m \sin \beta_m (a - x) \cos \frac{m\pi}{2b} y \end{aligned} \quad (2)$$



$$t = 0.32 \text{ cm}$$

$$\sigma = 270 \text{ k}\Omega$$

$$\epsilon_r = 2.62$$

Figure 1. A modified rectangular microstrip antenna with a short-circuit pin.

AD-A122 404

A STUDY OF MICROSTRIP ANTENNAS FOR MULTIPLE BAND  
OPERATION(U) ILLINOIS UNIV AT URBANA DEPT OF ELECTRICAL  
ENGINEERING Y T LO ET AL. SEP 82 UIIU-EM-82-3

2/2

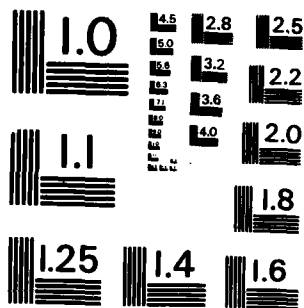
UNCLASSIFIED

RADC-TR-82-236 AFOSR-81-0234

F/Q 9/8

NL


END  
DATE  
FORMED  
183  
D14



MICROCOPY RESOLUTION TEST CHART  
NATIONAL BUREAU OF STANDARDS-1963-A

where

$$\beta_m^2 = k^2 - \left(\frac{m\pi}{2b}\right)^2$$

$$k^2 = k_o^2 \epsilon_r (1 - j\delta)$$

$$k_o^2 = \omega^2 \mu_o \epsilon_o$$

$\mu_o$  = permeability of free space

$\epsilon_o$  = permittivity of free space

$\epsilon_r$  = relative permittivity of the substrate with respect  
to  $\epsilon_o$

$\delta_{eff}$  = effective loss tangent

$\sum'_m$  = summation over all positive odd integers only

For simplicity let the feed excitation be a  $\hat{z}$ -directed electric current of one ampere, uniformly distributed over a ribbon of width  $d$ , and center at  $(x_1, y_1)$ ; i.e.,

$$\vec{J}(x, y) = \hat{z} J_z \delta(x - x_1) \quad ,$$

with

$$J_z = \frac{U(y - y_1 + d/2) - U(y - y_1 - d/2)}{d} \quad ,$$

$U(\cdot)$  = unit step function.

Applying the boundary conditions at  $x = x_1$ :

$$H_y^{(2)} - H_y^{(1)} = J_z \quad ,$$

$$E_z^{(2)} = E_z^{(1)},$$

one determines the expansion coefficients as given below.

$$A_m = j k_o \eta_o \frac{2 \cos \beta_m x_1}{b \beta_m \sin \beta_m a} \cos \frac{m\pi}{2b} y_1 j_o \left( \frac{m\pi d}{4b} \right), \quad (3)$$

$$A'_m = A_m \frac{\cos \beta_m (a - x_1)}{\cos \beta_m x_1}, \quad (4)$$

where

$$\eta_o = 377 \text{ ohms},$$

$$j_o(x) = \frac{\sin x}{x}.$$

## 2-2 INPUT IMPEDANCE

From  $E_z$  the input impedance can be found:

$$Z_{in} = - \frac{j 2k_o \eta_o t}{b} \sum_m \frac{\cos \beta_m x_1 \cos \beta_m (a - x_1)}{\beta_m \sin \beta_m a} \cos^2 \frac{m\pi y_1}{2b} j_o^2 \left( \frac{m\pi d}{4b} \right), \quad (5)$$

## 2-3 FAR FIELD

The cavity model assumes that the field under the patch is not much different from that of the corresponding cavity shown above. Next, based on the Huygen's principle one can find the radiation field from the equivalent Huygen source. It is reasonable to further assume that the electric currents on the exterior surfaces of the patch and the shorting tape at  $y = b$  are so small that their contribution to the far field can be neglected as compared with

that due to the magnetic current along the three walls at  $x = 0$ ,  $x = a$ , and  $y = 0$ . The magnetic current at these boundaries is

$$\vec{K} = \hat{n} \times \hat{z} E_z$$

where  $\hat{n}$  is the unit normal vector pointing away from the patch at the boundary and  $E_z$  is the field at that point. So far as the far field is concerned, one can even ignore the presence of a thin dielectric substrate over the ground plane in computation. With this simplification the electric vector potential of the far field is

$$\vec{F} = \frac{e^{-jk_0 r}}{4\pi r} 2t \int_{\text{patch boundary}} \vec{K}(x,y) e^{jk_0(x\sin\theta\cos\phi + y\sin\theta\sin\phi)} dl$$

where the factor 2 accounts for the image current due to the ground plane and  $t$  is resulted from the integration with respect to  $z$ . Using Equations (1) and (2),  $\vec{F}$  can be written as

$$\vec{F} = \frac{jk_0 \eta_0 t}{\pi b r} e^{-jk_0 r} \sum_m \frac{\cos(m\pi y_1/2b)}{\beta_m \sin\beta_m a} j_0(m\pi d/4b) (\hat{x}F_x + \hat{y}F_y) \quad (6)$$

where

$$F_x = - \frac{1}{\beta_m^2 - (k_0 \sin\theta \sin\phi)^2} \left[ \beta_m \sin(\beta_m a) e^{jk_0 y_1 \sin\theta \sin\phi} + jk_0 \sin\theta \sin\phi f \right] \quad (7)$$

$$F_y = \frac{f}{(m\pi/2b)^2 - (k_0 \sin\theta \cos\phi)^2} \left[ (-1)^{m+1/2} \frac{m\pi}{2b} e^{jk_0 b \sin\theta \cos\phi} - jk_0 \sin\theta \cos\phi \right] \quad (8)$$

$$f = \cos(\beta_m x_1) e^{jk_0 a \sin\theta \sin\phi} - \cos\beta_m (b - x)$$

The far field is given by

$$E_{\theta} = jk_0 (F_x \sin\phi + F_y \cos\phi) \quad , \quad (9)$$

$$E_{\phi} = jk_0 (F_x \cos\phi + F_y \sin\phi) \cos\theta \quad .$$

#### 2-4 Q-FACTOR

The Q-factor of the antenna at resonance is defined as

$$Q = \frac{\omega_0 (\text{time-average stored energy in the cavity})}{\text{total time-average power loss}}$$

$$= \frac{2\omega_0 W_e}{P_r + P_c + P_d} \quad (10)$$

where

$$W_e = \frac{\epsilon \epsilon_r \epsilon_0}{2} \int_0^a \int_0^b E_z E_z^* dx dy \quad , \quad (11)$$

$$P_d = \omega \epsilon_r \epsilon_0 \delta t \int_0^a \int_0^b E_z E_z^* dx dy = 2\omega \delta W_e \quad , \quad (12)$$

$$P_c = \frac{\Delta}{t} (2\omega W_e) \quad ,$$

$$P_r = \text{Re} \frac{1}{\eta_j} \int_0^{\pi/2} \int_0^{2\pi} (E_{\theta} E_{\theta}^* + E_{\phi} E_{\phi}^*) r^2 \sin\theta d\theta d\phi \quad , \quad (14)$$

$\delta$  = loss tangent of the substrate

$\Delta$  = skin depth of the copper cladding.



The copper loss of the shorting tape at  $y = b$  is approximately equal to  $(t/2b) P_c$  which can be neglected for thin microstrip antennas.

As discussed in our previous report [2], in order to have a self-consistent theory an effective loss tangent is defined to be

$$\delta_{\text{eff}} = 1/Q = (P_r + P_c + P_d), \quad (15)$$

and its corresponding effective wave number,

$$k_{\text{eff}} = k_0 [\epsilon_r (1 - j\delta_{\text{eff}})]^{1/2}.$$

Then  $\delta_{\text{eff}}$  and  $k_{\text{eff}}$  are to be used in Equations (1), (2) and (5) for computing  $E_z$  and  $Z_{\text{in}}$ . This simplification is possible mainly because the Q-factor of thin microstrip antenna is rather high, typically 50-200.

## 2-5 MULTI-PORT THEORY AND APPLICATIONS TO ANTENNAS WITH SHORTING PINS

The theory discussed in the last section can be extended for analyzing microstrip antennas with shorting pins. Consider the general case of an antenna with N ports. Then,

$$\sum_j I_j Z_{ij} = V_i, \quad i, j = 1, \dots, N,$$

where by definition the mutual impedance  $Z_{ij}$  is given by

$$Z_{ij} = [V_i / I_j]_{I_i = 0 \text{ for all } i's \neq j}$$

= open circuit voltage at the i-th port due to a unit current input at the j-th port with all other ports open.

Since the solution to  $E_z$  anywhere in the patch for an input current anywhere in the patch has been obtained, it is almost trivial to compute  $Z_{ij}$ , which is

$$Z_{ij} = -jk_o \eta_o t \frac{2}{b} \sum_m \frac{\cos \beta_m x_i \cos \beta_m (a-x_j)}{\beta_m \sin \beta_m a} \cos \frac{m\pi y_i}{2b} \cos \frac{m\pi y_j}{2b} j_o \left( \frac{m\pi d_i}{4b} \right) j_o \left( \frac{m\pi d_j}{4b} \right)$$

where  $d_i$  and  $d_j$  are the effective widths of the pin and the feed conductor, respectively.

## CHAPTER 3

THEORETICAL AND EXPERIMENTAL RESULTS3-1 INTRODUCTION

Several antennas have been constructed and tested to verify our theoretical predictions. All of them were made of double copper-cladded laminate Rexolite 2200, 1/8" thick. In our previous investigation [3] the relative permittivity  $\epsilon_r$  was found to be approximately 2.62 and the loss tangent  $\delta = 0.001$  and the copper cladding conductivity  $\approx 270 \text{ KMho}$ . These values were used for the theoretical computations in this report.

The key point in our approach to the dual-frequency microstrip antenna is based on the prediction that short-circuit pins, if placed over the nodal lines of the (0,3) modal field, will have no effect on this mode, but may have substantial effect on the (0,1) mode. To test this theory several simple antennas were constructed and investigated in the beginning of this investigation; a typical one is reported in Section 3-2.

Having gained some understanding on the mechanism of shorting pins, a systematic study was then made for two antennas of different types with more and more shorting pins inserted. The purpose is to determine to what extent the (0,1) modal frequency could be varied and also how the input impedance would be changed.

For the following discussion, a word on "resonance" is perhaps in order. Often resonance of a system is referred to as the state where the reactive part of the input impedance vanishes. This

definition may be too restricted to be useful for microstrip antennas, because in some cases the input impedance locus of a microstrip antenna may not cross the real axis for a certain frequency band at all, (dependent on the feed location). But as the observation point moves along the feed line, the impedance locus rotates in the Smith chart and eventually intersects the real axis. But the intersecting point frequency varies as the observation moves further along the line. One may then wonder what exactly is the resonant frequency. To avoid this ambiguity, we shall define the resonant frequency of a microstrip antenna to be the one when the magnitude of input impedance  $|Z_{in}|$  reaches maximum.

As reported previously [2], the input impedance of the antenna can be represented by an inductance and an infinite number of parallel resonant circuits, each corresponding to a mode, in series. Usually it is the modal resonance which gives the desirable radiation pattern that is of interest. If all parallel circuits are lossless, the resonant frequency (more accurately, antiresonant frequency in the circuit language) for the input impedance, of course, coincides with that of each parallel circuit. If the parallel circuits are lossy this may no longer be true. For thin microstrip antennas, the Q-factor is sufficiently high so that when one of the parallel circuits reaches resonance, the input impedance magnitude becomes maximum in the narrow frequency band of interest, despite that the input reactance may not vanish due to the presence of other circuit elements in series. For this reason we define the resonance as indicated above.

### 3-2 MICROSTRIP ANTENNA WITH ONE SHORTING PIN

A rectangular microstrip antenna considered has the dimensions  $a = 19.4$  cm and  $b = 5.5$  cm as shown in Figure 1. Furthermore, the patch is electrically shorted to the ground plate at  $y = b = 5.5$  cm. This is done by first cutting a slot across the edge, then inserting a copper tape in the slot, and finally soldering the tape to both the patch and the ground plate. Alternatively, a row of electrically conducting pins of sufficiently large number can be used in place of the tape. Apparently, either method is not convenient in fabrication. Later we shall discuss a simpler variation.

A miniature coaxial cable feed is placed at  $x = 9.7$  cm and  $y = 3.4$  cm. The only reason for choosing this feed location is that it gives a nearly match impedance to the  $50 \Omega$  line for the (0,1) mode band. As will be discussed later, a better feed location for dual-frequency operation may actually be the one which would give the best input impedance value for the (0,3) mode, rather than (0,1) mode.

The input impedance loci at the feed for both modes are shown as the solid curves in Figures 2 and 3, respectively. Also shown in this figure are the theoretically predicted values as marked by crosses (x). The agreement between them is excellent for the low-frequency band and less favorable for the high (0,3) modal band. This is expected since the cavity model theory is more accurate for thin (in wavelength) antennas.

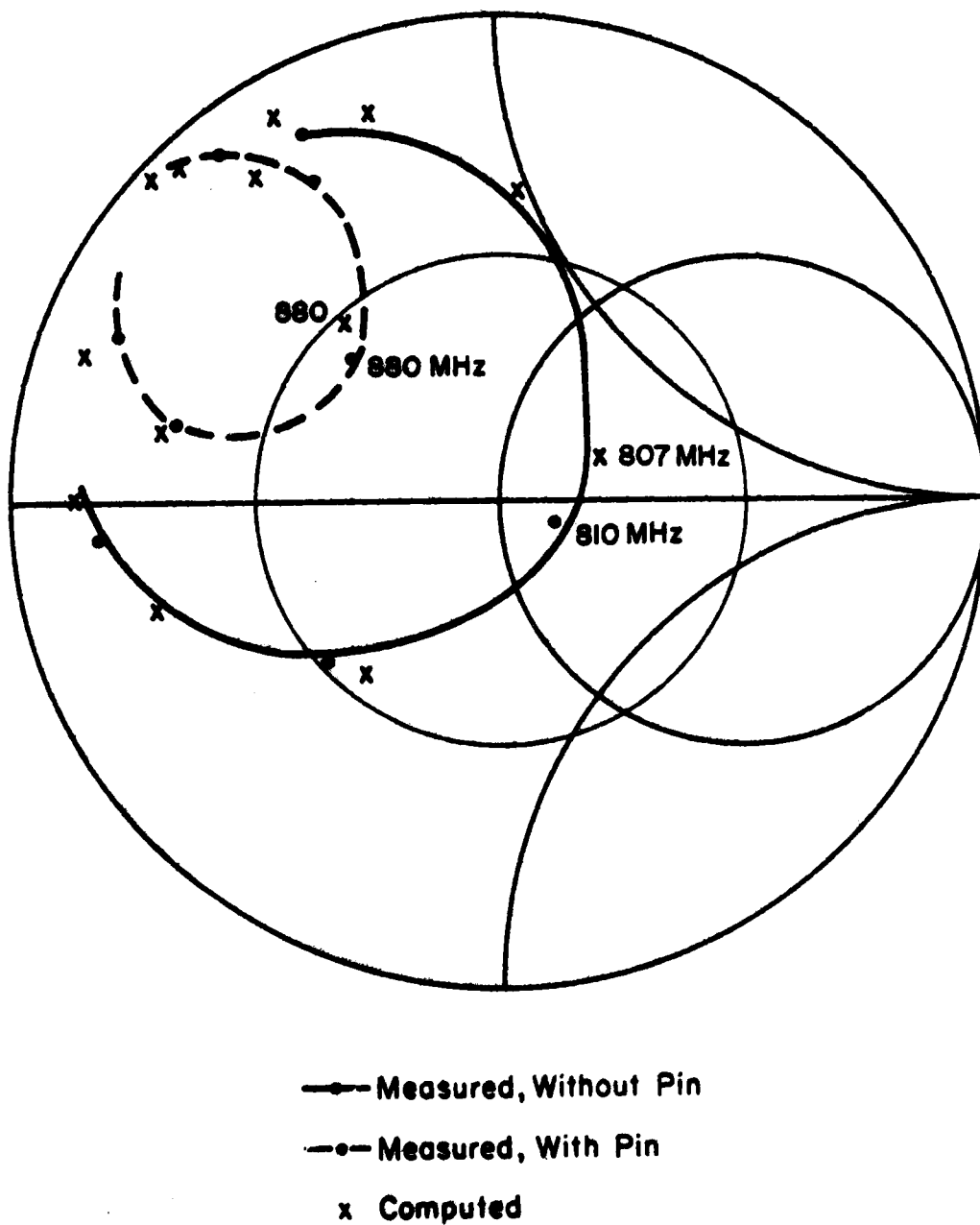
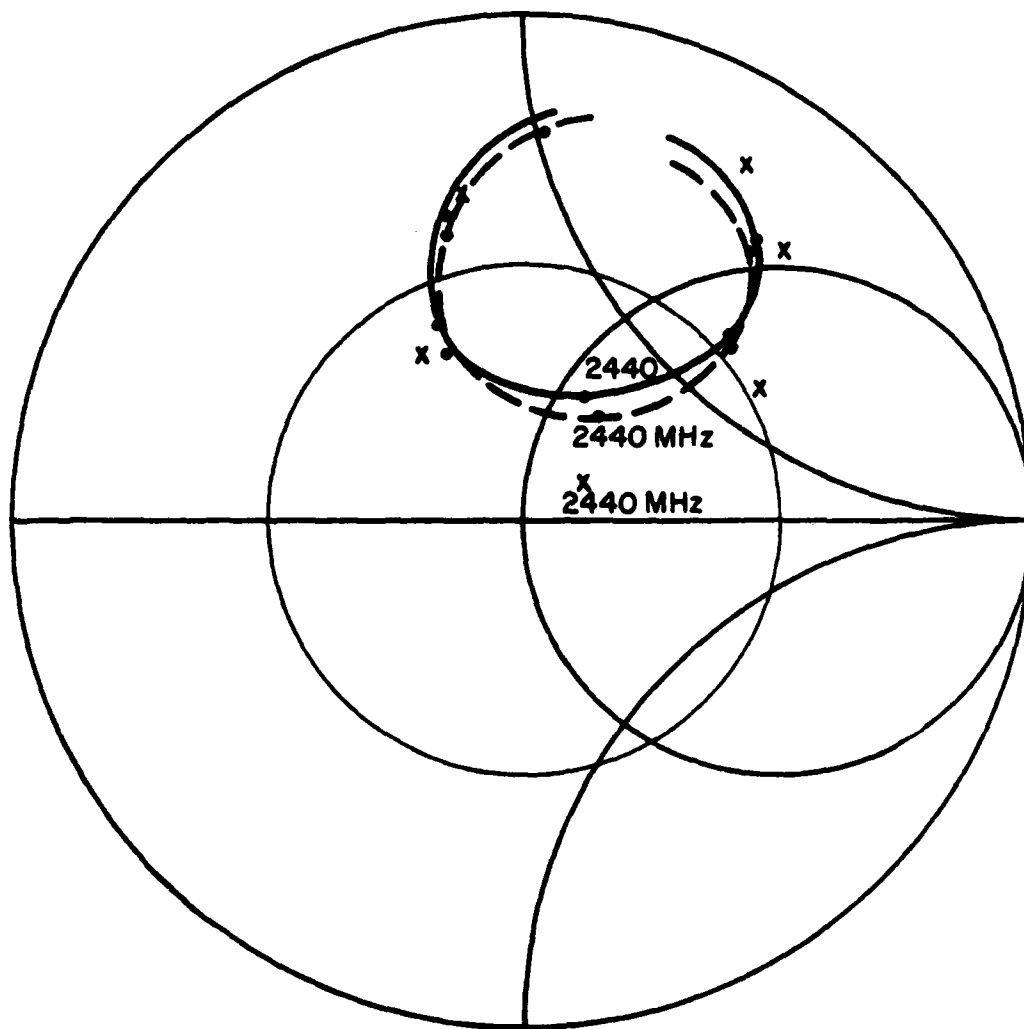


Figure 2. Measured and computed input impedance loci for the low band, with and without the shorting pin. Frequency increment between any two adjacent points  $\Delta f = 1$  MHz.



—●— Measured, Without Pin

-●- Measured, With Pin

x Computed, With Pin

Figure 3. Measured and computed input impedance loci for the high band, with and without the shorting pin. Frequency increment between any two adjacent points  $\Delta f = 20$  MHz.

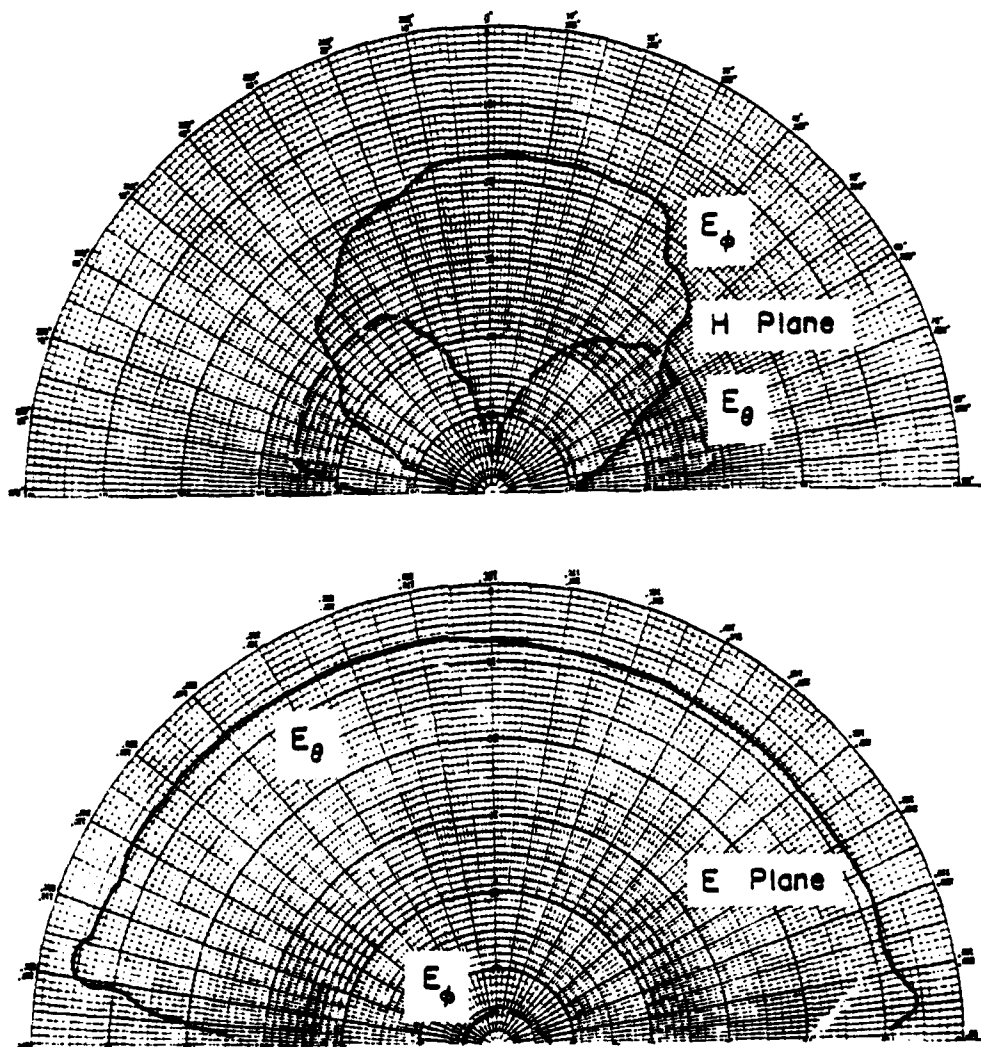


Figure 4. Radiation patterns in E- and H- plane at  $f = 813$  MHz of the rectangular microstrip antenna shown in Figure 1 without the pin.



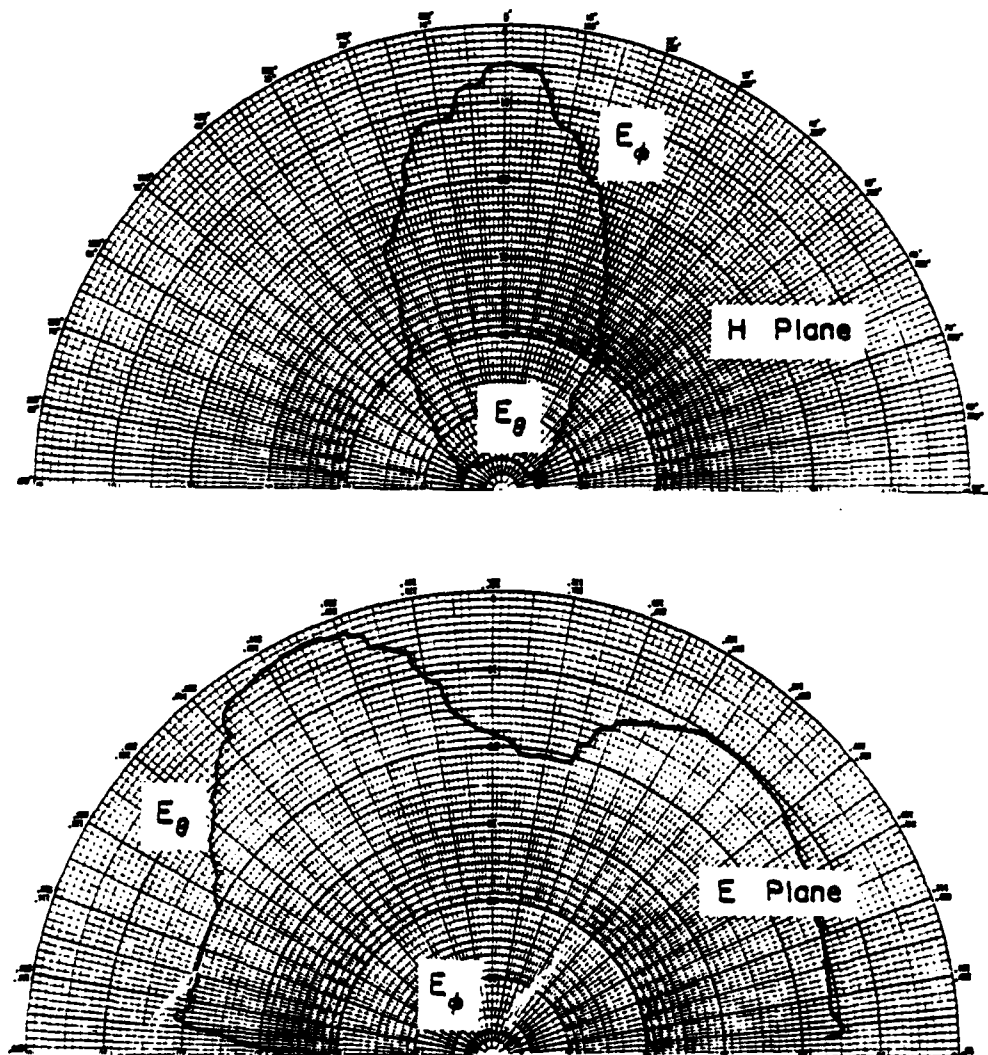


Figure 5. Radiation patterns in E- and H- plane at  $f = 2450$  MHz of the rectangular microstrip antenna shown in Figure 1 without the pin.

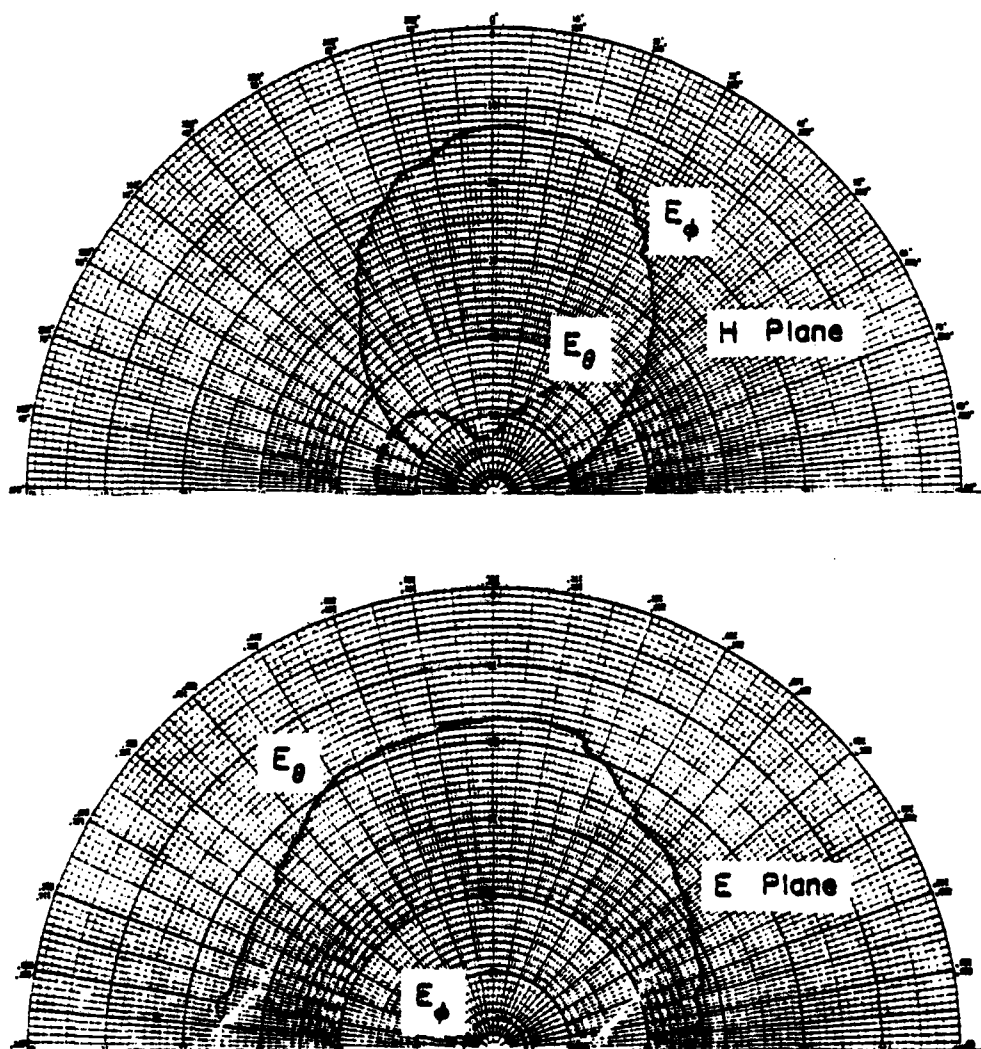


Figure 6. Radiation patterns in E- and H- plane at  $f = 885$  MHz of the rectangular microstrip antenna shown in Figure 1 with the pin.

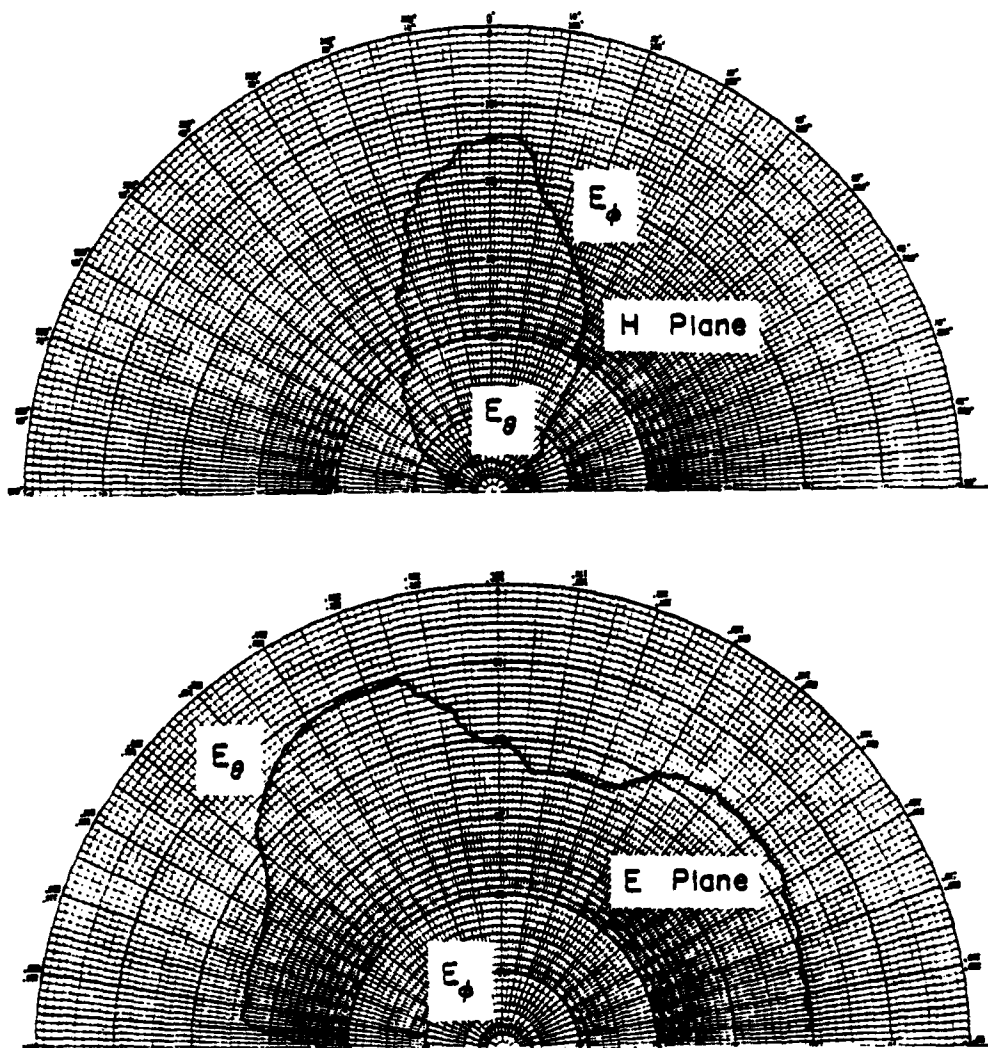


Figure 7. Radiation patterns in E- and H- plane at  $f = 2450$  MHz of the rectangular microstrip antenna shown in Figure 1 with the pin.

Now a shorting pin of radius about 0.025 cm is inserted at  $x = 9.7$  cm and  $y = 1.7$  cm which is approximately the electric field nodal line for the (0,3) mode. Because of the unknown fringing effect at the  $x = 0$  edge, the nodal line can be more accurately determined by counting one-half of the dielectric wavelength, i.e.,  $7.6/2$  cm, from the electric wall at  $y = 5.5$  cm, rather than counting  $1/4$  of the dielectric wavelength from  $y = 0$ . The impedance loci for both bands are again shown in Figures 2 and 3 as the dashed curves together with the computed results. First it is seen that the pin has practically no effect on the high band impedance locus. Second, not only the low band impedance locus is altered, the resonant frequency, as defined previously, is changed substantially. The radiation patterns for both low and high band resonant frequencies without and with the pin are shown in Figures 4 through 7. Again the patterns for the high band remain the same whether or not there is a pin inserted at the position indicated. However, for the low band, the resonant frequency is changed from 813 MHz to 885 MHz, but the major features of the patterns remain about the same. In fact, the beam in the E-plane becomes narrower and cross-polarized component smaller when the pin is used. This seems to be caused by the fact that the field contents of high order modes are changed due to the pin as can be seen from the theory in Chapter 2.

### 3-3 EFFECT OF MULTIPLE PINS ON RESONANT FREQUENCIES

Table 1 shows the variation of (0,1) modal frequency  $f_{01}$  with the number of shorting pins inserted at the locations as indicated in

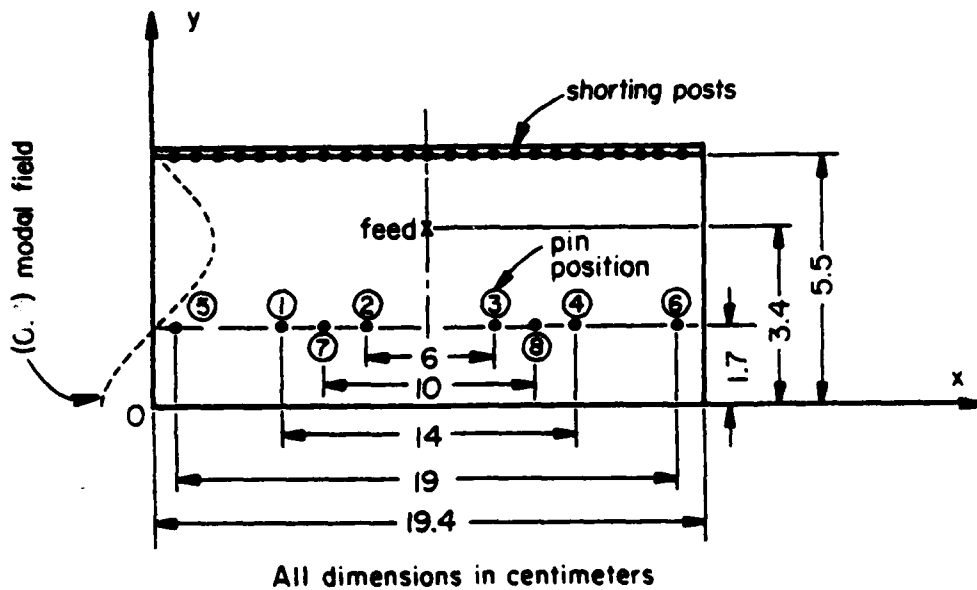


Figure 8. A modified rectangular microstrip antenna with one to eight shoring pins at the positions shown.

**TABLE 1.** Resonant frequencies for (0,1) and (0,3) modes vs. shorting pins used

Number of Pins	Pin Positions	$f_{01}$	$f_{03}$	$f_{03}/f_{01}$
0	---	805	2443	3.03
1	(3)	867	2445	2.82
2	(1)(3)	969	2445	2.52
3	(2)(3)(4)	1064	2445	2.30
4	(1) to (4)	1203	2445	2.00
6	(1) to (6)	1273	2445	1.92
8	(1) to (8)	1362	2445	1.80

Figure 8. For clarity, these results are plotted in Figure 9. Also shown in this figure is the plot of (0,3) modal frequency  $f_{03}$  versus the pins. It is seen that  $f_{03}$  is, within experimental error, perfectly constant, whereas  $f_{01}$  varies from 805 MHz to 1362 MHz, resulting in a variation from 3.03 to 1.8 for the ratio  $f_{03}/f_{01}$ . In fact, it is believed this ratio can be tuned even lower by adding more pins.

It may also be of interest to note that the change in  $f_{01}$  when pins No. 5 and No. 6 are used is less pronounced as compared with other pins. Similar phenomenon were discovered in our previous work [4] when a single shorting stub was moved close to the edge of the patch. This could be explained by the fact that as the shorting stub moves close to the edge the image electric current due to the magnetic wall would flow in such a direction that the inductance of the stub, or the stored magnetic energy, is reduced. It is also expected that as the pins are placed too close together, their effectiveness in frequency tuning may be reduced.

The input impedance loci for both high and low bands when all six pins are inserted in the positions (1) through (6) are shown in Figure 10. Comparing these loci with those shown in Figures 2 and 3 where no pins were used one finds that for the high band they are practically the same (the small difference is probably within our experimental error). But for the low band, even the frequencies are drastically changed. Typical radiation patterns when four pins are used are shown in Figures 11 and 12. The high band patterns

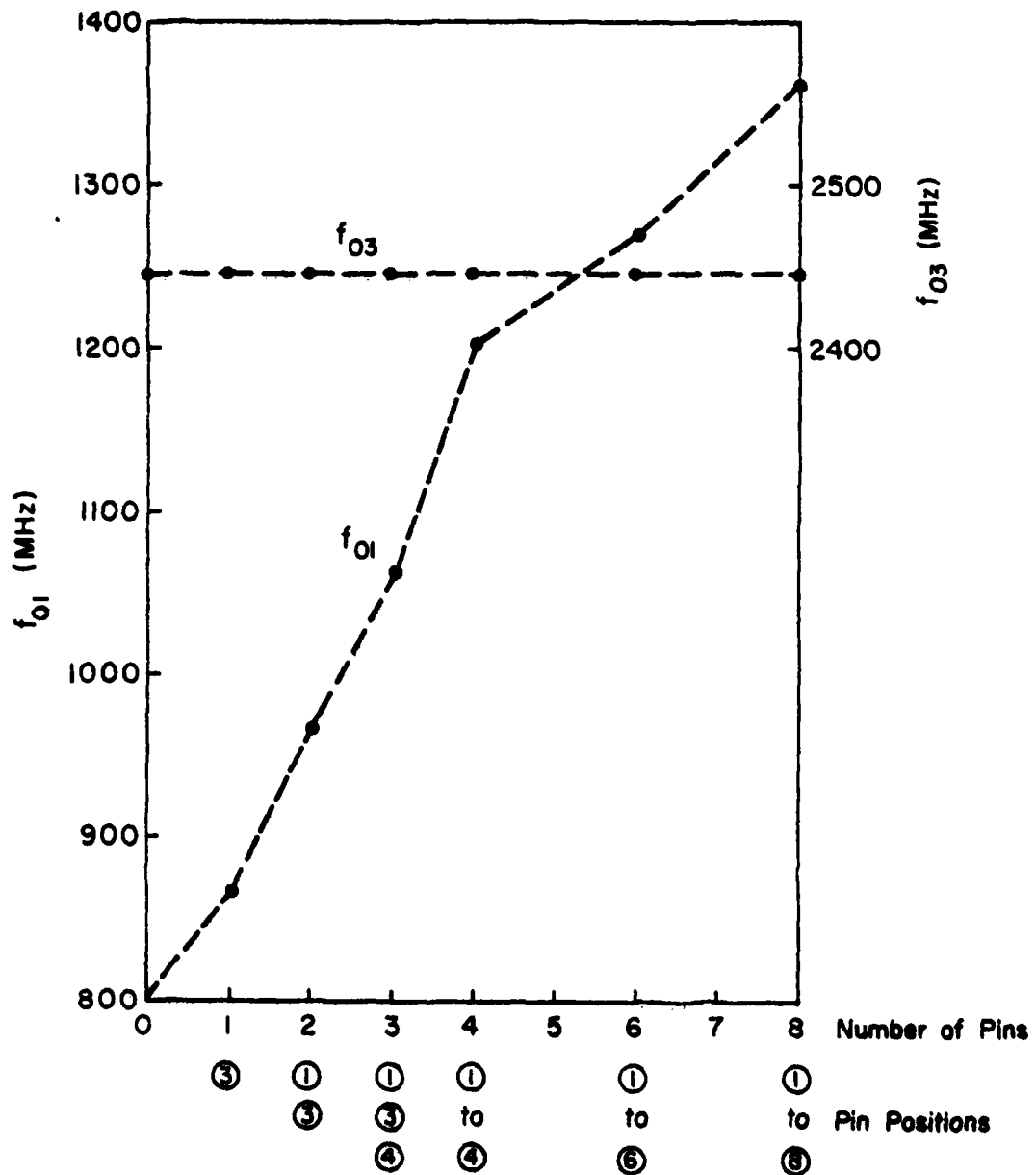


Figure 9. Variation of low and high band operating frequencies,  $f_{01}$  and  $f_{03}$  respectively, with the number of shorting pins inserted at the positions shown in Figure 8.



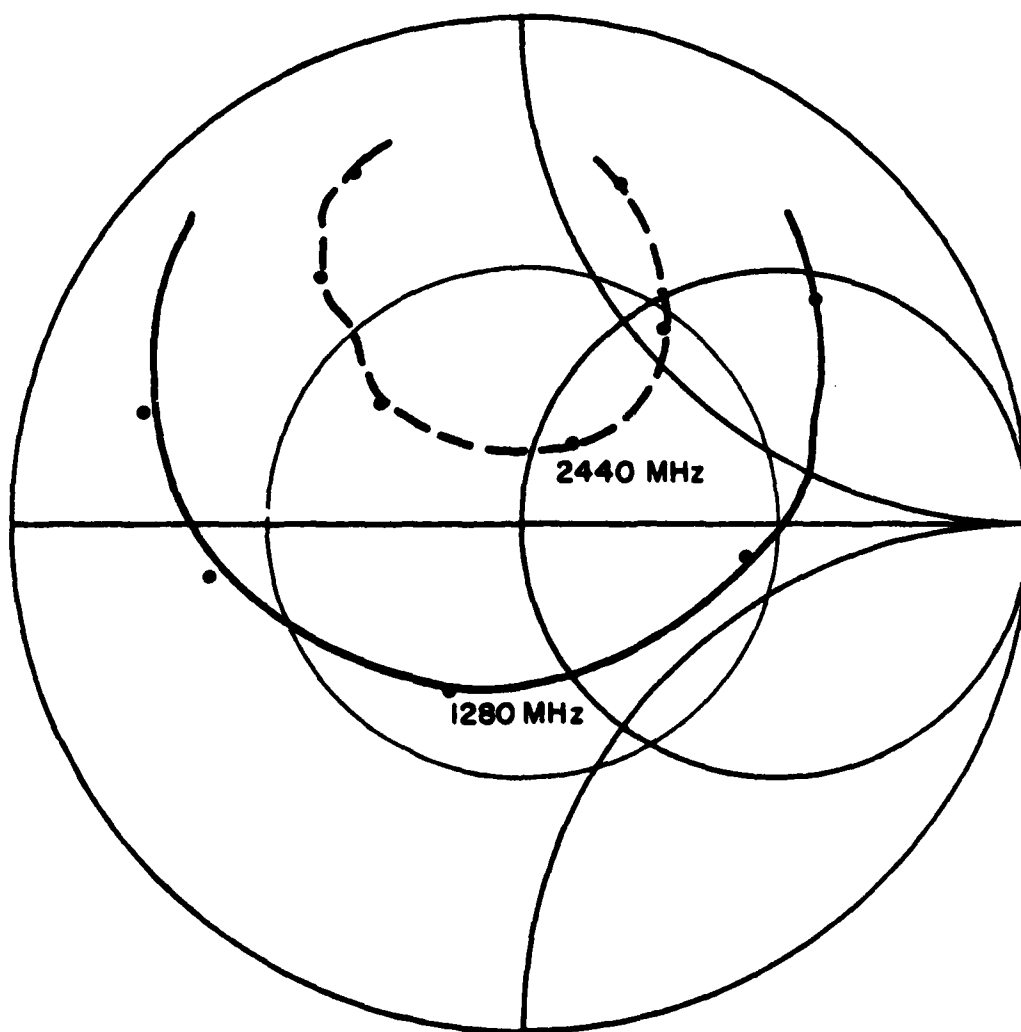


Figure 10. High- and low-band impedance loci of the antenna shown in Figure 8 with six pins inserted at positions (1) through (6). The frequency increment between adjacent points  $\Delta f = 20$  MHz.

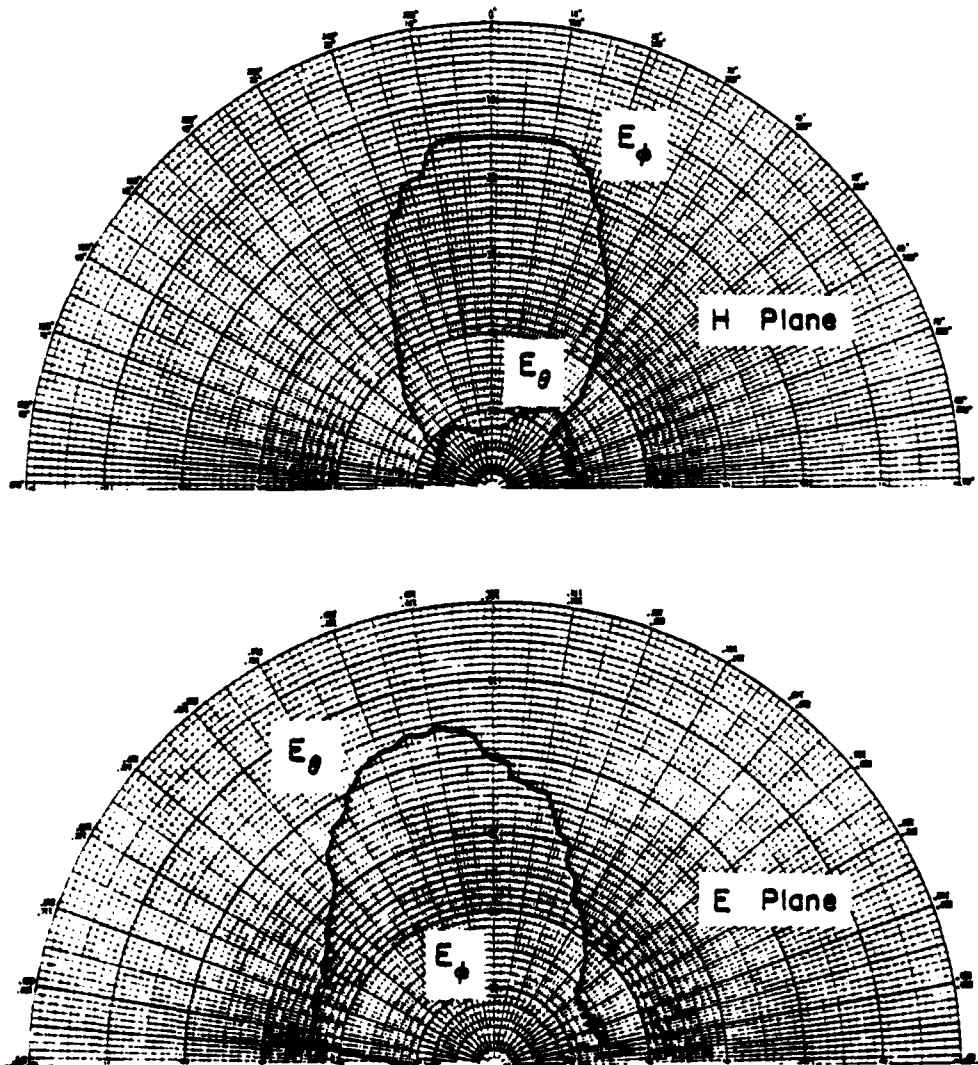


Figure 11. E- and H-plane radiation patterns at  $f = 1190$  MHz for the antenna shown in Figure 8 with four pins at positions (1) to (4).

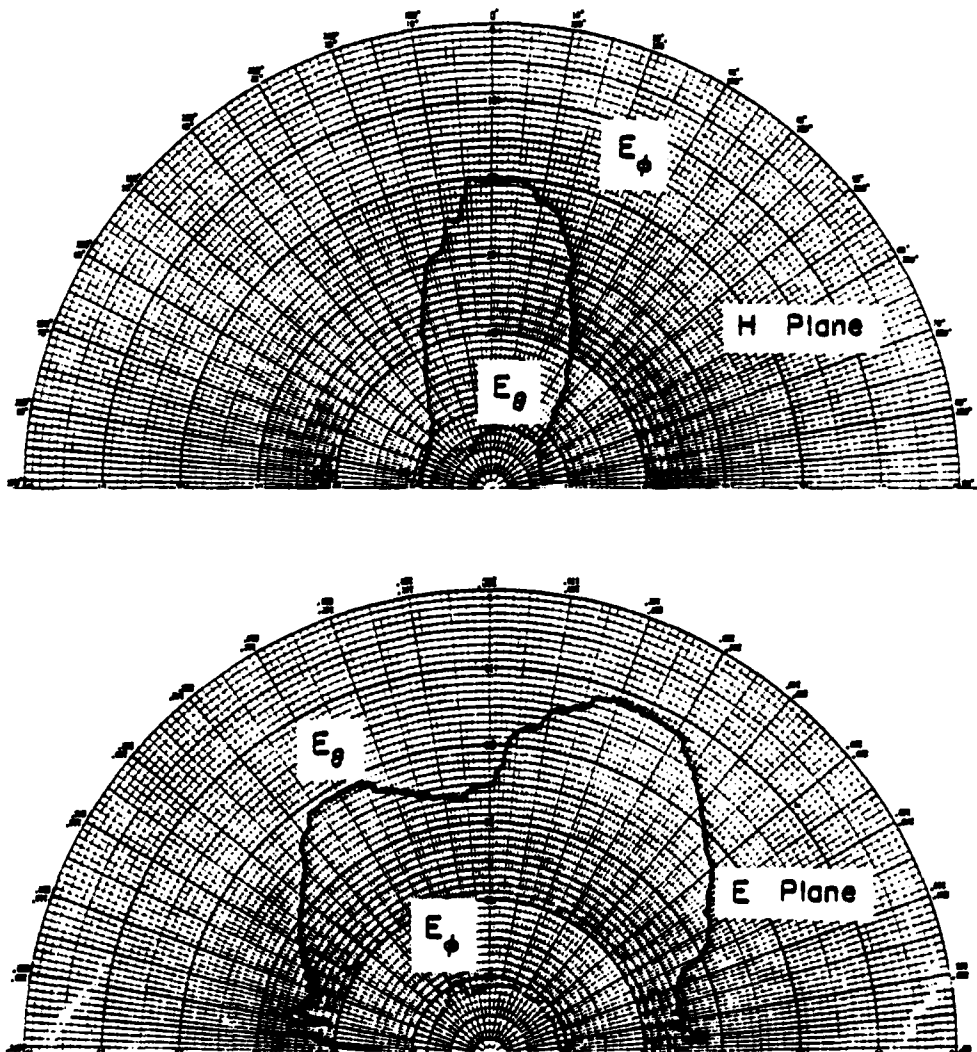


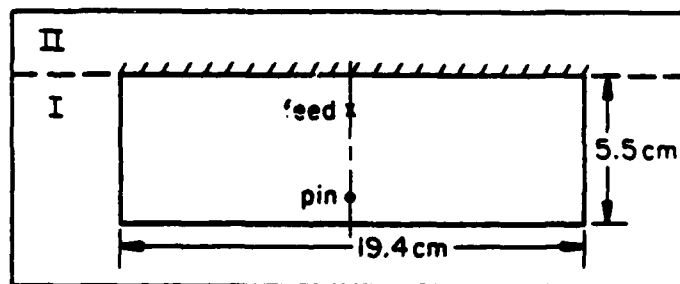
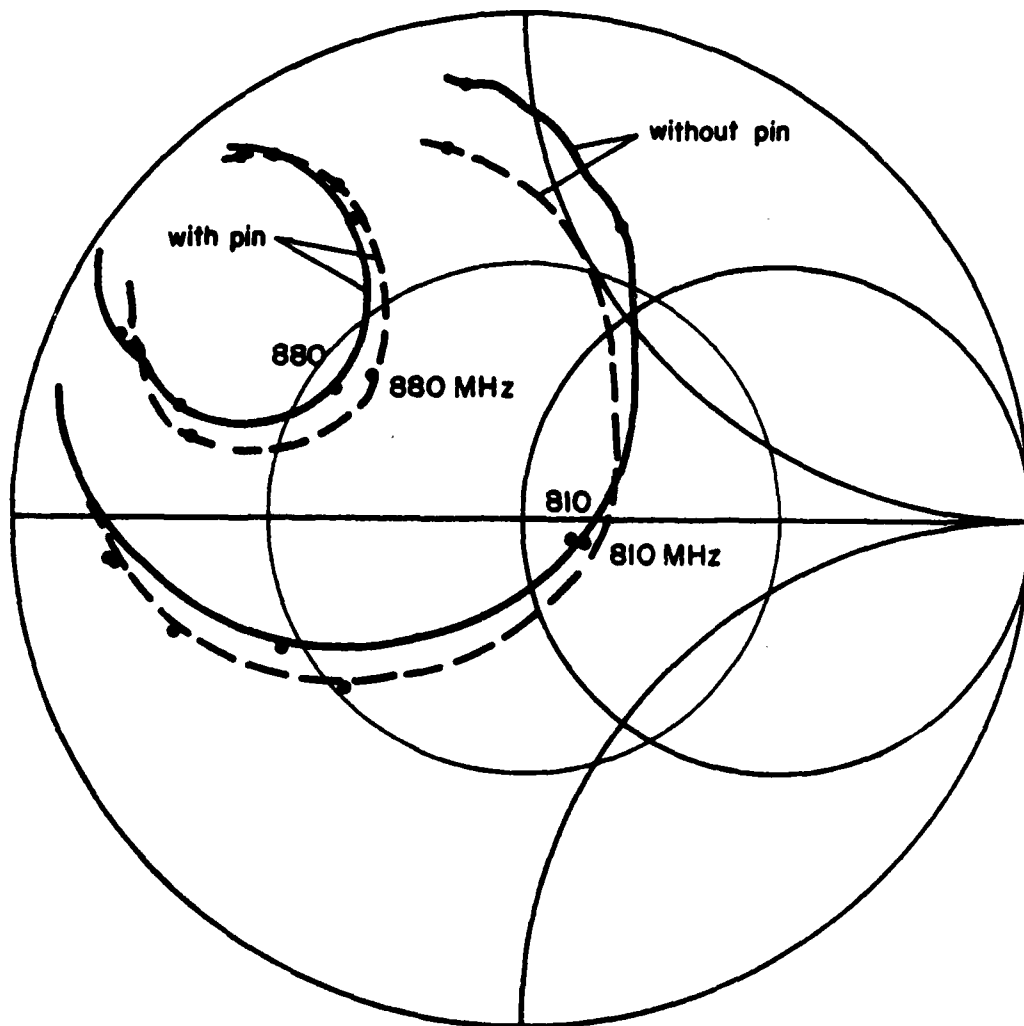
Figure 12. E- and H-plane radiation patterns at  $f = 2348$  MHz for the antenna shown in Figure 8 with four pins at positions (1) to (4).

are practically the same as before, whereas the low band patterns have a narrower beam in the E-plane as noted previously.

So far we considered the modified rectangular microstrip antennas with either a shorting copper tape inserted in the slot at the edge  $y = b$ , or a series of shorting posts at that edge. From fabrication point of view, both of these methods are awkward. To alleviate this difficulty, we investigated the possibility of cutting off the portion II, defined by  $y > b$ , of the entire antenna. Figure 13 shows the change in low band impedance loci before and after the portion II was cut off for the two cases when no pin or one pin was inserted. It is seen that there is no deleterious effect. Thus, in doing so not only there is no need to cut the slot but also the antenna can be made smaller in size.

#### 3-4 REGULAR RECTANGULAR MICROSTRIP ANTENNA FOR DUAL-FREQUENCY OPERATION

One of several microstrip antennas investigated so far is a regular rectangular patch (i.e., no electric short at  $y = b$ ) with  $a = 19.4$  cm and  $b = 14.7$  cm. It is fed with a miniature coax cable at  $x = 9.7$  cm and  $y = 0$ , as shown in Figure 14. Again, by successively adding shorting pins at the locations shown in the figure one can tune the  $(0,1)$  modal frequency  $f_{01}$  from 613 MHz to 891 MHz while maintaining the  $(0,3)$  modal frequency practically at a constant value of 1865 MHz as shown in Table 2. For those pins indicated, the ratio  $f_{03}/f_{01}$  can be varied from 3 to 2 approximately.



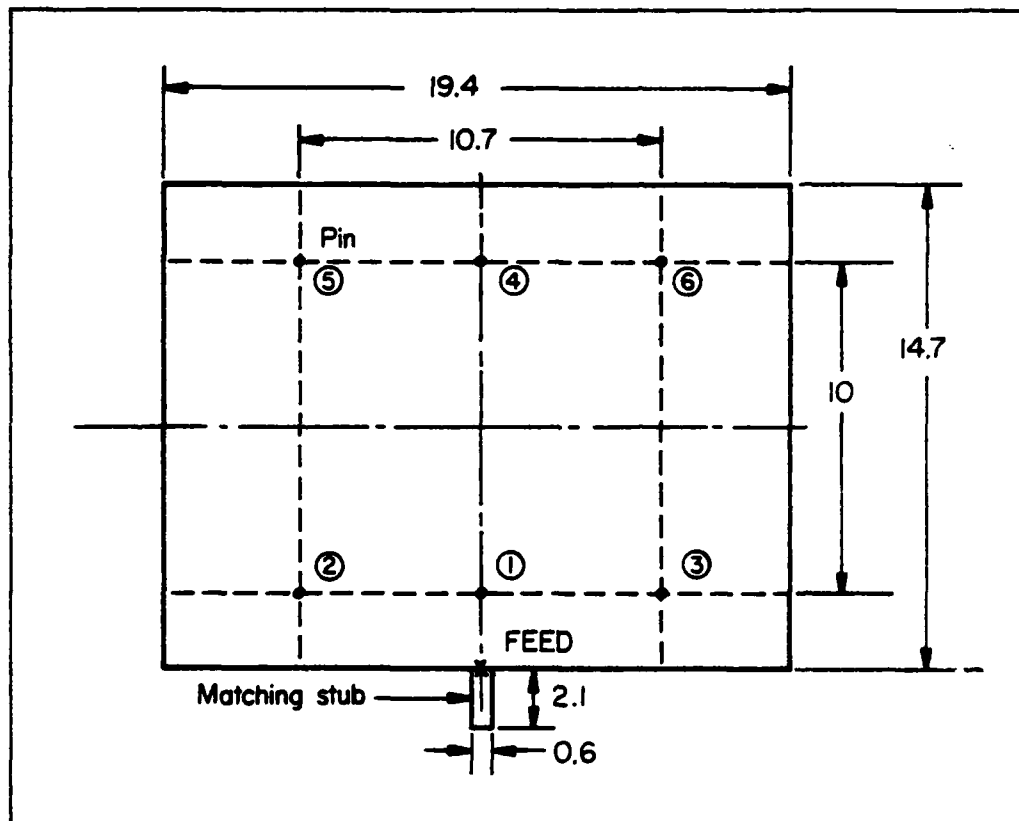
—●— Measured, Without Part II

- - ● - - Measured, With Part II

Figure 13. Truncation effect of part II of the antenna shown on the impedance loci with and without the pin.

**TABLE 2.** Resonant frequencies for (0,1) and (0,3) modes vs. shorting pins used

Number of Pins	Pin Positions	$f_{01}$	$f_{03}$	$f_{03}/f_{01}$
0	---	613	1861	3.04
1	(1)	664	1874	2.82
2	(1)(2)	706	1865	2.64
3	(1)(2)(3)	792	1865	2.36
4	(1)(2)(3)(6)	813	1865	2.29
5	(1)(2)(3)(5)(6)	846	1865	2.20
6	(1) to (6)	891	1865	2.09



All dimensions in cm

Figure 14. A regular rectangular microstrip antenna with six pins and a short matching stub.

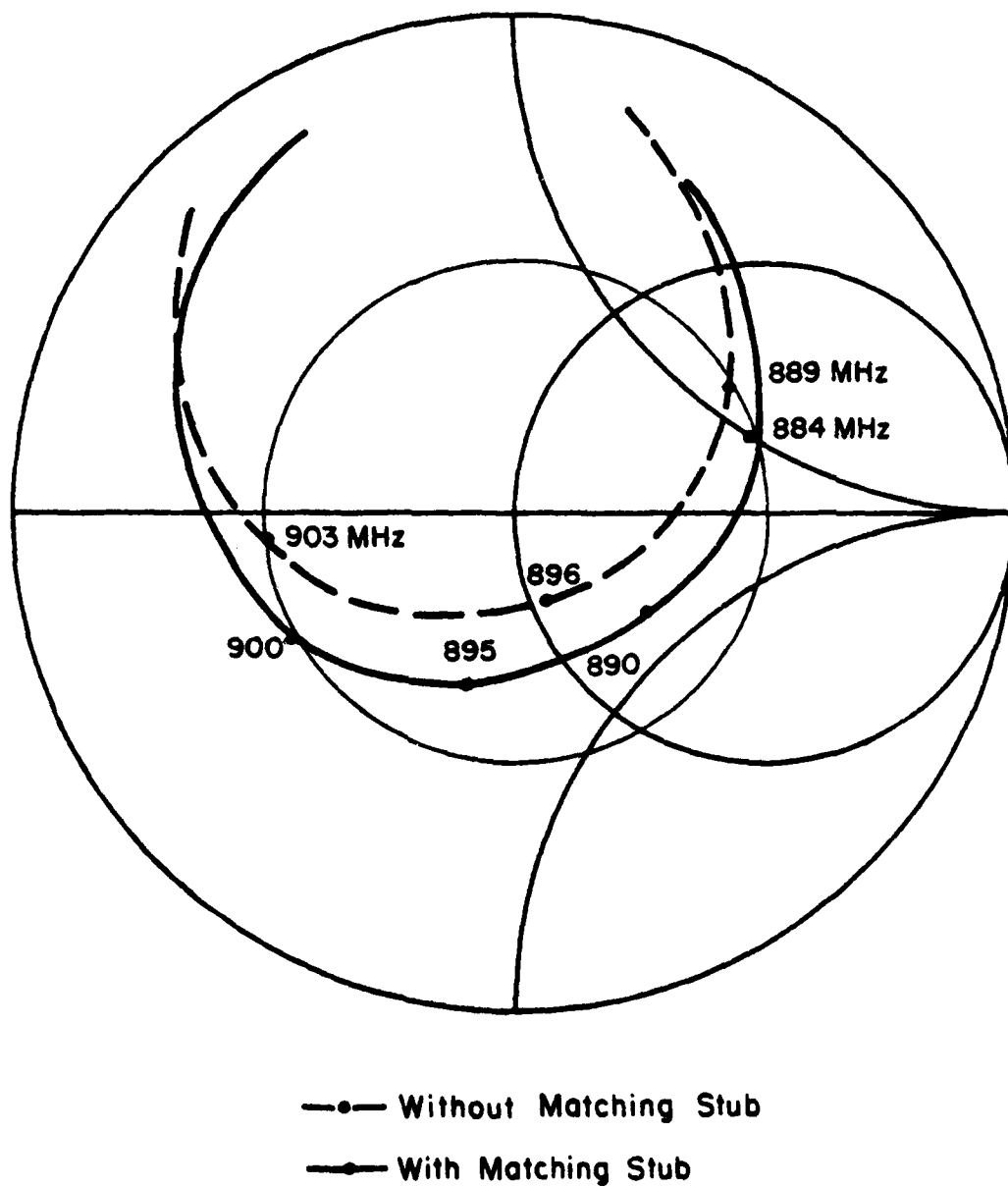


Figure 15. Low band impedance loci of the antenna shown in Figure 14 with and without matching stub at the feed.



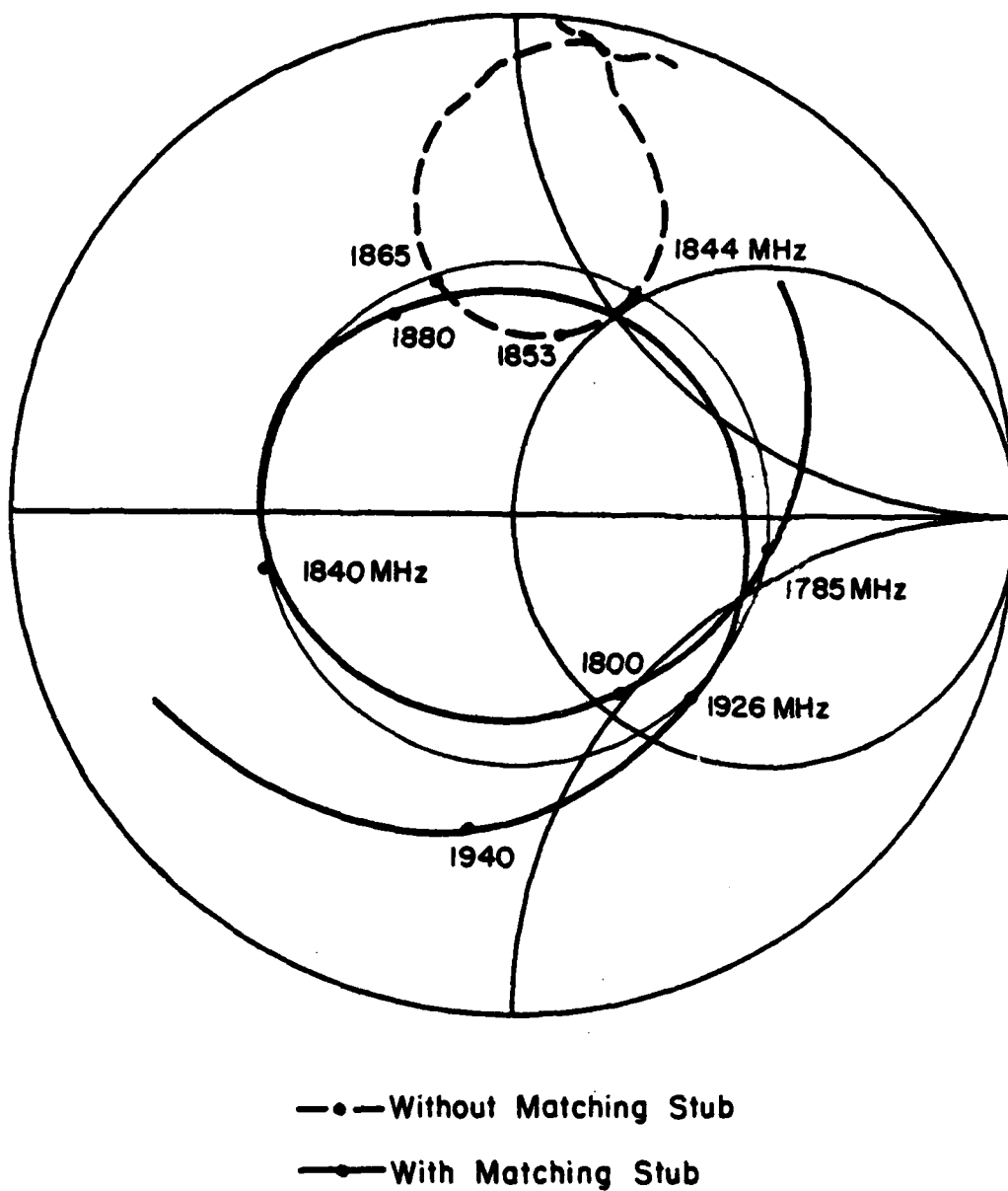


Figure 16. High band impedance loci of the antenna shown in Figure 14 with and without the matching stub at the feed.

The impedance loci for both the low and high band when all six pins were used are shown as dashed curves in Figures 15 and 16. In this case, the feed point was chosen for yielding a good impedance for the low band but not at all for the high band. But taking advantage of the large difference in their frequencies, one can very easily improve the high band impedance by adding a short capacitive microstrip line stub, about 2.1 cm x 0.6 cm in this example, at the feed as shown in Figure 14. With this shunting stub, almost the entire high band impedance locus, shown in solid curve in Figure 16, is moved into the 3:1 SWR circle, resulting in a bandwidth of almost 8%. But this stub is too short to have any harmful effect on the low band as can be seen in Figure 15.

Alternatively, one may choose the feed location for the high band impedance and position the shorting pins on the nodal lines of the high mode field for adjusting both the low band frequency and impedance.

Typical radiation patterns for the low band frequency  $f_{01} = 610$  MHz with no pins and  $f_{01} = 883$  MHz with all six pins are shown in Figures 17 and 18. The patterns for the high band frequency  $f_{03} = 1848$  MHz when all six pins are used are shown in Figure 19. Because of the wide spacing at this frequency between the two magnetic current line sources at  $y = 0$  and  $y = b$ , the E-plane pattern exhibits large grating lobes. As explained before, they can be eliminated by using materials with high dielectric constants.

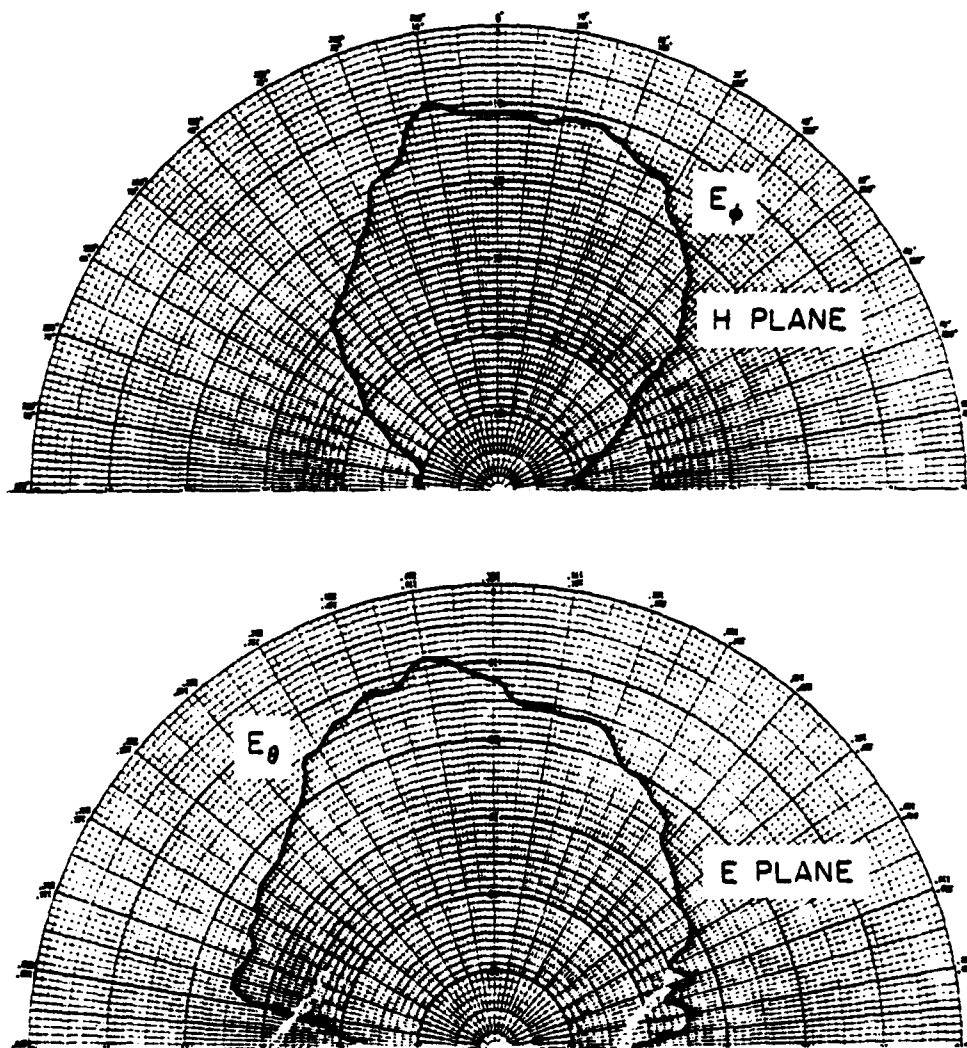


Figure 17. Typical low band radiation patterns of the antenna shown in Figure 14 without pins at  $f = 610$  MHz.

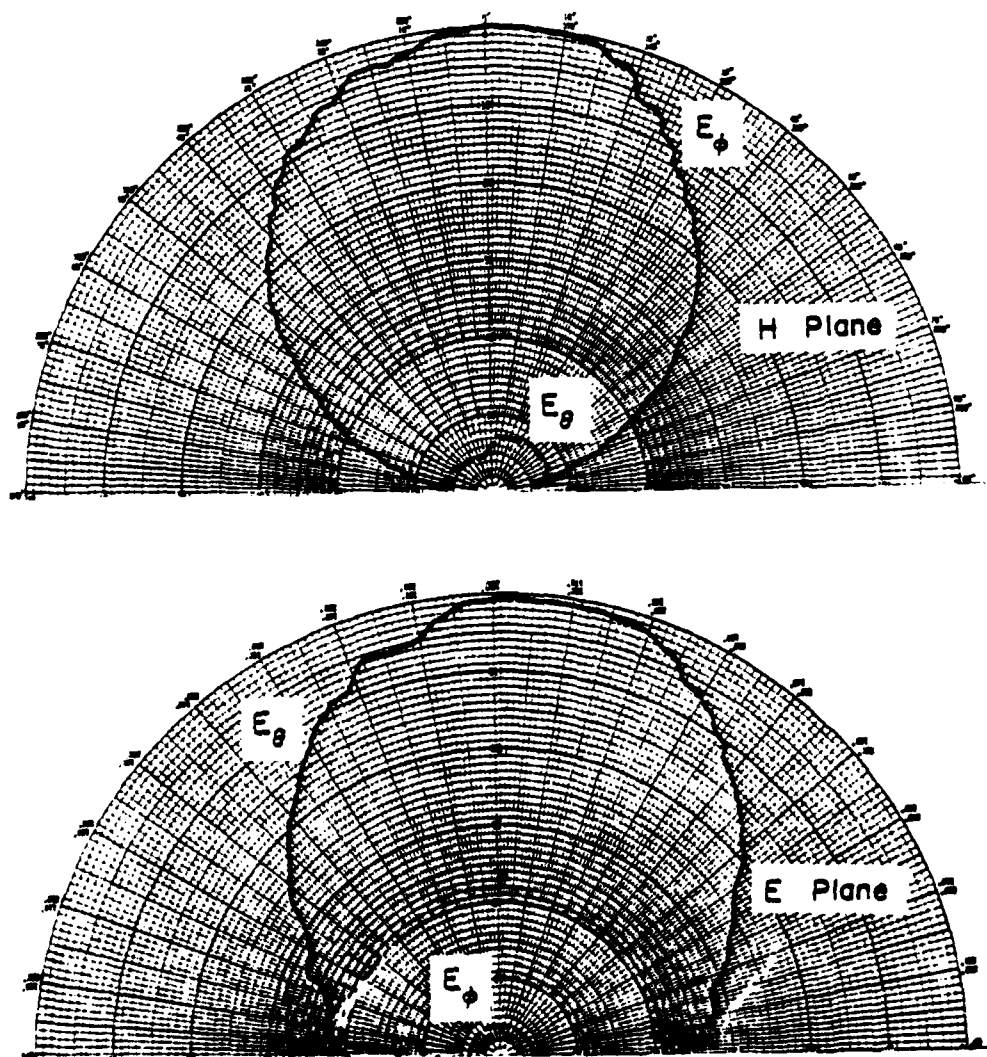


Figure 18. Typical low band radiation patterns of the antenna shown in Figure 14 with all six pins at  $f = 883$  MHz.

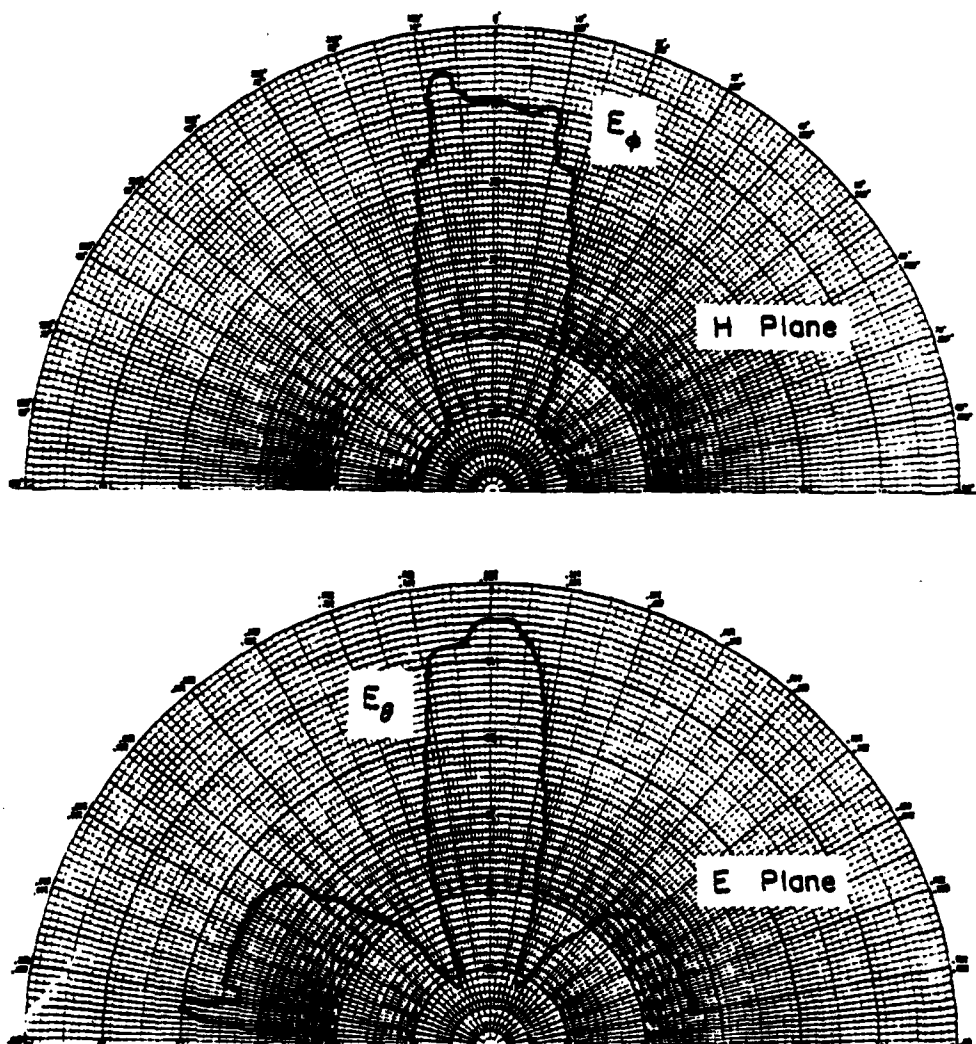


Figure 19. Typical high band radiation pattern of the antenna shown in Figure 14 with all six pins at  $f = 1848$  MHz.

## CHAPTER 4

## CONCLUSION

This investigation shows that a rectangular microstrip antenna can be designed to perform for dual bands, corresponding to the (0,1) and (0,3) modes. Some highlights and design guidelines are listed below:

- (1) The radiation patterns for both bands are predominantly broadside and have the same polarizations;
- (2) The input impedances at the feed for both bands can be designed to match the characteristic impedances of commonly used transmission lines;
- (3) The operating frequencies for the two bands can be tuned over a wide range, with a ratio from less than 1.8 to greater than 3;
- (4) The independent frequency-tuning for the low band is achieved by inserting shorting pins on the nodal lines of the (0,3) modal field on the patch, while the operating frequency of the high band is determined by the patch dimensions;
- (5) In general, the low band frequency increases with the number of pins used and the rate of increment is greater for pins in the high electric field area, except near the edges where the fringing effect becomes significant;
- (6) Taking advantage of the differences in high and low band frequencies, (a) simple matching stubs may be designed to

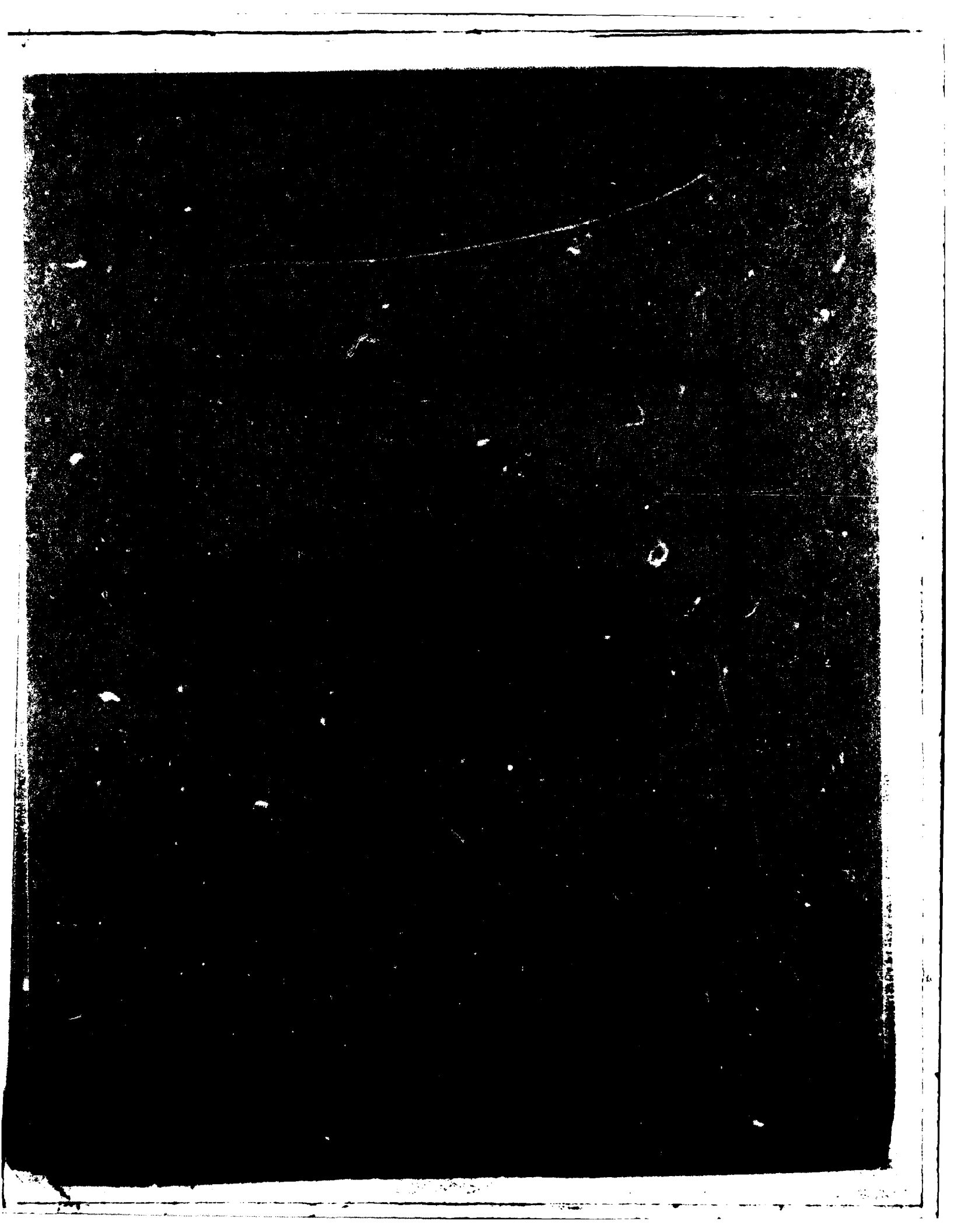
improve the high band impedance, while the feed location is selected for proper low band impedance, or (b) the feed location is selected for proper high band impedance while the low band impedance is tuned with shorting pins;

- (7) To avoid the grating lobes in the high band patterns, either materials with high dielectric constants should be used, or the rectangular patch should be modified with one edge electrically shorted to ground;
- (8) The multi-port theory can predict the performances of antennas with shorting pins very well;
- (9) This approach to dual-frequency microstrip antennas has the advantage that it consists of a single element and a single feed; therefore, it can result in great savings in weight, space, and materials in large array applications.

LIST OF REFERENCES

- [1] Sanford, G.G., and R.E. Munson, "Conformal VHF Antennas for the Apollo-Soyuz Project," IEEE AP-S International Symposium Digest, Oct. 1976, pp. 113-116.
- [2] Richards, W.F., Y.T. Lo, and D.D. Harrison, "An Improved Theory for Microstrip Antennas and Applications," IEEE Transactions on Antennas and Propagation, vol. AP-29, no. 1, pp. 38-46, Jan. 1981.
- [3] Lo, Y.T., W.F. Richards, and J.E. Brewer, "Evaluation of Losses in Microstrip Antenna Materials." Report No. RADC-TR-80-85, April 1980, AD# A087 476.
- [4] Lo, Y.T., W.F. Richards, P.S. Simon, J.E. Brewer, and C.P. Yuan, "Study of Microstrip Antenna Elements, Arrays, Feeds, Losses and Applications." Report RADC-TR-81-98, June, 1981. D# A104 493.





DATE  
FILMED  
8